WAVE DRAG OPTIMIZATION OF HIGH SPEED AIRCRAFT

A THESIS SUBMITTED TO
THE GRADUATE SCHOOL OF NATURAL AND APPLIED SCIENCES
OF
MIDDLE EAST TECHNICAL UNIVERSITY

BY

CAN ÇITAK

IN PARTIAL FULFILLMENT OF THE REQUIREMENTS
FOR
THE DEGREE OF MASTER OF SCIENCE
IN
AEROSPACE ENGINEERING

JANUARY 2015

Approval of the thesis:

WAVE DRAG OPTIMIZATION OF HIGH SPEED AIRCRAFT

submitted by **CAN ÇITAK** in partial fulfillment of the requirements for the degree of **Master of Science in Aerospace Engineering Department, Middle East Technical University** by,

Prof. Dr. Gülbin Dural Ünver
Dean, Graduate School of **Natural and Applied Sciences** _____

Prof. Dr. Ozan Tekinalp
Head of Department, **Aerospace Engineering** _____

Prof. Dr. Serkan Özgen
Supervisor, **Aerospace Engineering Dept., METU** _____

Examining Committee Members:

Prof. Dr. Hüseyin Nafiz Alemdaroğlu
Aerospace Engineering Dept., METU _____

Prof. Dr. Serkan Özgen
Aerospace Engineering Dept., METU _____

Prof. Dr. Gerhard Wilhelm Weber
Institute of Applied Mathematics, METU _____

Assoc.Prof. Dr. Metin Yavuz
Mechanical Engineering Dept., METU _____

Dr. Erhan Tarhan
Department of Flight Sciences, TAI _____

Date: 27.01.2015

I hereby declare that all information in this document has been obtained and presented in accordance with academic rules and ethical conduct. I also declare that, as required by these rules and conduct, I have fully cited and referenced all material and results that are not original to this work.

Name, Last name: Can ÇITAK

Signature:

ABSTRACT

WAVE DRAG OPTIMIZATION OF HIGH SPEED AIRCRAFT

Çıtak, Can

M.S.,Department of Aerospace Engineering

Supervisor: Prof. Dr. Serkan Özgen

January 2015, 97 pages

Supersonic flight has been the subject of the last half century. Both military and civil projects have been running on to design aircraft that will fly faster than the speed of sound. Developing technology and increasing experience leads to faster, more fuel – efficient, longer ranged aircraft designs. These vehicles have the advantage of shortening travelling times in the civilian role and performing missions with greater success in the military role. Aerodynamic design is the main argument of high speed aircraft improvement. Having less supersonic drag force, which is greater than double of the subsonic case for conventional aircraft, is the ultimate goal of the aircraft designers for supersonic design. Optimizing aerodynamic characteristics of supersonic air vehicles by reducing wave drag is the main purpose of this thesis. A computational tool using computational fluid dynamics, analytical and numerical methods is developed in order to meet this goal. Firstly, wave drag coefficient solver algorithm is generated on a MATLAB interface. Then, the solver is validated with different geometries by using computational fluid dynamics simulations at various speeds. ANSYS Fluent is used for flow simulations. Next, gradient-based constrained optimization algorithm is employed to minimize the wave drag coefficient of a supersonic aircraft design. In addition, test cases are selected to observe the success of the wave drag coefficient optimization program for different situations. Finally, fighter aircraft geometry is optimized with respect to engine size constraints.

Keywords: wave drag coefficient, optimization, aerodynamics, supersonic flight, compressible flow, supersonic area rule.

ÖZ

YÜKSEK HIZDA UÇAN HAVA ARACININ DALGA SÜRÜKLEME KUVVETİNİN ENİYİLEŞTİRİLMESİ

Çıtak, Can
Yüksek Lisans, Havacılık ve Uzay Mühendisliği Bölümü
Tez Yöneticisi : Prof. Dr. Serkan Özgen
Ocak 2015, 97 sayfa

Sesüstü hızlarda uçuş son yarım yüzyılın araştırma konularından olup, sesüstü hızlarda uçabilen uçakların tasarımı için hem askeri hem de sivil projeler yürütülmüştür. Tasarım konusunda gelişen teknoloji ve artan yetenekler sayesinde daha hızlı yakıt verimliliği yüksek ve daha uzun menzile sahip uçaklar tasarlanabilir duruma gelmiştir. Bu araçlar sayesinde seyahat süreleri azalmakta ve askeri görevler daha güçlü hava araçları ile daha yüksek başarımla yerine getirilmektedir. Şüphesiz ki aerodinamik tasarım bu gelişmeleri sağlayan en önemli faktörlerden biridir. Daha düşük sesüstü sürükleme kuvveti katsayısına sahip (standart bir hava aracının sesüstü sürükleme kuvveti katsayısı, sesaltı hızdakine göre iki kat daha fazladır) uçaklar, tasarımcıların nihai hedefi olmuştur. Hava aracının aerodinamik karakteristiklerinin dalga sürüklenmesinin azaltılması ile eniyilemesi ana hedefleridir. Bu çalışmanın amacı hesaplamalı akışkanlar dinamiği, analitik yöntemler ve sayısal yöntemleri kullanarak yüksek hızlarda uçması için tasarlanan uçakların dalga sürükleme katsayısının eniyileştirilmesini yapabilen bir hesaplama aracı geliştirmektir. İlk olarak, dalga sürükleme katsayısı çözücüsü MATLAB arayüzü kullanılarak oluşturulmuştur. Daha sonra, kullanılan akış çözücüsünün farklı geometriler ve hızlar için hesaplamalı akışkanlar dinamiği (HAD) yöntemi kullanılarak doğrulama yapılmıştır. Burada akış çözücüsü olarak ANSYS Fluent kullanılmıştır. Ardından, düğüm tabanlı kısıtlı eniyileme yöntemi kullanılarak ses üstü hızda uçabilen hava aracının dalga sürükleme kuvveti en aza indirilmeye çalışılmıştır. Buna ek olarak,

farklı durumlar için dalga sürükleme katsayısı optimizasyon programının başarımı gözlemlenmiştir. Son olarak, bir savaş uçağı geometrisi, motor boyutlandırma kısıtlamalarına göre eniyileştirilmiştir.

Anahtar Kelimeler: Dalga sürükleme kuvveti katsayısı, eniyileme, aerodinamik, sesüstü uçuş, sıkıştırılabilir akış, sesüstü alan kuralı.

To Hatice İnci

ACKNOWLEDGEMENTS

I would like to express my deepest appreciation to my advisor Prof. Dr. Serkan Özgen for his guidance, encouragement, and support. Moreover, his contribution to push abilities and widening my scientific perspective were the wings flying to perfection. I must also thank to Prof. Gerhard Wilhelm Weber for his effort to provide precious information.

I would like to thank Meral Ceren Bilgen for supporting me throughout this study. I would like to thank my friends Emre, Hakan, Özgür, Mustafa, and Onur for their help and encouragement.

Finally, I would like to express my gratitude to my family for their support and encouragement throughout my life.

TABLE OF CONTENTS

LIST OF TABLES

TABLES

LIST OF FIGURES

FIGURES

LIST OF ABBREVIATIONS

HSRP: High Speed Research Program

SBJ: Supersonic Business Jet

EFD: Experimental Fluid Dynamics

CPU: Central Processing Unit

GUI: Graphical User Interface

VSP: Vehicle Sketch Program

BFGS: Broyden–Fletcher–Goldfarb–Shanno

S-H: Sears–Haack

ICAS: International Council of Air Shows

CHAPTER 1

INTRODUCTION

1.1 Supersonic Flight

Designing an aircraft with the ability of flying faster than the speed of sound was the purpose of most aircraft designers in the past decades. Unlike the subsonic design, the supersonic design has obstacles to deal with in order to reach this aim. The major part of this problem is about the huge drag force occurring when compared to subsonic speed. Thus, aircraft designers aware of these drawbacks were in the need of making modifications and improvements to their designs.

Many aircraft, both military and commercial have been designed after the first supersonic flight of "*Bell X-1*". Most of the supersonic aircraft are military aircraft except for two which were able to go beyond the drawing board; *Concorde* and *Tupolev Tu-144*. The reasons behind the design and utilization of these aircraft were commercial benefits, which mainly included the attainability of lower fuel consumption as the first issue. Thus, aircraft mentioned above are no longer in service due to the fact that they have high fuel consumption because of the supersonic drag requiring more engine power to overcome. Although only two of such airplanes flew, important projects were pursued in the recent years. High – Speed Research (HSR) Program undertaken by NASA was the most important of these. The aim of the program was to design a supersonic aircraft with the capacity of 300 passengers, which could fly twice the speed of sound for the high cruise range mission. The program was cancelled due to funding reasons. Despite the fact that the aircraft would fly across the Pacific Ocean in half the time the aircraft of equivalent eligibility could achieve, the ticket price was predicted to be comparable to other airliners [1]. Moreover, supersonic

civil aircraft projects still proceed. *Aerion SBJ, Tupolev Tu–444, Spike S-512* are some of the supersonic business jet projects which offer long flights in shorter time.

Unlike commercial aviation, the main object of military aviation is performance. In other words, the aircraft has to complete the mission in the shortest time possible, which brings out the aerodynamic design trade-off challenge. In order to increase aircraft speed, more power is needed from the engine, which means more amount of fuel. However, any additional fuel weight increases the total weight of the aircraft which also reduces the maximum speed and acceleration of the aircraft. Thus, supersonic aircraft design is a challenge, which involves many difficulties and necessitates trade-off studies for designers.

Aerodynamic design principles of these aircraft are different from the subsonic aircraft due to the fact that the drag of an aircraft at supersonic speeds increases sharply. For example, two aircraft can be compared in order to observe the differences between supersonic and the subsonic aircraft design; namely, *Concorde* and *Boeing 747-400. Boeing 747-400* has a moderately swept wing and a thick airfoil; while *Concorde* has a high swept wings and a thin airfoil. In addition, *Concorde* has a sharp nose and a slender fuselage; on the other hand, *Boeing 747-400* has a blunt nose and a wide blunt body. Figure 1 and Figure 2 shows 3 views of *Concorde* and *Boeing 747*.

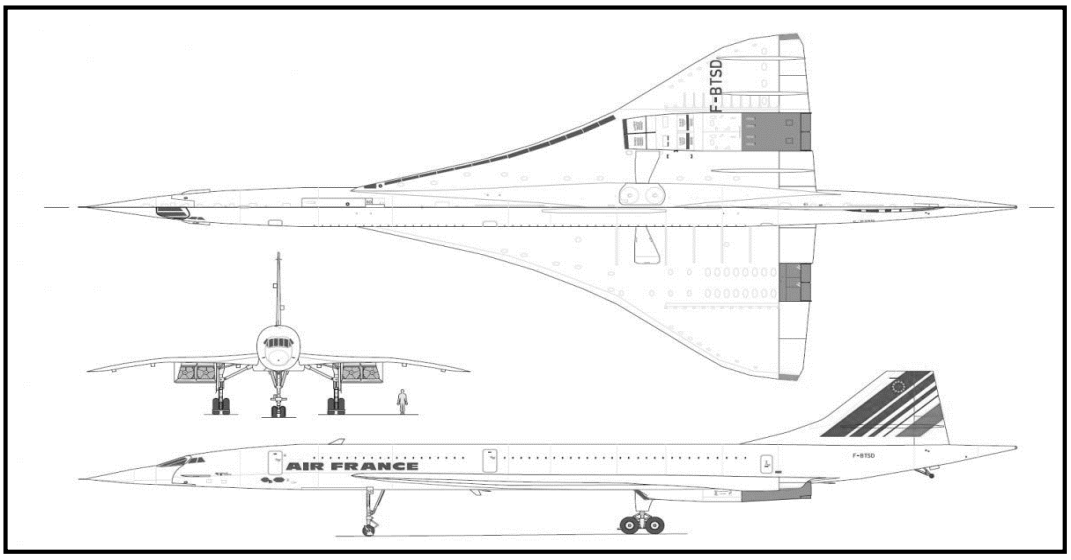

Figure 1–Concorde 3 view (Top, front, and side views) [2]

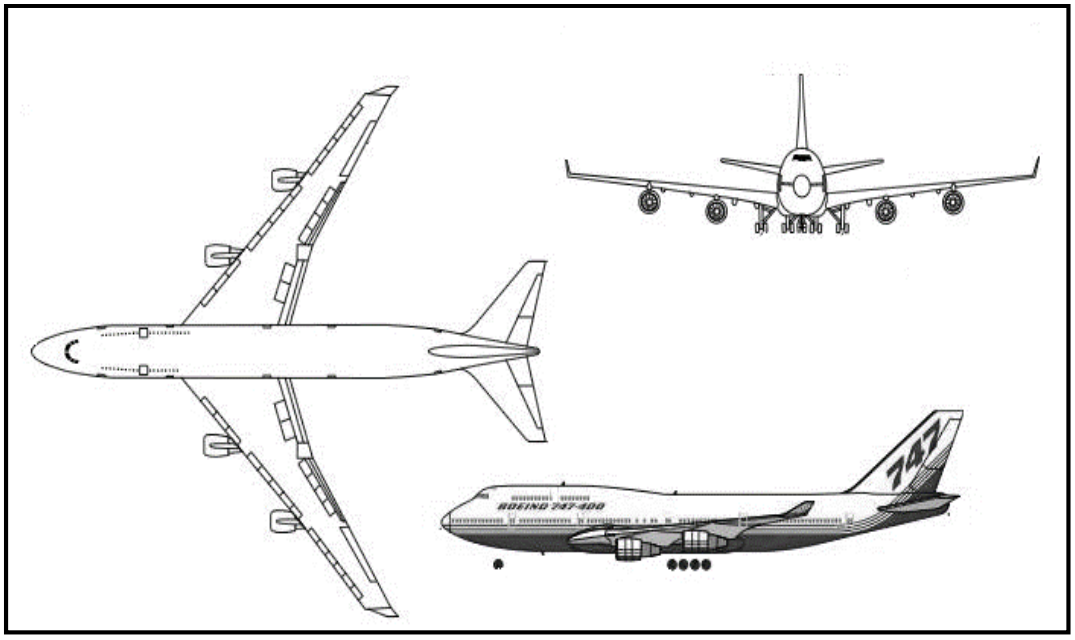

Figure 2–Boeing 747-400 3 view [3]

The reason why the shapes of these aircraft presented above are different is the minimization of total drag force and optimization of other aerodynamic parameters. Since flow behavior at supersonic and subsonic flight are different, shapes having minimum drag force in different flow regimes are not the same.

1.2 Wave Drag Force

Drag can be described as the force resisting aircraft motion. It depends on the velocity of the aircraft, wing area, air density and drag coefficient which are related to the complete aircraft configuration. The main purpose in an aircraft design is generally to reduce drag to a minimum. On the other hand, drag force is beneficial for some cases; such as the utilization of complex flap mechanisms or drag parachutes to shorten landing distances.

Drag is mainly classified as drag due to lift and zero–lift drag. Figure 3 presents the types of drag. The work presented in this thesis mainly concentrates on the wave drag,

which is a zero-lift drag constituent. Induced wave drag is outside the scope of this thesis.

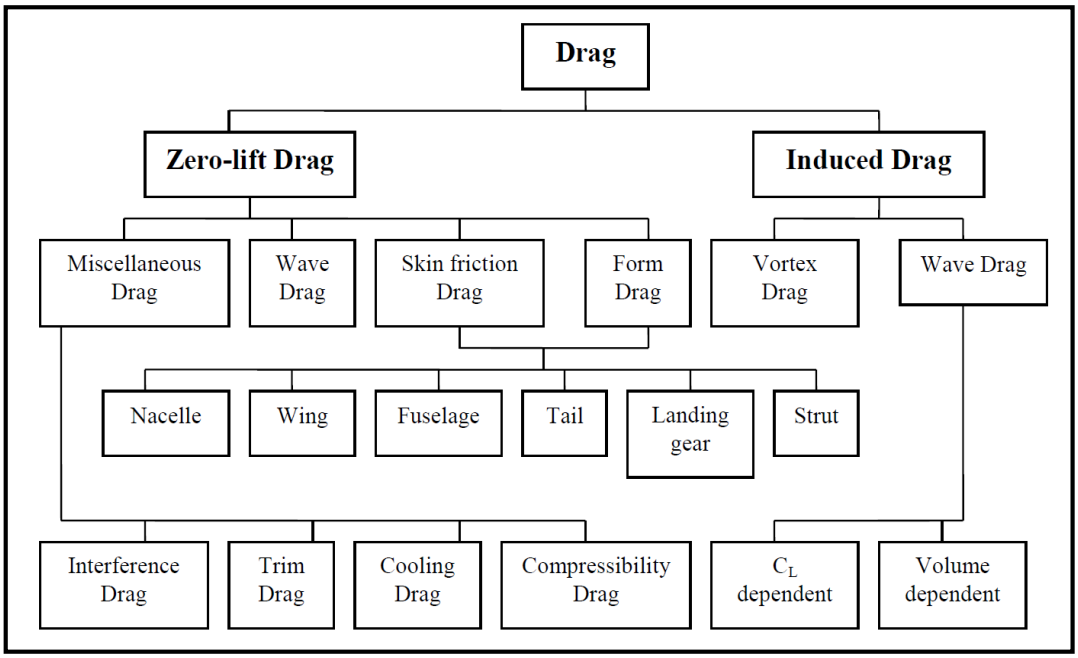

Figure 3–Drag classification [4]

Temperature, pressure, aircraft velocity and the geometry of the configuration affects the magnitude of the wave drag. When supersonic freestream flow reaches an obstacle, shock waves occur, which increase the density and pressure of the flow. In other words, the freestream Mach number, which must be greater than one for shock wave to occur, decreases below Mach 1 downstream of the normal shock formation. The shock wave results in increase in entropy and reduction in total pressure. If the shock wave is inevitable, the efficiency of the shock formation can be increased in order to reduce the increase in entropy. A swept wing and/or fuselage shaping can be used for this purpose. This study aims at minimizing the wave drag coefficient without changing the aerodynamic characteristics of the lifting surfaces, hence without altering the total lift. The tail surfaces are also not altered in any way. Thus, the area distribution and the volume of the fuselage are modified to reach the minimum value of the objective function.

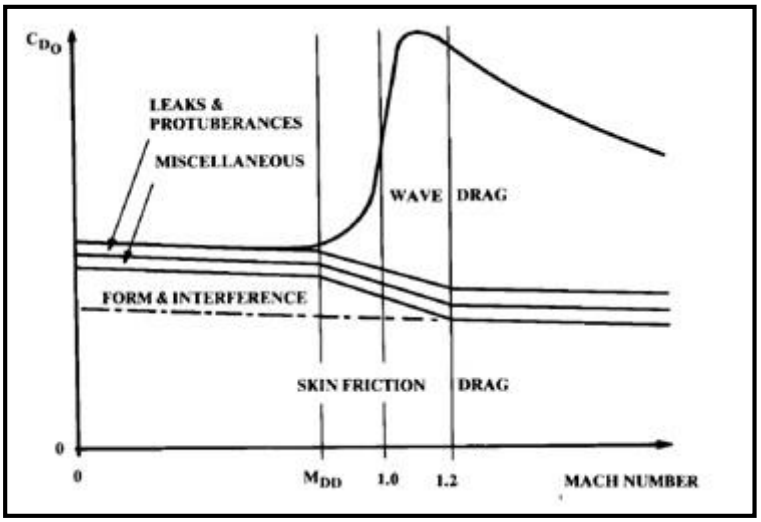

Figure 4–Drag variation with Mach number [5]

As seen in Figure 4, the supersonic drag of an aircraft increases 3 - 4 times compared to the subsonic value in a poorly designed aircraft, so the drag optimization of supersonic aircraft is the main criterion of the aerodynamic design process. Nevertheless, the theoretical optimal shape of aircraft are not being implemented to the base design due to manufacturing and sub-component constraints which give rise to additional drag. Small changes in supersonic drag could be critical. To illustrate this, on the *Concorde*, it can be stated that one count drag increase ($\Delta C_D = 0.0001$) requires two passengers, out of the 90-100 passenger capacity, be taken off the North Atlantic run [6]. Additional drag components at supersonic speed are wave drag due to lift and wave drag due to volume. Wave drag due to lift vanishes as Mach number approaches one or aspect ratio approaches zero and will not be elaborated in this study [32]. On the other hand, wave drag due to volume is investigated in the current study. The behavior of the volume wave drag at various Mach numbers and different geometries are observed.

Kulfan et al. [7] investigated different methods for the calculation of the supersonic drag on a variety of aircraft design. Kulfan separated high speed civil transport aircraft design into sub–topics according to the optimal design considerations. Firstly, the fuselage must be optimized with respect to the area rule. As the area magnitudes and the locations of control and lifting surfaces are kept constant, the fuselage area

distribution must be reshaped to obtain the optimum wave drag coefficient. Then, the optimal geometry of the leading edge emerges as blunt at inboard, sharp at outboard. Nacelles are also shaped to have efficient shock formation. According to wave drag theory, the cross sectional area of the engine must be subtracted from the area distribution while calculating the wave drag coefficient. Furthermore, wing planform is shaped to satisfy high lift requirements, and supersonic cruise specifications. Moreover, flow separation over the aircraft at high speed could be huge complexity to aircraft stability. Thus, the transition of aircraft geometry components must be smooth.

The importance of the wave drag is observed drastically on the Convair F-102. First prototype, YF-102A was lost due to the fact that wave drag force was higher than expected. (Thus, requirements related to overcome drag force is below limits [35]. Area distribution of the aircraft, thereby, shape of the geometry was later modified with respect to the area rule [36]). Figure 5 illustrates the re-design of the F-102. With this modification the F102-A was able to exceed the speed of sound comfortably.

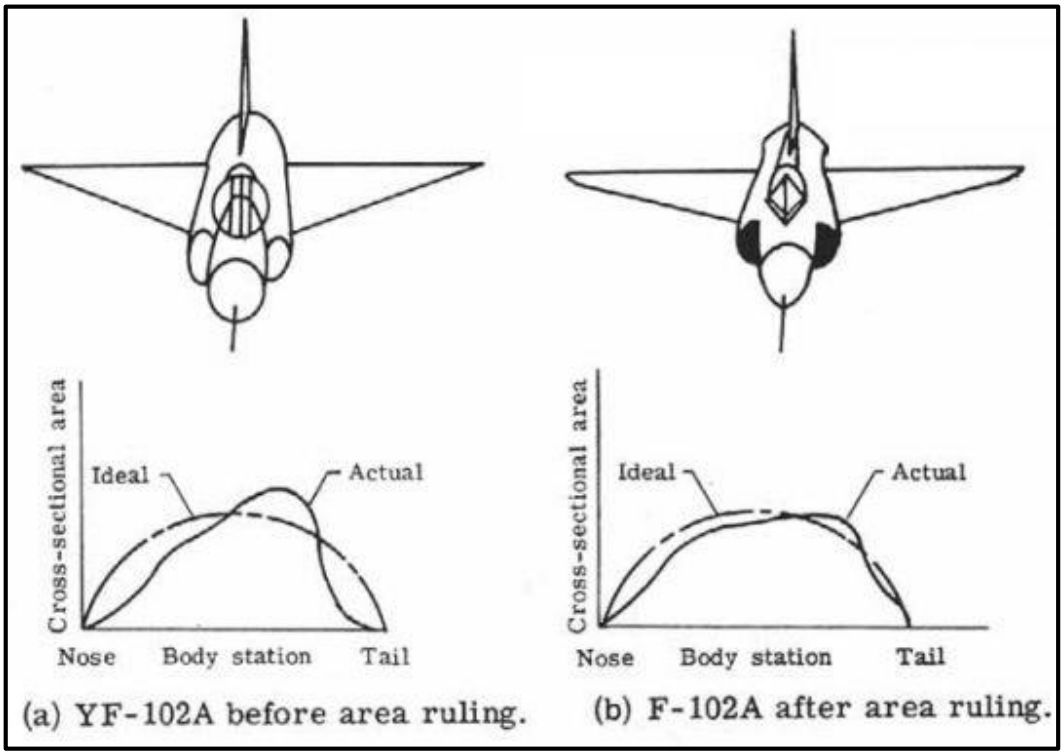

Figure 5-Re-design of F-102 [35]

1.3 The Review of Methods for Wave Drag Calculation

There are three methods to calculate the supersonic drag in the literature. Namely; experimental fluid dynamics (EFD), computational fluid dynamics (CFD) and linearized fluid dynamics. EFD is the most accurate method for analyzing the behavior of the flow over the aircraft. However, there are several disadvantages when comparing with other methods written above. First of all, EFD is not preferable during the conceptual design process due to the cost of a supersonic experimental setup. Massive workload is required since more than one experiments ought to be conducted for various speeds and different geometries. CFD is another successful method to investigate the flow behavior numerically, which takes far more time than the linearized method. The motivation of this work is to develop an accurate, but yet simple, user-friendly wave drag coefficient optimization tool for the conceptual aircraft design process. The tool also has to be comprehensive enough not to observe the physical basis.

Although aircraft design is more and more dominated by CFD, linearized methods are still in use for fast predictions. Some advantages and disadvantages of linearized methods can be mentioned. Main reason behind the advantages of linearized theory is the speed of operation. Linearized theory can be easily used for optimization process due to its direct formulation. Linearized theory is also used for trade-off studies since it is fast when compared to other methods. On the other hand, it cannot estimate the viscous effects on drag. In cases, such as incompressible subsonic flow, where the majority of the drag contribution is coming from viscous drag, linearized theory could be inappropriate. For the same reason, without considering the surface roughness, it under-estimates the pressure distribution over the aircraft.

CFD has superiority over linearized methods when analyzing the flow fields of complex geometries. Firstly, linearized theory is limited to a certain Mach number interval. However, CFD is used for any Mach number by choosing the appropriate solution method and the numerical scheme. Effect of the aircraft geometry details, such as wing body intersection, surface roughness, and shock formation over the body

on flow dynamics could be observed by using CFD. Nevertheless, although the accuracy in this case is higher than in linearized theory, computational time and effort are greater. If CFD was used for optimization, computational time because of CPU usage therefore would become larger. However, the accuracy of linearized theory proves satisfactory for conceptual aircraft design. Furthermore, when speed of CFD and linearized theory are compared, linearized theory is much faster than CFD. Since the shape of the aircraft changes many times during the design process, using fast methods like linearized theory is beneficial for designers instead of using CFD.

The most well-known linearized theory code in literature is Harris Wave Drag Program which has been used for more than 50 years in High Speed Civil Transport program and various academic researches. Rallabhandi et al. [8] investigated wave drag calculation with their own program and compared their results with those obtained from the Harris wave drag code. The program in the study was more complex and therefore slower than Harris wave drag program written in FORTRAN [24]. In addition, Delaunay triangulation program was created as well to analyze the aircraft geometry with different methods [9].

Near–field and far–field wave drag theories can be used for the calculation of supersonic wave drag force for conceptual design of high speed aircraft. The far–field wave drag theory computes the zero lift wave drag of an aircraft by means of the supersonic area rule, assuming the lift generated by the aircraft is zero. The method states that the wave drag of an aircraft is the same as the wave drag of an equivalent body of revolution having the same cross–sectional area distribution. In other words, the contribution of the cross –section shape is zero. Flow separation over the aircraft geometry is not taken into account for the wave drag calculation due to cross–section shape. Second, the near–field wave drag theory computes zero–lift thickness pressure distributions for the entire aircraft configuration of aircraft. Then, the pressure distribution is integrated over the cross–sectional area of the aircraft in order to calculate the wave drag coefficient. Accurate presentation of an aircraft depends on the cross–sectional area distribution in both approaches. Two difficulties that must be avoided during the computation; round-off error and missing the geometry changes of

aircraft. First and second derivatives of cross–sectional area distribution of an aircraft are used for both theories to obtain the wave drag coefficient. Thus, using a high number of cross-sections yields the round–off error, which gives inaccurate results. On the other hand, using less number of cross–sections causes deficient representation of the aircraft geometry [25]. Small changes in cross–sectional area magnitude might result in massive increase in drag. Being aware of these difficulties, sensitivity analysis must be done to obtain the accurate aircraft representation. In other words, the derivatives must be continuous in order to calculate the drag force correctly. Thus, transforming cross-sectional area distribution to higher order polynomial functions is beneficial to obtain wave drag coefficient accurately.

1.4 Optimization Methods Review

The optimization of the aircraft geometry is one of the main parts of aircraft design. While optimizing one design goal, another one could be worsened. For example; in order to minimize wave drag coefficient, the area distribution of the aircraft could be changed unrealistically. However, the effect of the change in area distribution must be considered for other design goals, such as the center of gravity location which is important for the stability of the aircraft [30, 31]. Determining constraints is also critical for the optimization process. The objective function may transform the initial aircraft geometry to a shape which is not possible to produce. To illustrate; the magnitude of the cross-sectional area at engine location must be kept above a certain magnitude due to the fact that parts used to connect between the wing and the engine need volume to be placed [27]. If engine is placed at the rear fuselage, the program gives optimal cross-sectional area magnitude at this location as zero which is infeasible considering the arrangement of the aircraft.

Two different mathematical optimization methods that can be used for minimization are, genetic algorithm and gradient based optimization methods. Evolutionary algorithms use more CPU time due to the fact that the way they optimize the objective function is by trial and error. They make a high number of function evaluations. Despite using more CPU time, mathematical formulation is simpler than the gradient

based optimization methods. On the contrary, search direction is found by calculating the gradients of the objective function in the gradient based optimization. For advanced methods, Hessian matrix needs to be calculated to obtain the gradients, which requires a large amount of CPU usage thereby take more time.

Hutchison used a gradient based algorithm for multidisciplinary design optimization [10]. He calculates the gradients by approximating the function using first order Taylor series expansion. It is a fast but accurate methodology for improvements relying on the computational power of today's world. Likewise, gradient based optimization method is used in the present work.

Convenience in use is an important parameter for aircraft design computational tools. Controlling the settings of the tool easily, visual interface for observing the geometry and simplicity for end users are the features which make the program user friendly. Graphical user interface (GUI) development satisfies the features explained above. End users could avoid the complicated input files to control program settings by using GUI. Furthermore, the interaction between input and output and the ease of the direct manipulation of the program are established so that the time spent for aircraft design decreases.

1.5 Aim of the Study

The motivation of this study is to create a computational tool for wave drag coefficient optimization of high speed aircraft. Harris wave drag code is investigated to understand the methodology behind wave drag calculations of arbitrary shapes. The developed tool uses only the cross sectional area distribution of an aircraft. Thus, the mesh of the three dimensional aircraft geometry is exported from an open source program *OpenVSP* [11] and then, the cross-sectional area distribution is calculated. This distribution is input to the program after Fourier sine transformation to smooth the distribution curve. Then, the mesh is updated at each optimization iteration by keeping the position of each cross-section on the longitudinal axis constant. Moreover, CFD analysis are completed in order to validate the wave drag coefficient results of the code. The main program interface used is created by MATLAB [12]. CFD analyse

are done by using ANSYS FLUENT [13]. Tecplot [14] is used for post–processing operations.

Brief information about wave drag calculation methods used in the designed tool and in literature, Fourier transformation, and optimization method can be found in Chapter 2. The solution procedure, numerical applications needed for initiating the tool, mathematical models created for the representation and optimization of the aircraft geometry are presented in Chapter 3. Next, validation of the wave drag coefficient solver with two different geometries, optimization test cases, and optimization of the fighter aircraft geometry results are reported in Chapter 4. Finally, conclusion, summary, and discussion of the thesis are outlined in Chapter 5.

CHAPTER 2

THEORY

Wave drag coefficient optimization can be defined under two main headings: (i) calculating the wave drag coefficient using relevant theories and (ii) the optimization methods. Wave drag of an aircraft can be obtained by using of far–field & near–field wave drag theories or computational fluid dynamics. Aim of this chapter is to give brief information about linearized theories and optimization methods; i.e., evolutionary and gradient based algorithms used in order to minimize the wave drag coefficient. The information given in this chapter is available in aerodynamics and optimization text books in greater detail [15].

2.1 Wave Drag Calculation Methods

2.1.1 Computational Fluid Dynamics (CFD)

Solution of Navier Stokes equations is a powerful method to analyze flow dynamics. However, wave drag cannot be calculated by CFD alone since the method does not separate inviscid drag into its components. However, it is assumed that 90% of the inviscid drag is the wave drag of the configuration [5]. Equations used in CFD tools are given as:

Continuity equation:

$$\frac{\partial \rho}{\partial t} + \nabla.(\rho \vec{v}) = 0. \tag{2.1}$$

x –momentum equation:

$$\frac{\partial (\rho u)}{\partial t} + \nabla.(\rho u \vec{v}) = -\frac{\partial p}{\partial x} + \frac{1}{\mathrm{Re}}\left[\frac{\partial \tau_{xx}}{\partial x} + \frac{\partial \tau_{xy}}{\partial y} + \frac{\partial \tau_{xz}}{\partial z} \right]. \tag{2.2}$$

y –momentum equation:

$$\frac{\partial(\rho v)}{\partial t}+\nabla.(\rho v\vec{v})=-\frac{\partial p}{\partial y}+\frac{1}{\mathrm{Re}}\left[\frac{\partial \tau_{xy}}{\partial x}+\frac{\partial \tau_{yy}}{\partial y}+\frac{\partial \tau_{yz}}{\partial z}\right]. \tag{2.3}$$

z –momentum equation:

$$\frac{\partial(\rho w)}{\partial t}+\nabla.(\rho w\vec{v})=-\frac{\partial p}{\partial z}+\frac{1}{\mathrm{Re}}\left[\frac{\partial \tau_{xz}}{\partial x}+\frac{\partial \tau_{xz}}{\partial y}+\frac{\partial \tau_{zz}}{\partial z}\right]. \tag{2.4}$$

Energy equation:

$$\frac{\partial(\rho \mathrm{E})}{\partial t}+\nabla\left(\left(\rho E+p\right)\vec{v}\right)=\nabla.\left[k\nabla T-\sum_{k}h_k\vec{J}_k+\left(\bar{\bar{\tau}}.\vec{v}\right)\right]+S_E. \tag{2.5}$$

2.1.2 Far–Field Theory

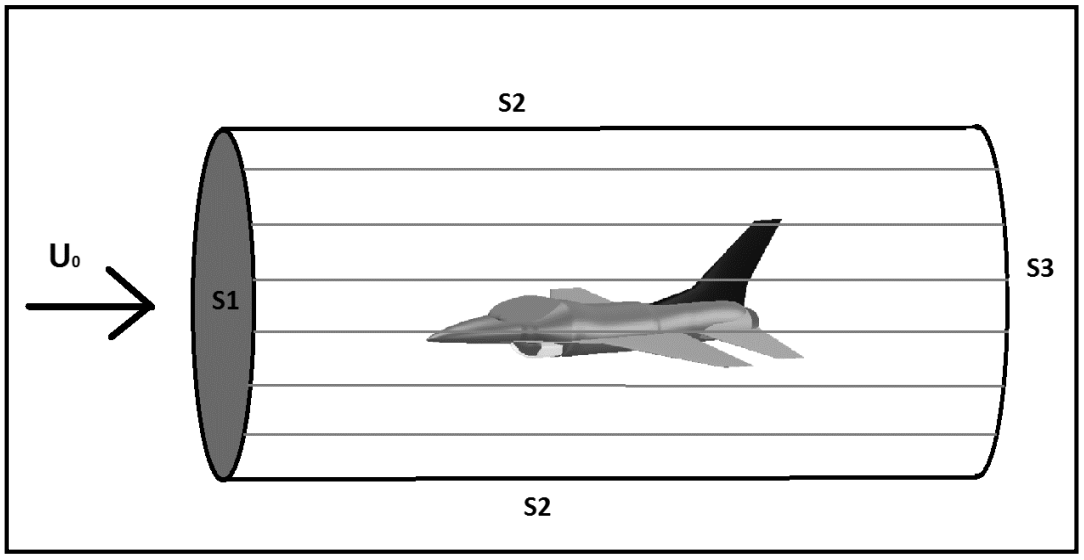

Figure 6 – Control Volume Representation

Total momentum change in streamwise direction of a control volume is equal to the drag of the aircraft. Inlet region (S1 in Figure 6) is the only undisturbed flow passing through the aircraft geometry, which becomes two dimensional because of the

pressure effects. Thus, the momentum change between the inlet and outlet regions (streamwise momentum change) is the sum of all the drag contributions. In addition, subsonic flow becomes parallel at the outlet if the control volume is large enough. On the other hand, mass flows in and out from the sides of the cylinder at supersonic speeds due to shock and expansion wave formations. Total change in momentum as a result of mass flow in and out is defined as wave drag. Moreover, since the shock formation varies with the angle of attack, wave drag can change with the angle of attack as well. Therefore, the total wave drag is the sum of wave drag due to volume and wave drag due to lift. The drag equation is given in Equation (2.6):

$$D = -\iint_{S_3=S_1} (p - p_\infty)\, dS_3 - \rho_\infty U_\infty^2 \iint_{S_3=S_1} \phi_x (1+\phi_x)\, dS_3 - \rho_\infty U_\infty^2 \iint_{S_2} \phi_x \phi_r\, dS_2 + \sum D_{Misc}. \quad (2.6)$$

If the control volume boundaries are located far enough, flow becomes two dimensional, the streamwise perturbation velocity ($\emptyset_x$) is zero. Thus the second integral in the general drag formula becomes zero:

$$\rho_\infty U_\infty^2 \iint_{S_3=S_1} \phi_x (1+\phi_x)\, dS_3 = 0, \quad (2.7)$$

and the gauge pressure is formulated as:

$$p - p_\infty = -\frac{1}{2}\rho_\infty U_\infty^2 \left(\phi_y^2 + \phi_z^2\right). \quad (2.8)$$

As the viscosity effects are neglected, total inviscid drag equation can be written as follows:

$$D = -\rho_\infty U_\infty^2 \iint_{S_2} \phi_x \phi_r\, dS_2 + \frac{1}{2}\rho_\infty U_\infty^2 \iint_{S_2} \left(\phi_y^2 + \phi_z^2\right) dS_3. \quad (2.9)$$

Wave drag can be calculated directly from the mass flow rate change at the side surface of the control volume. Perturbation velocities in the first integral give the velocity

change in side direction, which is the velocity difference at the incremental side surface of the control volume. As these are multiplied with the density and the square of free stream velocity, the total wave drag could be obtained. Hence, wave drag formula is obtained from in Equation (2.10):

$$D_w = -\rho_\infty U_\infty^2 \iint_{S_2} \phi_x \phi_r dS_2. \tag{2.10}$$

The perturbation velocities are directly related to the slope of the discretized aircraft geometry. Thus, Equation (2.10) can be written in terms of geometric parameters by using linear source distribution as [32]:

$$D_w = -\frac{1}{2\pi} \int_0^1 \int_0^1 S''(x) S''(y) \log|x-y| dxdy. \tag{2.11}$$

Far–field linear theory has positive and negative aspects. First, it is simply used for calculations. In addition, singularities can be overcome without sophisticated numerical methods; i.e., pressure calculations at leading edge. As shown in Equation (2.10), induced drag can be separated from wave drag by using far–field linear theory, which provides pure wave drag calculation. Thus, it is useful for area rule optimization with respect to wave drag coefficient. Since the volume of the aircraft is the only contributor to drag formula, aircraft geometry can be directly related to the wave drag coefficient. Hence, aircraft area distribution can be modified in order to minimize wave drag coefficient. On the other hand, the theory does not reflect physics of the flow completely. Therefore, aircraft design could be validated with other methods to ensure the behavior of the flow over aircraft surface.

2.1.3 Fourier Transformation

The Fourier transformation methodology is defined as fitting to a data set or any polynomial sinusoidal function(s). General formulation for the polynomial curve fitting is written as:

$$y = a_0 + a_1 x + a_2 x^2 + ... + a_m x^n. \tag{2.12}$$

The residual is calculated as:

$$S_r = \sum_{i=1}^{n} \left(y_i - a_0 - a_1 x - a_2 x^2 - ... - a_m x^n \right)^2, \tag{2.13}$$

Where y_i is the exact value of the data set corresponding to *x*. When the curve is fit accurately the residual "S_r" is minimized. Thus, gradients of the residual is zero when the curve fitting presents the data set successfully. The gradients are given by:

$$\frac{\partial S_r}{\partial a_0} = -2\sum_{i=1}^{n} \left(y_i - a_0 - a_1 x - a_2 x^2 - ... - a_m x^n \right), \tag{2.14}$$

$$\frac{\partial S_r}{\partial a_1} = -2\sum_{i=1}^{n} x_i \left(y_i - a_0 - a_1 x - a_2 x^2 - ... - a_m x^n \right), \tag{2.15}$$

$$\frac{\partial S_r}{\partial a_2} = -2\sum_{i=1}^{n} x_i^2 \left(y_i - a_0 - a_1 x - a_2 x^2 - ... - a_m x^n \right), \tag{2.16}$$

$$\vdots$$

$$\frac{\partial S_r}{\partial a_n} = -2\sum_{i=1}^{n} x_i^n \left(y_i - a_0 - a_1 x - a_2 x^2 - ... - a_m x^n \right). \tag{2.17}$$

The coefficients are obtained by equating and solving the gradient equations:

$$\begin{gathered}
(n)a_0 + (\sum_{i=1}^{n} x_i)a_1 + (\sum_{i=1}^{n} x_i^2)a_2 + \ldots + (\sum_{i=1}^{n} x_n^m)a_m = \sum_{i=1}^{n} y_i, \\
(\sum_{i=1}^{n} x_i)a_0 + (\sum_{i=1}^{n} x_i^2)a_1 + (\sum_{i=1}^{n} x_i^3)a_2 + \ldots + (\sum_{i=1}^{n} x_n^{m+1})a_m = \sum_{i=1}^{n} x_i y_i, \\
(\sum_{i=1}^{n} x_i^2)a_0 + (\sum_{i=1}^{n} x_i^3)a_1 + (\sum_{i=1}^{n} x_i^4)a_2 + \ldots + (\sum_{i=1}^{n} x_n^{m+2})a_m = \sum_{i=1}^{n} x_i^2 y_i, \\
\vdots \\
(\sum_{i=1}^{n} x_i^n)a_0 + (\sum_{i=1}^{n} x_i^{n+1})a_1 + (\sum_{i=1}^{n} x_i^{n+2})a_2 + \ldots + (\sum_{i=1}^{n} x_n^{m+n})a_m = \sum_{i=1}^{n} x_i^m y_i.
\end{gathered} \tag{2.18}$$

Same approach can be used for the Fourier transformation. The polynomial function can be changed into a sinusoidal function in order to fit the Fourier transformation to the data set. Equation (2.19) shown below presents the first order Fourier model. Application of the transformation is explained in Chapter 3.

$$y = A_0 + A_1 \cos(\omega t) + B_1 \sin(\omega t). \tag{2.19}$$

The residual of the model is given as:

$$S_r = \sum_{i=1}^{n} \left(y_i - A_0 - A_1 \cos(\omega t) - B_1 \sin(\omega t) \right)^2, \tag{2.20}$$

gradients of the residual "S_r" are presented as:

$$\frac{\partial S_r}{\partial A_0} = -2 \sum_{i=1}^{n} \left(y_i - A_0 - A_1 \cos(\omega t) - B_1 \sin(\omega t) \right), \tag{2.21}$$

$$\frac{\partial S_r}{\partial A_1} = -2 \sum_{i=1}^{n} \cos(\omega \mathrm{t}) \left(y_i - A_0 - A_1 \cos(\omega t) - B_1 \sin(\omega t) \right), \tag{2.22}$$

$$\frac{\partial S_r}{\partial A_2} = -2 \sum_{i=1}^{n} \sin(\omega \mathrm{t}) \left(y_i - A_0 - A_1 \cos(\omega t) - B_1 \sin(\omega t) \right). \tag{2.23}$$

The necessary condition for success of the curve fitting operation is that the gradient equations are equal to zero. Then, the unknown coefficients are obtained from the solutions of the set of equations.

2.2 Optimization Method

Several methods have been used for minimizing the wave drag coefficient. The choice of the method, whether it is gradient or non–gradient based algorithms is decided by considering the overall configuration of the optimization problem. Depending on the complexity of the aircraft geometry, and the theory being used for solver of the wave drag phenomenon optimization method is chosen. More information can be found

about the optimization methods used in this study for minimizing wave drag coefficient in the literature [16, 32].

2.2.1 Theory of Lagrange Multipliers

The methodology of Lagrange multiplier is employed for the constrained optimization. This part presents the method used for minimization of wave drag coefficient. A general formulation can be presented as:

$$\min f(x) \quad \text{subject to} \begin{cases} c_i(x) = 0, & i \in \varepsilon \\ c_i(x) \geq 0, & i \in I \end{cases} \tag{2.24}$$

where the both the objective function and the constraints are smooth, real–valued functions. $i \in \varepsilon$ are the equality constraints, $i \in I$ are the inequality constraints [18]. There is more than one local solution for an objective function both for constrained and unconstrained cases. Smoothness of the objective functions and constraints is critical for global convergence. Furthermore, sharp gradients of these functions might mislead the search direction. To avoid that, the functions having sharp edges could be characterized with a collection of smooth functions. Simply, Lagrangian function for one (equality) constraint is shown as:

$$L(x, \lambda) = f(x) - \lambda_1 c_1(x), \tag{2.25}$$

where $f(x)$ is the objective and $c_1(x)$ is the constraint function. The optimality condition is given by:

$$\nabla_x L(x^*, \lambda_1^*) = 0, \qquad \text{for some } \lambda_1^* \geq 0 \tag{2.26}$$

Despite the fact that equation shown above is necessary for optimal solution, it is not sufficient. It is also required that:

$$\lambda_1^* c_1(x^*) = 0. \tag{2.27}$$

Generally, Lagrangian function for the constrained optimization problem is defined as:

$$L(x,\lambda) = f(x) - \sum_{i\epsilon\varepsilon\cup I} \lambda_i c_i(x). \tag{2.28}$$

The active set $A(x)$ at any feasible x is the union of the set ε with the indices of the active inequality constraints [15]. Next, it can be said that the linear independence constraint qualification (*LICQ*) holds if the set of active constraint gradients is linearly independent. Finally, open form of the first–order necessary conditions is written as:

$$\nabla_x L(x^*, \lambda^*) = 0\,, \tag{2.29}$$

$$c_i(x^*) = 0, \quad \text{for all } i \in \varepsilon, \tag{2.30}$$

$$c_i(x^*) \geq 0 \quad \text{for all } i \in I, \tag{2.31}$$

$$\lambda_i^* \geq 0 \qquad \text{for all } i \in I, \tag{2.32}$$

$$\lambda_i^* c_i(x^*) = 0, \quad \text{for all } i \in \varepsilon \cup I. \tag{2.33}$$

The multi–constrained (equality) optimization method is employed for this study. Theory of Lagrange multiplier for related subjects are explained in detail. Considering the case of objective function $f(x,y,z)$ to be minimized with respect to constraints $c_1(x,y,z)$ and $c_2(x,y,z)$, *Lagrangian* function is written as:

$$L(x,y,z,\lambda_1,\lambda_2) = f(x,y,z) - \lambda_1 c_1(x,y,z) - \lambda_2 \, c_2(x,y,z). \tag{2.34}$$

where λ_1 and λ_1 are *Lagrange* multipliers, '*' denotes the optimal condition. The optimality condition is reached when

$$\nabla f(x^*, y^*, z^*) = \lambda_1 \nabla c_1(x^*, y^*, z^*) + \lambda_2 \nabla c_2(x^*, y^*, z^*). \tag{2.35}$$

Open form of the equations are presented as:

$$0 = L_x\left(x^*, y^*, z^*, \lambda_1, \lambda_2\right) = f_x\left(x^*, y^*, z^*\right) - \lambda_1 c_{1_x}\left(x^*, y^*, z^*\right) - \lambda_2 c_{2_x}\left(x^*, y^*, z^*\right), \tag{2.36}$$

$$0 = L_y\left(x^*, y^*, z^*, \lambda_1, \lambda_2\right) = f_y\left(x^*, y^*, z^*\right) - \lambda_1 c_{1_y}\left(x^*, y^*, z^*\right) - \lambda_2 c_{2_y}\left(x^*, y^*, z^*\right), \tag{2.37}$$

$$0 = L_z\left(x^*, y^*, z^*, \lambda_1, \lambda_2\right) = f_z\left(x^*, y^*, z^*\right) - \lambda_1 c_{1_z}\left(x^*, y^*, z^*\right) - \lambda_2 c_{2_z}\left(x^*, y^*, z^*\right), \tag{2.38}$$

$$0 = L_{\lambda_1}\left(x^*, y^*, z^*, \lambda_1, \lambda_2\right) = c_1\left(x^*, y^*, z^*\right), \tag{2.39}$$

$$0 = L_{\lambda_2}\left(x^*, y^*, z^*, \lambda_1, \lambda_2\right) = c_2\left(x^*, y^*, z^*\right). \tag{2.40}$$

CHAPTER 3

NUMERICAL METHODS

This chapter presents the methods used methodologies in the thesis to optimize the wave drag coefficient of high speed aircraft. In this chapter, detailed explanation of the wave drag coefficient calculation, the optimization mid–steps including the constraint definition and the transformation of the objective function from the original formula, three dimensional geometry discretization and filtering methods, arbitrary shaped area calculation, aircraft geometry update as a result of the wave drag coefficient minimization can be found.

3.1 General Algorithm of the Program

The developed program is used for minimizing the wave drag coefficient of a high speed aircraft. The entire process is initialized by inputting the aircraft geometry to the program. Then, the geometry is discretized section by section. The area distribution of the aircraft geometry is filtered out to simplify the procedure and to eliminate the relatively higher CPU cost. In other words, the points representing the aircraft geometry are updated with respect to the optimization result indirectly. The smoothness of the distribution is one of the most important parameters for wave drag calculation. Thus, the curve representing the cross–sectional area distribution is transformed to a Fourier sine function. Optimization loop is entered after initializing the necessary parameters which are explained above. The final step of the program is to update the geometry of the aircraft. Since the optimal area distribution is achieved with respect to the wave drag coefficient, the initial area distribution can be updated by using final (optimal) area distribution. The methodology behind the updating process is that the ratio of the final to the initial area distribution decides how much the final aircraft geometry enlarges or narrows down. Then, the whole configuration

is updated based on this decision with the exceptions for control and lifting surfaces. Figure 7 presents the flowchart of the program.

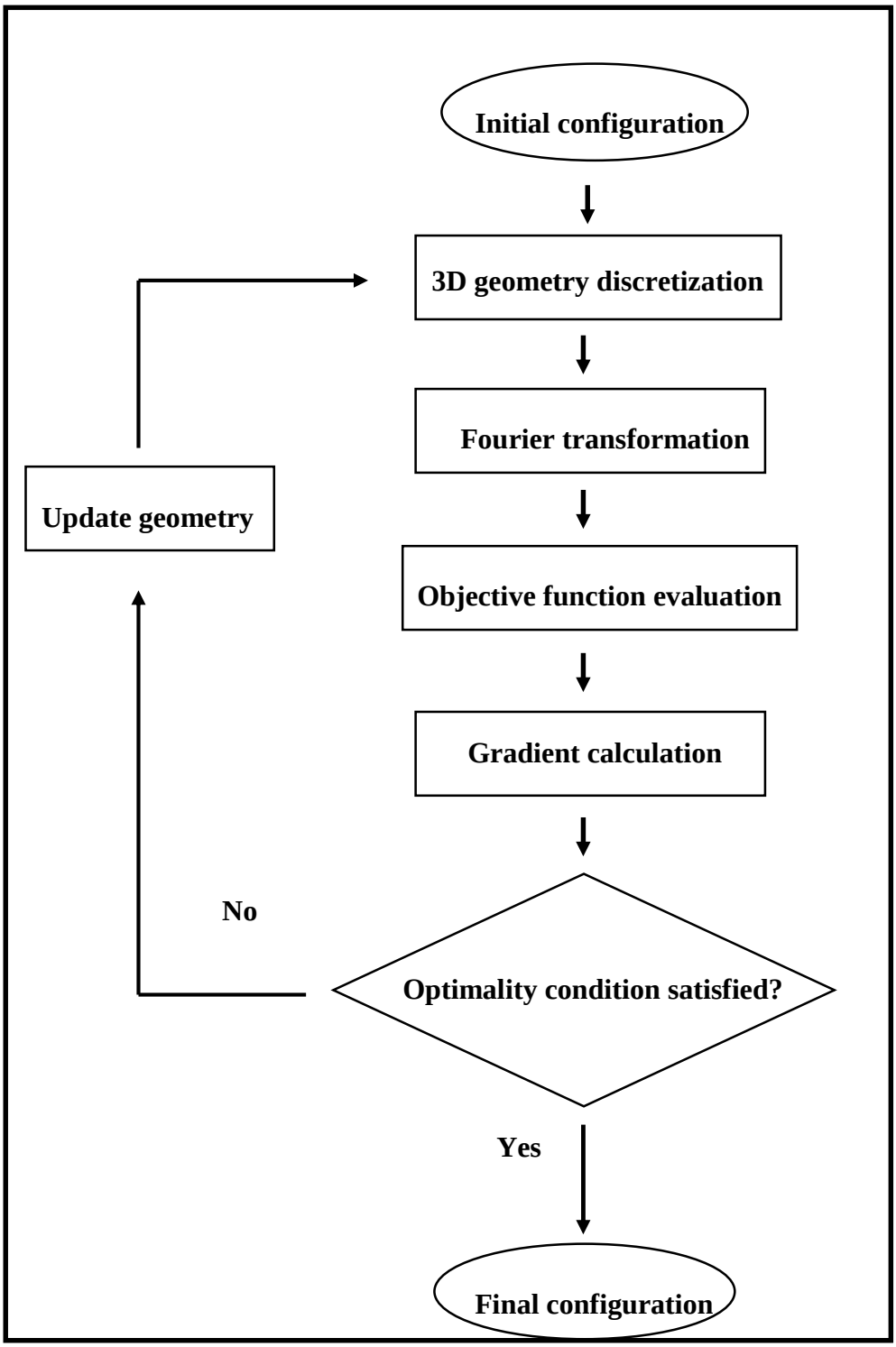

Figure 7-Flowchart of the Program

3.2 Wave Drag Calculation Methodology

Conventional form of the wave drag is given by [32]:

$$D_w = -\frac{1}{2\pi}\int_0^1\int_0^1 S''(x)S''(y)\log|x-y|dxdy. \tag{3.1}$$

Two problems arise in the calculation of the formula given above. Firstly, singularity occurs where the longitudinal locations of the integral become identical, i.e. $x = y$. Secondly, numerical precision strongly depends on the differentiation method used and the degree of accuracy. Thus, sensitivity analysis is made for the calculation of wave drag coefficient.

Two conditions must be satisfied for the method used to obtain wave drag coefficient:

- The first derivative of the area distribution is continuous along longitudinal direction of aircraft.
- The first derivatives of the area distribution at nose and rear regions are equal to zero:

$$S'(0) = S'(1) = 0, \tag{3.2}$$

since the length is non-dimensionalized, '*1*' in Equation (3.2) presents the length of an aircraft. When the conditions explained above are satisfied, the first derivative of the area distribution can be transformed into Fourier sine series as:

$$x = \frac{1}{2}(1-\cos\theta), \tag{3.3}$$

where θ can be written as a function of longitudinal distance:

$$\theta = \cos^{-1}(1-2x), \tag{3.4}$$

where θ varies between 0 and π. Equations (3.3) and (3.4) are implicitly referred. Then the first derivative distribution is given by:

$$S'(\mathrm{x}) = \pi L \sum_{r=1}^{\infty} a_r \sin r\theta, \qquad 0 \leq x \leq 1, \tag{3.5}$$

where the coefficients are written as:

$$a_r = \sum_{r=1}^{\infty} \frac{2}{\pi} \int_0^{\pi} S'(x) r\theta d\theta, \quad \mathrm{r}=1, 2\ldots \tag{3.6}$$

The area distribution of the aircraft is obtained by integrating Equation (3.6):

$$S(x) = \sum_{r=1}^{\infty} a_r \int \sin r\theta dx. \tag{3.7}$$

Equation (3.5) is integrated and substituted into Equation (3.8) by using the derivative of Equation (3.3):

$$dx = -\frac{1}{2} \sin\theta d\theta, \tag{3.8}$$

$$S(x) = \frac{1}{2} \sum_{r=1}^{\infty} a_r \int \sin r\theta \sin\theta d\theta, \tag{3.9}$$

$$= a + \frac{1}{4} a_1 (\theta - \frac{1}{2} \sin 2\theta) + \frac{1}{4} \sum_{r=2}^{\infty} a_r \left[\frac{\sin(r-1)\theta}{r-1} - \frac{\sin(r+1)\theta}{r+1} \right]$$

$$= a + \frac{1}{4} a_1 \theta + \frac{1}{4} \sum_{r=1}^{\infty} (a_r - a_{r-1}) \sin r\theta.$$

By using Equation (3.9), the second derivative of the area distribution is obtained and inserted into Equation (3.1) as:

$$D_w = \frac{1}{2} \int_0^{\pi} \sum_{r=1}^{\infty} r a_r \sin r\theta \sum_{s=1}^{\infty} a_s \sin s\theta d\theta,$$

$$= \frac{1}{2} \sum_{r=1}^{\infty} \sum_{s=1}^{\infty} r a_r a_s \int_0^{\pi} \sin r\theta \sin s\theta d\theta, \tag{3.10}$$

$$= \frac{\pi}{4} \sum_{r=1}^{\infty} r a_r^2 .$$

Gradient based optimization method is used in order to obtain the area distribution which has minimum wave drag coefficient. Since the accuracy of the gradient calculation strictly depends on the smoothness of the objective function and constraints, analytical functions presenting aircraft geometry give more stable results than the non-analytical ones [21].

3.3 Numerical Applications

Additional workload to the main optimization algorithm; namely, discretization, sine transformation, area calculation and point update are necessary to complete the minimization process of the wave drag coefficient. These secondary efforts are essential in order to transfer the three dimensional geometry from sketching program to the optimization process, fitting the cross–sectional area distribution as input to the program, calculating both for cross sectional and lateral areas, and updating the results of each optimization step to visualize the geometrical effects of the minimization. The subjects mentioned above are annotated in the following headings.

3.3.1 Discretization of the Geometry

The initial configuration of the aircraft is obtained from *OpenVSP* [11]. It is an open source vehicle sketch pad since 2012. Most aerodynamic characteristics affecting the aircraft design process are used in the program parametrically.

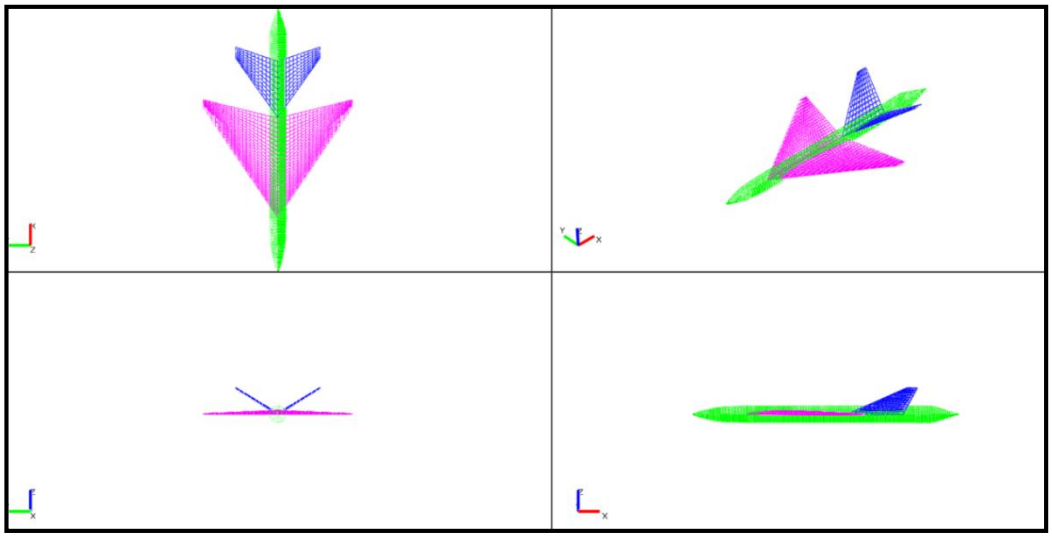

Figure 8 – Configuration 4

Figure 8 presents the *OpenVSP* [11] view of one of the configurations studied in this thesis.

3.3.2 Sine Transformation

In this section, first derivative of the cross–sectional area distribution is transformed into a Fourier sine function. The reason of this process is that the first derivative of cross–sectional area distribution must be continuous according to the wave drag calculation methodology. Equation (3.11) presents the open form of the sine function. In addition, smoothness is one of the most important criteria for minimization procedure. Thus, representation of real cross–sectional area distribution must be accurate enough. Furthermore, value of the error function shown in Equation (3.12), does not reduce linearly. Therefore, to keep CPU at a certain level and to obtain an accurate representation, fourth order sine functions are chosen.

$$y = a_0 + a_1\cos(x) + b_1\sin(x) + a_2\cos(2x) + b_2\sin(2x) \\ +a_3\cos(3x) + b_3\sin(3x) + a_4\cos(4x) + b_4\sin(4x). \tag{3.10}$$

Function 'S_r'' gives the difference between discrete data and the approximated function.

$$S_r^{'} = \sum_{i=1}^{N} \{y_i - y\}^2. \tag{3.11}$$

Thus, this fit of the curve accuracy has to be optimized. Thus, gradients of the residual is zero when the curve fitting presents the data set successfully. The gradients are given by:

$$\frac{\partial S_r^{'}}{\partial a_o}, \frac{\partial S_r^{'}}{\partial a_1}, \frac{\partial S_r^{'}}{\partial a_2}, \frac{\partial S_r^{'}}{\partial a_3}, \frac{\partial S_r^{'}}{\partial a_4}, \frac{\partial S_r^{'}}{\partial b_1}, \frac{\partial S_r^{'}}{\partial b_2}, \frac{\partial S_r^{'}}{\partial b_3}, \frac{\partial S_r^{'}}{\partial b_4} = 0. \tag{3.12}$$

Open form of the gradients are defined as:

$$\frac{\partial S_r^{'}}{\partial a_o} = 2\left(y_i - \left(\begin{matrix} a_0 + a_1\cos(x) + b_1\sin(x) + a_2\cos(2x) + b_2\sin(2x) + \\ a_3\cos(3x) + b_3\sin(3x) + a_4\cos(4x) + b_4\sin(4x) \end{matrix} \right) \right) = 0, \tag{3.13}$$

$$\frac{\partial S_r^{'}}{\partial a_1} = 2\left(y_i - \left(\begin{matrix} a_0 + a_1\cos(x) + b_1\sin(x) + a_2\cos(2x) \\ +b_2\sin(2x) + a_3\cos(3x) + b_3\sin(3x) \\ +a_4\cos(4x) + b_4\sin(4x) \end{matrix} \right) \right)\left(\cos(\mathrm{x})\right) = 0, \tag{3.14}$$

$$\frac{\partial S_r^{'}}{\partial a_2} = 2\left(y_i - \left(\begin{matrix} a_0 + a_1\cos(x) + b_1\sin(x) + a_2\cos(2x) \\ +b_2\sin(2x) + a_3\cos(3x) + b_3\sin(3x) \\ +a_4\cos(4x) + b_4\sin(4x) \end{matrix} \right) \right)\left(\cos(2\,\mathrm{x})\right) = 0, \tag{3.15}$$

$$\frac{\partial S_r^{'}}{\partial a_3} = 2\left(y_i - \left(\begin{matrix} a_0 + a_1\cos(x) + b_1\sin(x) + a_2\cos(2x) \\ +b_2\sin(2x) + a_3\cos(3x) + b_3\sin(3x) \\ +a_4\cos(4x) + b_4\sin(4x) \end{matrix} \right) \right)\left(\cos(3\,\mathrm{x})\right) = 0, \tag{3.16}$$

$$\frac{\partial S_r^{'}}{\partial a_4} = 2\left(y_i - \left(\begin{matrix} a_0 + a_1\cos(x) + b_1\sin(x) + a_2\cos(2x) \\ +b_2\sin(2x) + a_3\cos(3x) + b_3\sin(3x) \\ +a_4\cos(4x) + b_4\sin(4x) \end{matrix} \right) \right)\left(\cos(4x)\right) = 0, \tag{3.17}$$

$$\frac{\partial S_r^{'}}{\partial b_1} = 2\left(y_i - \left(\begin{matrix} a_0 + a_1\cos(x) + b_1\sin(x) + a_2\cos(2x) \\ +b_2\sin(2x) + a_3\cos(3x) + b_3\sin(3x) \\ +a_4\cos(4x) + b_4\sin(4x) \end{matrix} \right) \right)\left(\sin(\mathrm{x})\right) = 0, \tag{3.18}$$

$$\frac{\partial S_r^{'}}{\partial b_2} = 2\left(y_i - \begin{pmatrix} a_0 + a_1\cos(x) + b_1\sin(x) + a_2\cos(2x) \\ +b_2\sin(2x) + a_3\cos(3x) + b_3\sin(3x) \\ +a_4\cos(4x) + b_4\sin(4x) \end{pmatrix} \right)\left(\sin(2\,\mathrm{x})\right) = 0, \qquad (3.19)$$

$$\frac{\partial S_r^{'}}{\partial b_3} = 2\left(y_i - \begin{pmatrix} a_0 + a_1\cos(x) + b_1\sin(x) + a_2\cos(2x) \\ +b_2\sin(2x) + a_3\cos(3x) + b_3\sin(3x) \\ +a_4\cos(4x) + b_4\sin(4x) \end{pmatrix} \right)\left(\sin(3\,\mathrm{x})\right) = 0, \qquad (3.20)$$

$$\frac{\partial S_r^{'}}{\partial b_4} = 2\left(y_i - \begin{pmatrix} a_0 + a_1\cos(x) + b_1\sin(x) + a_2\cos(2x) \\ +b_2\sin(2x) + a_3\cos(3x) + b_3\sin(3x) \\ +a_4\cos(4x) + b_4\sin(4x) \end{pmatrix} \right)\left(\sin(4\,\mathrm{x})\right) = 0. \qquad (3.21)$$

3.3.3 Area Calculation

Green's theorem is used for the calculation of cross–sectional area [20]. The incremental area *dA* is defined as:

$$dA = dxdy, \qquad (3.22)$$

It states that area *A* of a closed region *D* can be presented as:

$$A = \iint_D dA. \qquad (3.23)$$

M and *L* are functions having continuous partial derivatives defined by the boundaries of *D*.

$$\frac{\partial M}{\partial x} - \frac{\partial L}{\partial y} = 1, \qquad (3.24)$$

where *M* and *L* are functions having continuous partial derivatives defined by the boundaries of *D*. The area *A* is given by:

$$A = \oint_C (Ldx + Mdy). \qquad (3.25)$$

The final form of the area formula can be written as:

$$A = \frac{1}{2}\oint_C (-ydx + xdy). \tag{3.26}$$

Area computation for each cross–section is necessary as being inputs to the solver, since the shape of the cross–sections are arbitrary with variable number of points. Equation (3.28) is used to calculate this area. Figure 9 indicates an arbitrary shaped cross section.

$$S = \frac{1}{2}\sum_{i=1}^{n-1} y_i x_{i+1} - y_{i+1} x_i. \tag{3.27}$$

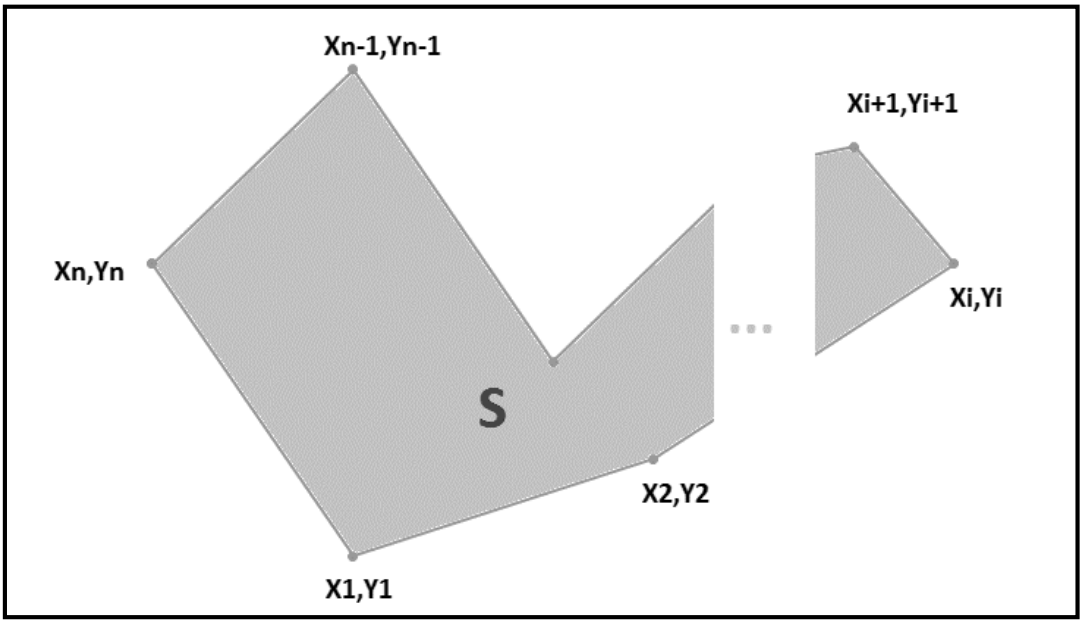

Figure 9–Arbitrary shaped cross–section

3.3.4 Optimization Procedure

Since the area distribution is defined in two different sine functions, which are linearly independent, wave drag formula is transformed into Equation (3.29) (a_0 presents the nose area which is equal to zero):

$$D_w = \sum_{n=1}^{\infty} n a_n^2 + n b_n^2. \tag{3.28}$$

The coefficients 'a_n' and 'b_n' above are the parameters in the Fourier transformation. The permanent constraint function which defines the total volume of the aircraft is defined as:

$$V = \frac{1}{2}\sum_{i=1}^{n-1}\left(y_{i+1} + y_i\right)\times\left(x_{i+1} - x_i\right), \tag{3.29}$$

where *y* represents the Fourier transformation of the area distribution. The volume function is created by using the simple trapezoid rule. Second constraint function is generated for keeping the i^{th} cross – sectional area constant. Equation (3.31) shows the constraint function of the area:

$$S_i = S_c. \tag{3.30}$$

In open form, Equation (3.29) and (3.30) are written as:

$$\begin{aligned} C_1 = \frac{1}{8}\sum_{i=1}^{n-1}\Big[& a_1\theta + a_2\sin\theta + (a_3 - a_1)\sin 2\theta + (a_4 - a_2)\sin 3\theta + \\ & b_1\theta + a_2\cos\theta + (\mathrm{b}_3 - b_1)\cos 2\theta + (\mathrm{b}_4 - b_2)\cos 3\theta \Big] \\ \times & \left(x_{i+1} - x_i\right) - V = 0, \end{aligned} \tag{3.31}$$

$$C_2 = \begin{pmatrix} a_1\theta + a_2\sin\theta + (a_3 - a_1)\sin 2\theta + (a_4 - a_2)\sin 3\theta + \\ b_1\theta + a_2\cos\theta + (\mathrm{b}_3 - b_1)\cos 2\theta + (\mathrm{b}_4 - b_2)\cos 3\theta \end{pmatrix} - S_c = 0. \tag{3.32}$$

Lagrangian functions are given by:

$$\begin{aligned} 0 = & L(\mathrm{a}_1, \mathrm{a}_2, \mathrm{a}_3, \mathrm{a}_4, \mathrm{b}_1, \mathrm{b}_2, \mathrm{b}_3, \mathrm{b}_4, \lambda_1, \lambda_2)_{a_1} = f_{a_1}(\mathrm{a}_1, \mathrm{a}_2, \mathrm{a}_3, \mathrm{a}_4, \mathrm{b}_1, \mathrm{b}_2, \mathrm{b}_3, \mathrm{b}_4) \\ & -\lambda_1 \mathrm{C}_{1_{a1}}(\mathrm{a}_1, \mathrm{a}_2, \mathrm{a}_3, \mathrm{a}_4, \mathrm{b}_1, \mathrm{b}_2, \mathrm{b}_3, \mathrm{b}_4) - \lambda_2 \mathrm{C}_{2_{a1}}(\mathrm{a}_1, \mathrm{a}_2, \mathrm{a}_3, \mathrm{a}_4, \mathrm{b}_1, \mathrm{b}_2, \mathrm{b}_3, \mathrm{b}_4), \end{aligned} \tag{3.33}$$

$$\begin{aligned} 0 = & L(\mathrm{a}_1, \mathrm{a}_2, \mathrm{a}_3, \mathrm{a}_4, \mathrm{b}_1, \mathrm{b}_2, \mathrm{b}_3, \mathrm{b}_4, \lambda_1, \lambda_2)_{a_2} = f_{a_2}(\mathrm{a}_1, \mathrm{a}_2, \mathrm{a}_3, \mathrm{a}_4, \mathrm{b}_1, \mathrm{b}_2, \mathrm{b}_3, \mathrm{b}_4) \\ & -\lambda_1 \mathrm{C}_{1_{a2}}(\mathrm{a}_1, \mathrm{a}_2, \mathrm{a}_3, \mathrm{a}_4, \mathrm{b}_1, \mathrm{b}_2, \mathrm{b}_3, \mathrm{b}_4) - \lambda_2 \mathrm{C}_{2_{a2}}(\mathrm{a}_1, \mathrm{a}_2, \mathrm{a}_3, \mathrm{a}_4, \mathrm{b}_1, \mathrm{b}_2, \mathrm{b}_3, \mathrm{b}_4), \end{aligned} \tag{3.34}$$

$$0 = L(a_1, a_2, a_3, a_4, b_1, b_2, b_3, b_4, \lambda_1, \lambda_2)_{a_3} = f_{a_3}(a_1, a_2, a_3, a_4, b_1, b_2, b_3, b_4) \\ -\lambda_1 C_{1_{a3}}(a_1, a_2, a_3, a_4, b_1, b_2, b_3, b_4) - \lambda_2 C_{2_{a3}}(a_1, a_2, a_3, a_4, b_1, b_2, b_3, b_4), \tag{3.35}$$

$$0 = L(a_1, a_2, a_3, a_4, b_1, b_2, b_3, b_4, \lambda_1, \lambda_2)_{a_4} = f_{a_4}(a_1, a_2, a_3, a_4, b_1, b_2, b_3, b_4) \\ -\lambda_1 C_{1_{a4}}(a_1, a_2, a_3, a_4, b_1, b_2, b_3, b_4) - \lambda_2 C_{2_{a4}}(a_1, a_2, a_3, a_4, b_1, b_2, b_3, b_4), \tag{3.36}$$

$$0 = L(a_1, a_2, a_3, a_4, b_1, b_2, b_3, b_4, \lambda_1, \lambda_2)_{b_1} = f_{b_1}(a_1, a_2, a_3, a_4, b_1, b_2, b_3, b_4) \\ -\lambda_1 C_{1_{b1}}(a_1, a_2, a_3, a_4, b_1, b_2, b_3, b_4) - \lambda_2 C_{2_{b1}}(a_1, a_2, a_3, a_4, b_1, b_2, b_3, b_4), \tag{3.37}$$

$$0 = L(a_1, a_2, a_3, a_4, b_1, b_2, b_3, b_4, \lambda_1, \lambda_2)_{b_2} = f_{b_2}(a_1, a_2, a_3, a_4, b_1, b_2, b_3, b_4) \\ -\lambda_1 C_{1_{b2}}(a_1, a_2, a_3, a_4, b_1, b_2, b_3, b_4) - \lambda_2 C_{2_{b2}}(a_1, a_2, a_3, a_4, b_1, b_2, b_3, b_4), \tag{3.38}$$

$$0 = L(a_1, a_2, a_3, a_4, b_1, b_2, b_3, b_4, \lambda_1, \lambda_2)_{b_3} = f_{b_3}(a_1, a_2, a_3, a_4, b_1, b_2, b_3, b_4) \\ -\lambda_1 C_{1_{b3}}(a_1, a_2, a_3, a_4, b_1, b_2, b_3, b_4) - \lambda_2 C_{2_{b3}}(a_1, a_2, a_3, a_4, b_1, b_2, b_3, b_4), \tag{3.39}$$

$$0 = L(a_1, a_2, a_3, a_4, b_1, b_2, b_3, b_4, \lambda_1, \lambda_2)_{b_4} = f_{b_4}(a_1, a_2, a_3, a_4, b_1, b_2, b_3, b_4) \\ -\lambda_1 C_{1_{b4}}(a_1, a_2, a_3, a_4, b_1, b_2, b_3, b_4) - \lambda_2 C_{2_{b4}}(a_1, a_2, a_3, a_4, b_1, b_2, b_3, b_4), \tag{3.40}$$

$$0 = L(a_1, a_2, a_3, a_4, b_1, b_2, b_3, b_4, \lambda_1, \lambda_2)_{\lambda_1} = C_1, \tag{3.41}$$

$$0 = L(a_1, a_2, a_3, a_4, b_1, b_2, b_3, b_4, \lambda_1, \lambda_2)_{\lambda_2} = C_2. \tag{3.42}$$

Partial derivatives of the objective function and the constraint functions are given in Equations (3.44), (3.45), and (3.46) as:

$$\begin{bmatrix} \frac{\partial F}{\partial a_1} \\ \frac{\partial F}{\partial a_2} \\ \frac{\partial F}{\partial a_3} \\ \frac{\partial F}{\partial a_4} \\ \frac{\partial F}{\partial b_1} \\ \frac{\partial F}{\partial b_2} \\ \frac{\partial F}{\partial b_3} \\ \frac{\partial F}{\partial b_4} \end{bmatrix} = \begin{bmatrix} \sum_{r=1}^{4} 2ra_r \\ \sum_{r=2}^{4} 2ra_r \\ \sum_{r=3}^{4} 2ra_r \\ \sum_{r=4}^{4} 2ra_r \\ \sum_{r=1}^{4} 2rb_r \\ \sum_{r=2}^{4} 2rb_r \\ \sum_{r=3}^{4} 2rb_r \\ \sum_{r=4}^{4} 2rb_r \end{bmatrix}, \tag{3.43}$$

$$\begin{bmatrix} \frac{\partial C_1}{\partial a_1} \\ \frac{\partial C_1}{\partial a_2} \\ \frac{\partial C_1}{\partial a_3} \\ \frac{\partial C_1}{\partial a_4} \\ \frac{\partial C_1}{\partial b_1} \\ \frac{\partial C_1}{\partial b_2} \\ \frac{\partial C_1}{\partial b_3} \\ \frac{\partial C_1}{\partial b_4} \end{bmatrix} = \begin{bmatrix} \frac{1}{8}\sum_{i=1}^{n-1}\left[\cos^{-1}(1-2x)-\sin(2(\cos^{-1}(1-2x))\right](x_{i+1}-x_i) \\ \frac{1}{8}\sum_{i=1}^{n-1}\left[\sin((\cos^{-1}(1-2x)-\sin(3(\cos^{-1}(1-2x)\right](x_{i+1}-x_i) \\ \frac{1}{8}\sum_{i=1}^{n-1}\left[\sin(2(\cos^{-1}(1-2x)\right](x_{i+1}-x_i) \\ \frac{1}{8}\sum_{i=1}^{n-1}\left[\sin(3(\cos^{-1}(1-2x)\right](x_{i+1}-x_i) \\ \frac{1}{8}\sum_{i=1}^{n-1}\left[\cos^{-1}(1-2x)-\cos(2\cos^{-1}(1-2x))\right](x_{i+1}-x_i) \\ \frac{1}{8}\sum_{i=1}^{n-1}\left[\cos(\cos^{-1}(1-2x))-\cos(3\cos^{-1}(1-2x))\right](x_{i+1}-x_i) \\ \frac{1}{8}\sum_{i=1}^{n-1}\left[\cos(2\cos^{-1}(1-2x))\right](x_{i+1}-x_i) \\ \frac{1}{8}\sum_{i=1}^{n-1}\left[\cos(3\cos^{-1}(1-2x))\right](x_{i+1}-x_i) \end{bmatrix}, \tag{3.44}$$

$$\begin{bmatrix} \frac{\partial C_2}{\partial a_1} \\ \frac{\partial C_2}{\partial a_2} \\ \frac{\partial C_2}{\partial a_3} \\ \frac{\partial C_2}{\partial a_4} \\ \frac{\partial C_2}{\partial b_1} \\ \frac{\partial C_2}{\partial b_2} \\ \frac{\partial C_2}{\partial b_3} \\ \frac{\partial C_2}{\partial b_4} \end{bmatrix} = \begin{bmatrix} \frac{1}{4}\left[\cos^{-1}(1-2x)-\sin(2(\cos^{-1}(1-2x))\right] \\ \frac{1}{4}\left[\sin(\cos^{-1}(1-2x))-\sin(3(\cos^{-1}(1-2x))\right] \\ \frac{1}{4}\sin(2(\cos^{-1}(1-2x)) \\ \frac{1}{4}\sin(3(\cos^{-1}(1-2x)) \\ \frac{1}{4}\left[(\cos^{-1}(1-2x)-\cos(2((\cos^{-1}(1-2x)))\right] \\ \frac{1}{4}\left[\cos((\cos^{-1}(1-2x))-\cos(2((\cos^{-1}(1-2x)))\right] \\ \frac{1}{4}\cos(2(\cos^{-1}(1-2x)) \\ \frac{1}{4}\cos(3(\cos^{-1}(1-2x) \end{bmatrix}. \tag{3.45}$$

Equation (3.47) is solved iteratively to obtain optimum values by using partial derivatives presented above. In order to reach the optimality conditions, search

direction is utilized to update the iteration algorithm. The search direction is obtained from:

$$\nabla f(a_1, a_2, a_3, a_4, b_1, b_2, b_3, b_4, \lambda_1, \lambda_2) = \lambda_1 C_1(a_1, a_2, a_3, a_4, b_1, b_2, b_3, b_4) + \lambda_2 C_2(a_1, a_2, a_3, a_4, b_1, b_2, b_3, b_4). \quad (3.46)$$

The convergence criterion is satisfied as soon as $\|\nabla L\|_2 \leq \varepsilon$ at the regarded point, for some given $\varepsilon > 0$.

It can be emphasized that, the objective function is strictly convex, guaranteeing that the candidate solution is a real solution. Theoretically, the upper bound of the summation term in wave drag formula, Equation (3.10), is infinite to simulate aircraft geometry by using Fourier transformation without losing accuracy. On the other hand, it is impossible to represent an aircraft geometry with a very large number of Fourier coefficients due to round-off error, thereby, CPU usage becomes unnecessarily huge. Practically, representation with two to four coefficients which leads to ten linearly independent set of equations to be solved is accurate enough to represent a continuous (both area and the first derivative of the area distribution) aircraft geometry. For this reason, convexity of the objective function is examined for definite number of coefficients. Let $D \subseteq R^n$ be open and convex, and let $f: C \rightarrow R$ have continuous first partial derivatives on *D.* Then any critical point of $f(x)$ in *D* is a global minimizer of $f(x)$ on *D.* Related theorem for the objective function used in this study with respect to correlation explained above is that if Hessian $H\ f(x)$ is positive definite on an interval *D,* then $f(x)$ is strictly convex on *D* [28]. The objective function is analyzed in order to analyze the strictly convexity for three different upper bounds. It explains the generic formation of the solution of the objective function is real minimizer. The objective function is given by:

$$D_w = \frac{\pi}{4} \sum_{r=1}^{\infty} r a_r^2. \quad (3.47)$$

The formation of the objective function for upper bound equal to one is written as:

$$D_w = \frac{\pi}{4}\sum_{r=1}^{1} r a_r^2 = \frac{\pi}{4} a_1^2. \tag{3.48}$$

Partial derivative and Hessian are obtained as:

$$\frac{\partial D_w}{\partial a_1} = \frac{\pi}{2} a_1, \tag{3.49}$$

$$\frac{\partial^2 D_w}{\partial a_1^2} = \frac{\pi}{2}. \tag{3.50}$$

The formation of the objective function for upper bound equal to two is written as:

$$D_w = \frac{\pi}{4}\sum_{r=1}^{2} r a_r^2 = \frac{\pi}{4}\left(a_1^2 + 2a_2^2\right). \tag{3.51}$$

Partial derivatives are obtained as:

$$\frac{\partial^2 D_w}{\partial a_1^2} = \frac{\pi}{2}, \tag{3.52}$$

$$\frac{\partial^2 D_w}{\partial a_1 \partial a_2} = \frac{\partial^2 D_w}{\partial a_2 \partial a_1} = 0, \tag{3.53}$$

$$\frac{\partial^2 D_w}{\partial a_2^2} = \pi, \tag{3.54}$$

Hessian $H\ D_w$ is written as:

$$H = \begin{bmatrix} \frac{\pi}{2} & 0 \\ 0 & \pi \end{bmatrix}. \tag{3.55}$$

The formation of the objective function for upper bound equal to three is written as:

$$D_w = \frac{\pi}{4}\sum_{r=1}^{3} r a_r^2 = \frac{\pi}{4}\left(a_1^2 + 2a_2^2 + 3a_3^2\right). \tag{3.56}$$

Partial derivatives and Hessian are given by:

$$\frac{\partial^2 D_w}{\partial a_1^2} = \frac{\pi}{2}, \tag{3.57}$$

$$\frac{\partial^2 D_w}{\partial a_2^2} = \pi, \tag{3.58}$$

$$\frac{\partial^2 D_w}{\partial a_3^2} = \frac{3\pi}{2}, \tag{3.59}$$

$$\frac{\partial^2 D_w}{\partial a_1 \partial a_2} = \frac{\partial^2 D_w}{\partial a_2 \partial a_1} = \frac{\partial^2 D_w}{\partial a_1 \partial a_3} = \frac{\partial^2 D_w}{\partial a_3 \partial a_1} = \frac{\partial^2 D_w}{\partial a_3 \partial a_2} = \frac{\partial^2 D_w}{\partial a_2 \partial a_3} = 0. \tag{3.60}$$

Hessian $H\ D_w$ is written as:

$$H = \frac{\pi}{4}\begin{bmatrix} 2 & 0 & 0 \\ 0 & 4 & 0 \\ 0 & 0 & 6 \end{bmatrix}. \tag{3.61}$$

The domain of the objective function *D* must have continuous area and first derivative of area distribution due to linearized far-field theory. For three different cases (upper bound equal to 1, 2, and 3), Hessian *H* is positive definite on *D.* Then, it can be said that the objective function, D_w is strictly convex.

3.3.5 Point Update

Updating the points after the optimization step is the final step of the program. Simple methodology is used for this work. Initial cross–sectional area magnitude at i^{th} location S_{init_i} is calculated as explained in the previous section. Then, optimal cross–

sectional area magnitude S_{opt_i} is obtained after the optimization process. Ratio R_i is defined as:

$$S_{opt_i} = S_{init_i} + \Delta S_i, \tag{3.62}$$

$$R_i = \sqrt{\frac{S_{opt_i}}{S_{init_i}}}. \tag{3.63}$$

Initial x and y locations, j^{th}order of i^{th}section; $P_{Xij_{init}}$ and $P_{Yij_{init}}$ are updated as follows:

$$Px_{ij_{opt}} = R_i \times Px_{ij_{init}}, \tag{3.64}$$

$$Py_{ij_{opt}} = R_i \times Py_{ij_{init}}. \tag{3.65}$$

All cross–sections except for the stabilizing and the lifting surfaces are updated as explained above. The idea behind the use of ratio R_i is that the slope of the points belonging to the same cross–section is kept constant. The slopes of $P_{ij_{init}}$ and $P_{ij_{opt}}$ can be written as:

$$C_{ij_{init}} = \frac{Py_{ij_{init}}}{Px_{ij_{init}}}, C_{ij_{opt}} = \frac{Py_{ij_{opt}}}{Px_{ij_{opt}}}, \tag{3.66}$$

and

$$C_{ij_{opt}} = C_{ij_{init}} = \frac{Py_{ij_{init}} \times R_i}{Px_{ij_{init}} \times R_i}. \tag{3.67}$$

To illustrate, Figure 10 presents the methodology for the point update. Assuming that the final cross–sectional area is less than the initial area; then, the slope of the point can be kept constant, and updated with respect to ratio of optimal and initial cross–sectional area. Thus, the shape of the geometry is protected which means that the initial conceptual design criteria is kept.

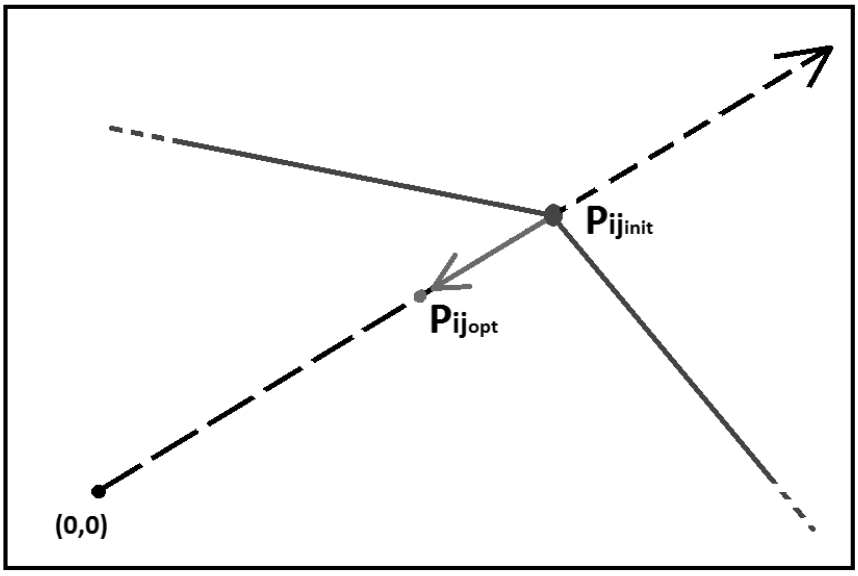

Figure 10–Point Update Presentation

Furthermore, some additional steps must be investigated for non–symmetric cases. The center of the cross section must be found. Theoretically, x_c and y_c are the coordinates of the centroids of the j^{th} cross-section:

$$x_{c_j} = \frac{1}{n}\sum_{i=1}^{n} x_{init}, \tag{3.68}$$

$$y_{c_j} = \frac{1}{n}\sum_{i=1}^{n} y_{init}. \tag{3.69}$$

The slopes of each point in the non–symmetric cross–section are:

$$C_{ij_{init}} = \frac{y_{init} - y_{c_j}}{x_{init} - x_{c_j}}, \tag{3.70}$$

since the slope is kept constant, two unknowns and two equations arise:

$$C_{ij_{opt}} = \frac{y_{opt} - y_{c_j}}{x_{opt} - x_{c_j}}, \tag{3.71}$$

$$\sqrt{\left(x_{init}-x_{cj}\right)^2+\left(y_{init}-y_{cj}\right)^2}\times R=\sqrt{\left(x_{opt}-x_{cj}\right)^2+\left(y_{opt}-y_{cj}\right)^2}. \qquad (3.72)$$

The coordinates of the optimal form of the cross–sectional area distribution can be obtained by solving Equation (3.72) and (3.73). This approach allows the analysis of more realistic configurations.

CHAPTER 4

RESULTS AND DISCUSSION

In this chapter, results are examined in four sub-subjects. First, the validation of the solver is completed by analyzing two different shapes whose wave drag coefficients are known. Sears–Haack slender body and F-16 [29] area distributions are analyzed with computational fluid dynamics methods and compared with values acquired from the literature. Then, test cases are defined and input to the program since the solver is validated with satisfactory results. Finally, the optimal forms of the configurations are presented and compared.

4.1 Validation of the Solver with CFD Analysis

Solver used for the calculation of the wave drag force and coefficient is validated with CFD results. First, Sears–Haack slender body is analyzed with 8 different velocities ranging from Mach 0.85 to Mach 2. Secondly, the wave drag coefficient of the F-16 at Mach 2 is obtained for comparison with Rallabhandi's result [8]. The main reason of conducting CFD simulations is to compare results of the previous studies with those of the present study. Mesh independency for all simulations are obtained by trying different mesh resolutions.

4.1.1 Sears–Haack Slender Body

Despite the fact that the wave drag coefficient of the S-H slender body is independent of Mach number theoretically, results obtained from CFD analysis show that wave drag coefficient increases approaching to Mach 1. Figure 11 presents the shape of the S–H slender body which is known as the body having the smallest wave drag coefficient for a given length and volume.

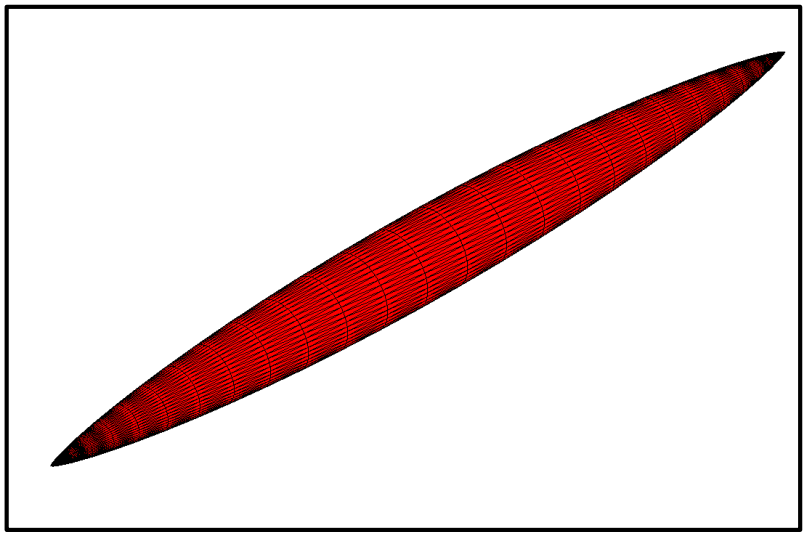

Figure 11–Sears–Haack Slender Body [8]

Geometric parameters of the body that are studied in the present thesis are given in Table 1.

Table 1–Geometric Parameters of S–H Slender Body

volume	$100m^3$
length	30 m
ref. area	5.65 m^2

Results presented below belongs to Mach 1 and 2. Main difference between the cases are the characteristics of compressibility effects on the S–H slender body. It is expected that wave drag coefficient increases as Mach number increases, at subsonic speed up to Mach number equal to 1. At supersonic speed, a reduction is expected.

Figures 12, 13, and 14 show the static pressure, Mach number and density contour plots of the S–H slender body at Mach=2.

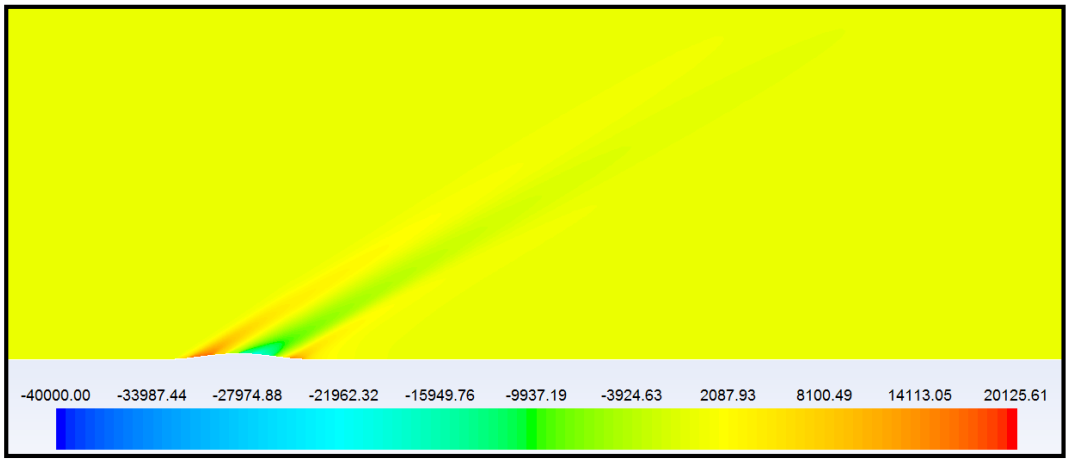

Figure 12–S–H Slender Body Static Pressure Distribution at Mach=2 [Pa]

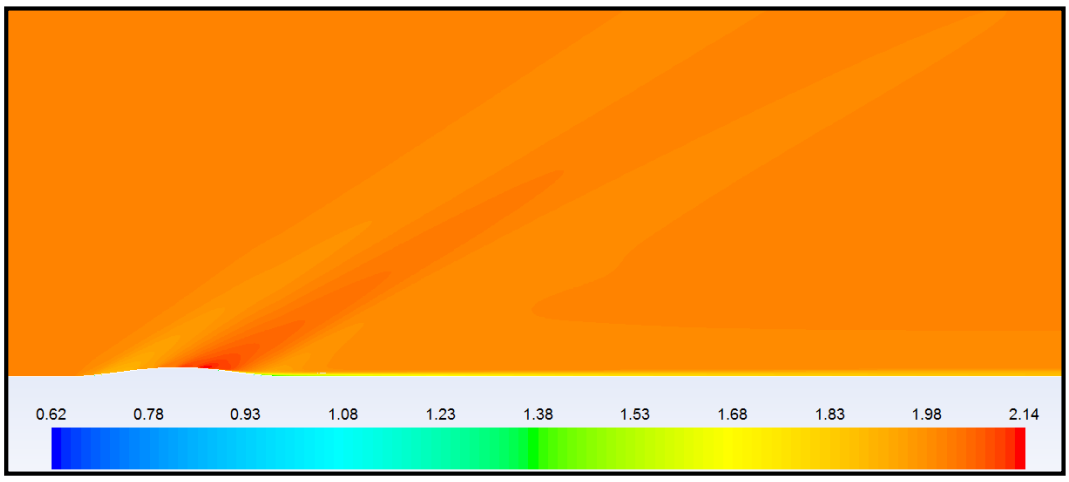

Figure 13-S–H Slender Body Mach Contours at Mach=2

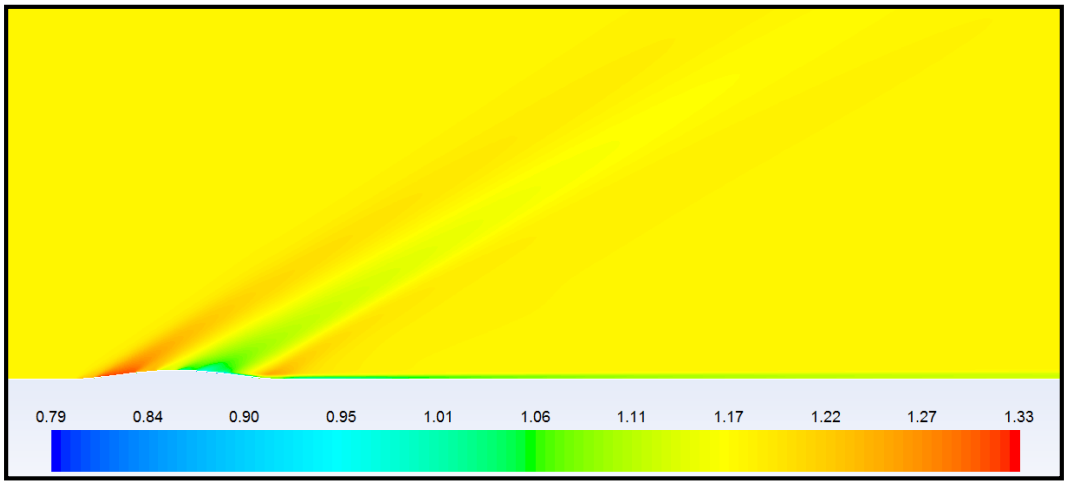

Figure 14-S–H Slender Body Density Contours at Mach =2 [kg/m^3]

The contours of static pressure, Mach number and density are given in Figures 15, 16, and 17.

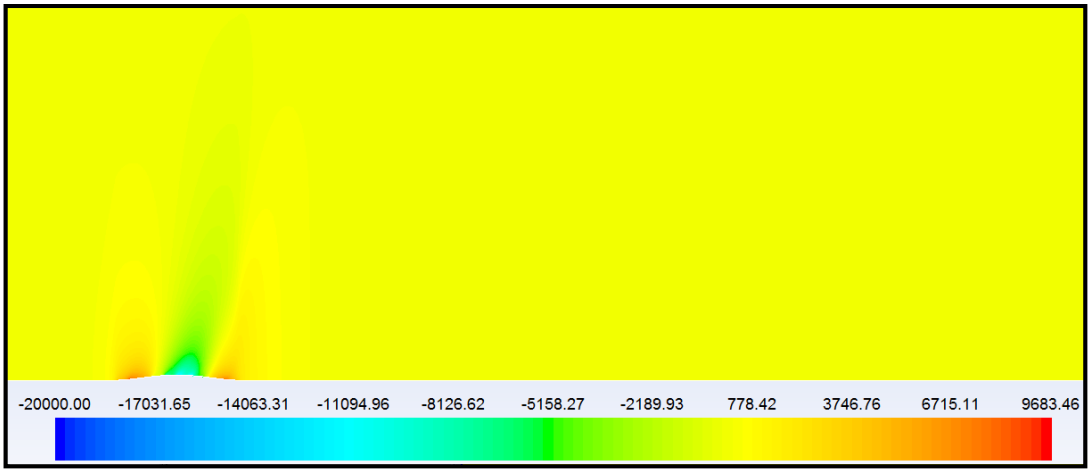

Figure 15–S-H Slender Body Static Pressure Contours at Mach=1 [Pa]

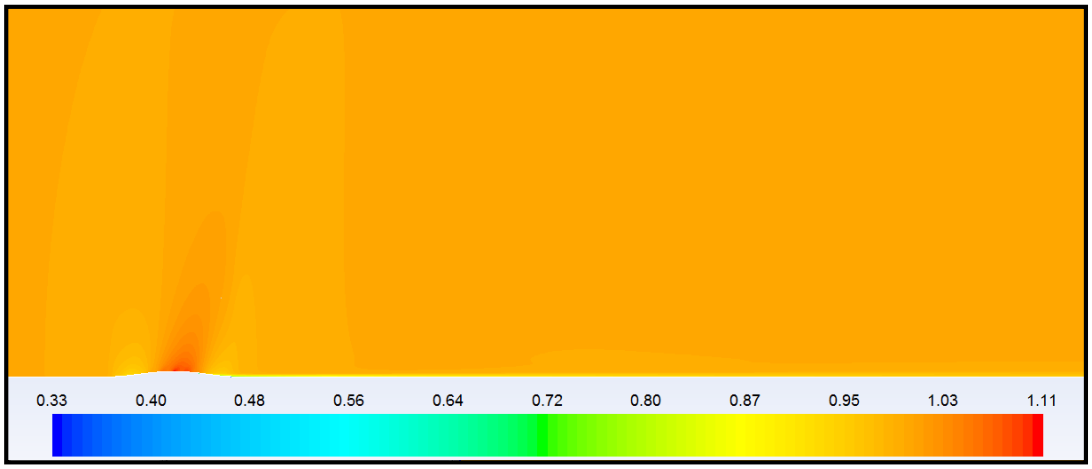

Figure 16–S–H Slender Body Mach contours at Mach=1

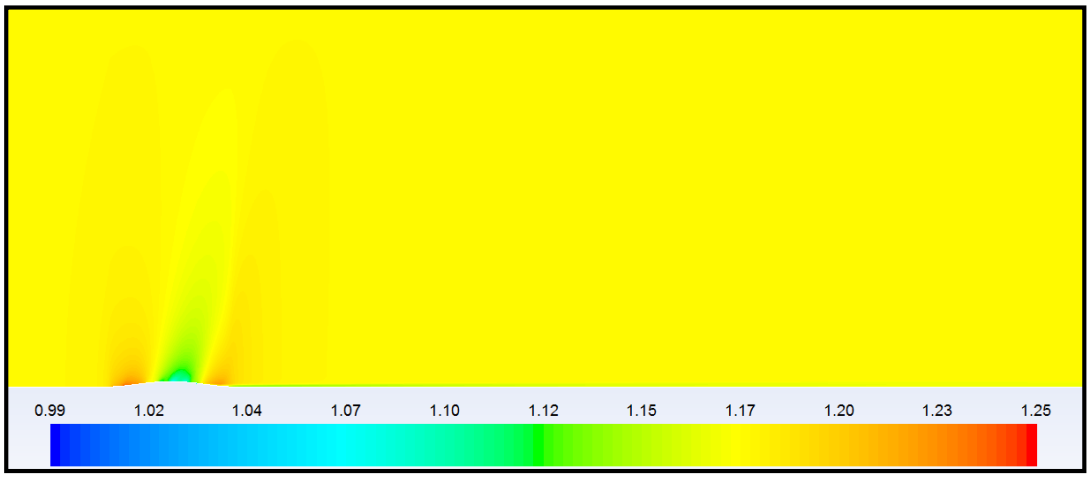

Figure 17–S–H Slender Body Density Contours at Mach=1 [kg/m^3]

The wave drag coefficient variation between Mach 1 and Mach 2 is shown in Figure 18. It is seen that it has peak at Mach 1 as expected. In addition, total drag coefficient increases to values 2 to 3 times greater than the values in the subsonic region.

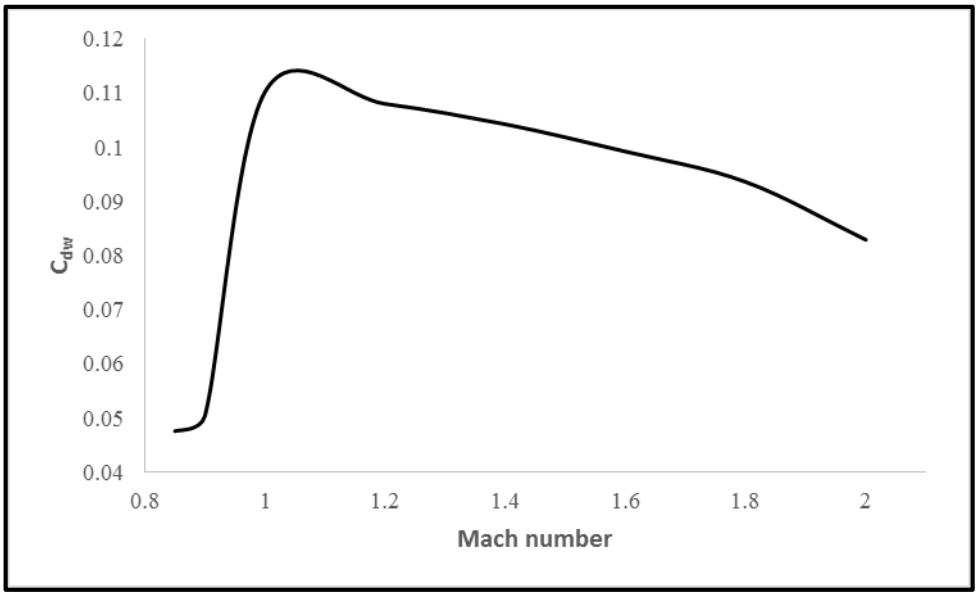

Figure 18–Wave Drag Coefficient Variation with Mach Number

Figure 19 shows the zero–lift drag coefficient increment variation. Drag coefficient at Mach=0.85 is the starting region of shock formation taken as base to observe the change with Mach number. It is observed that drag coefficient of the S–H slender body increases up to Mach=1 and decreases 50% approaching to Mach=2.

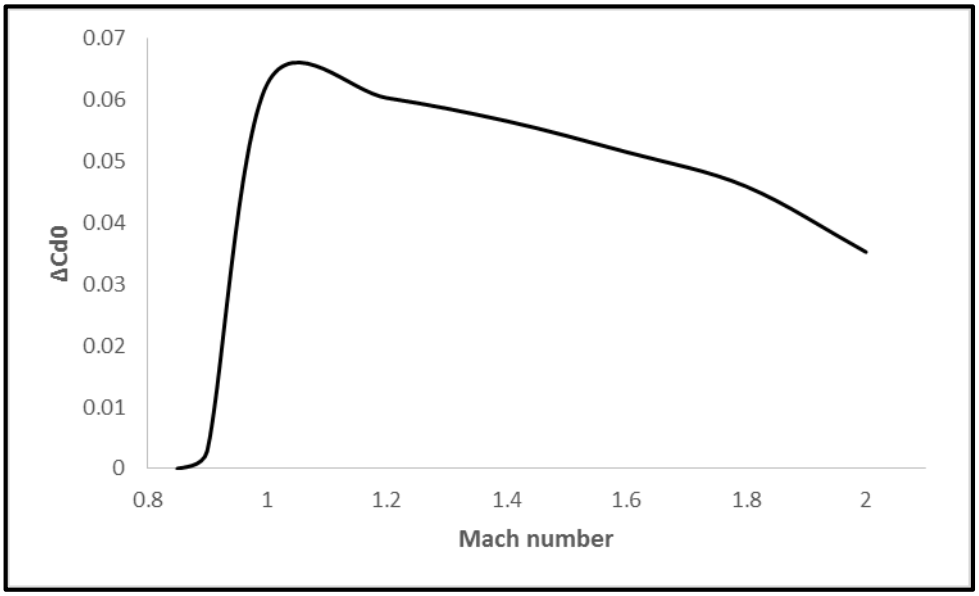

Figure 19–Zero–Lift Drag Coefficient Increment Variation

Table 2 shows the supersonic drag force and wave drag coefficient variation with Mach number. It is observed that drag coefficient increases as Mach increases, and a peak is observed at Mach 1. Then, for supersonic speeds, it decreases with increasing Mach number. However, drag force increases continuously as this is proportional to the square of the velocity.

Table 2–Wave Drag Coefficient and Total Drag Force Variation

Mach number	**Drag Force [N]**	C_{D_w}
2.00	132000	0.083
1.80	120854	0.093
1.60	101000	0.099
1.40	81380	0.104
1.20	63584	0.108
1.00	46340	0.110
0.90	16279	0.051
0.85	13700	0.048

The comparison of the present results and Rallabhandi's results is given in Table 3. Due to the disadvantages of linearized supersonic theory explained above the drag force is calculated less than the actual. Change in flow behavior over the aircraft surface due to shock formation results in an underestimation of the pressure over surface.

Table 3–Comparison of the Results

Mach	**Rallabhandi's result** C_{D_w} [8]	**Present** C_{D_w}
1.00	0.089	0.110
2.00	0.081	0.083

4.1.2 F–16 Case

Figure 20 shows the mesh volume representation. Mesh volume is prepared according to aerodynamic CFD analysis considerations as upstream and far stream are created as

10 times of aircraft length and 5 times for the upper and lower boundaries of mesh volume. k-ε turbulence model is used for flow simulation.

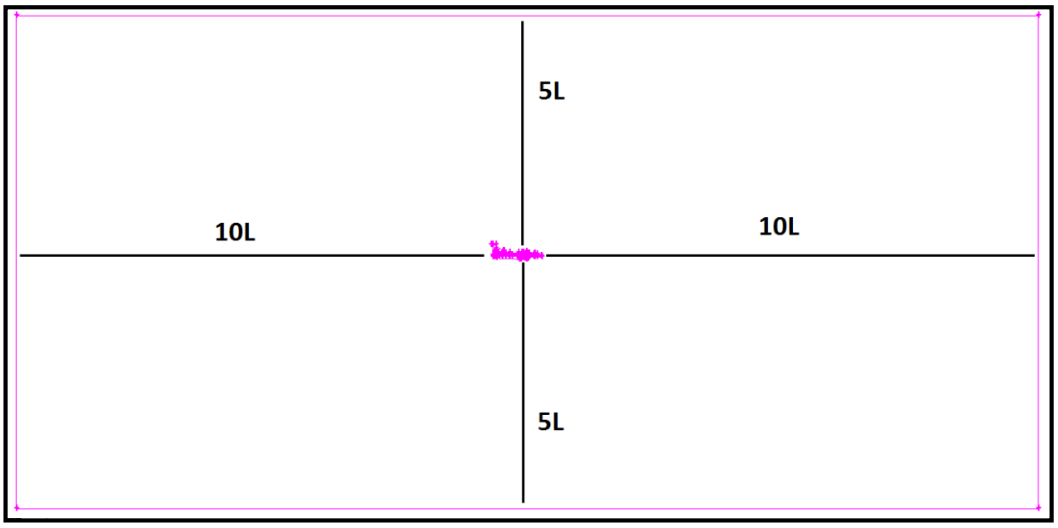

Figure 20–Mesh Volume Representation

Half of the whole configuration is solved for the purpose of efficient use of CPU, since aircraft is symmetric with respect to the longitudinal axis. 6.7 million elements are created for the half aircraft. Figure 21 presents the mesh elements on aircraft surface and symmetry plane. Inviscid drag force is necessary in order to obtain the wave drag force from CFD analysis. Thus, inviscid force observed from CFD simulation is inserted into the wave drag coefficient calculation. (Wave drag is assumed 90% of the inviscid drag.)

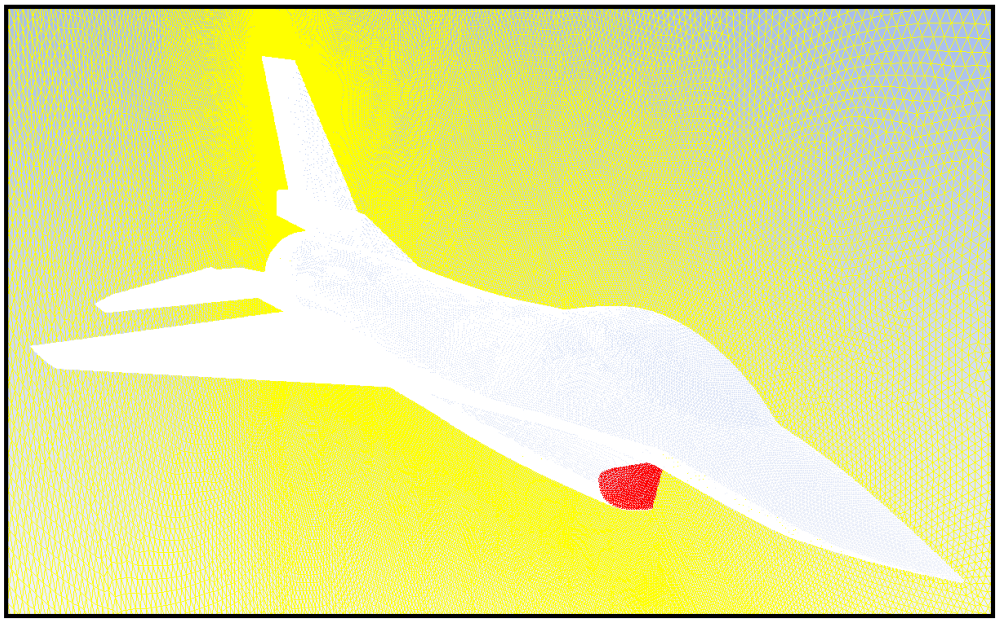

Figure 21–Mesh Presentation

CFD simulation results of the present study is compared with Rallabhandi et al's result [8]. CFD analysis of F 16 is completed at Mach=2 for comparison of the results which are shown in Table 4. It can be seen that 5.7% difference between the wave drag coefficients predictions exist.

Table 4–Comparison of the Results

Mach	**Rallabhandi's result** C_{D_w} [8]	**Present study** C_{D_w}
2.00	0.0357	0.0330

Figures 22,23, and 24 present the temperature, static pressure and Mach number contours of F 16 at Mach=2. It is observed that more than one shock and expansion wave occurs on the aircraft geometry which directly relates the wave drag force. To observe better, same types of contours are taken on the symmetry plane. Figures 25, 26, 27 and 28 show the temperature, static pressure and Mach contours on the symmetry plane.

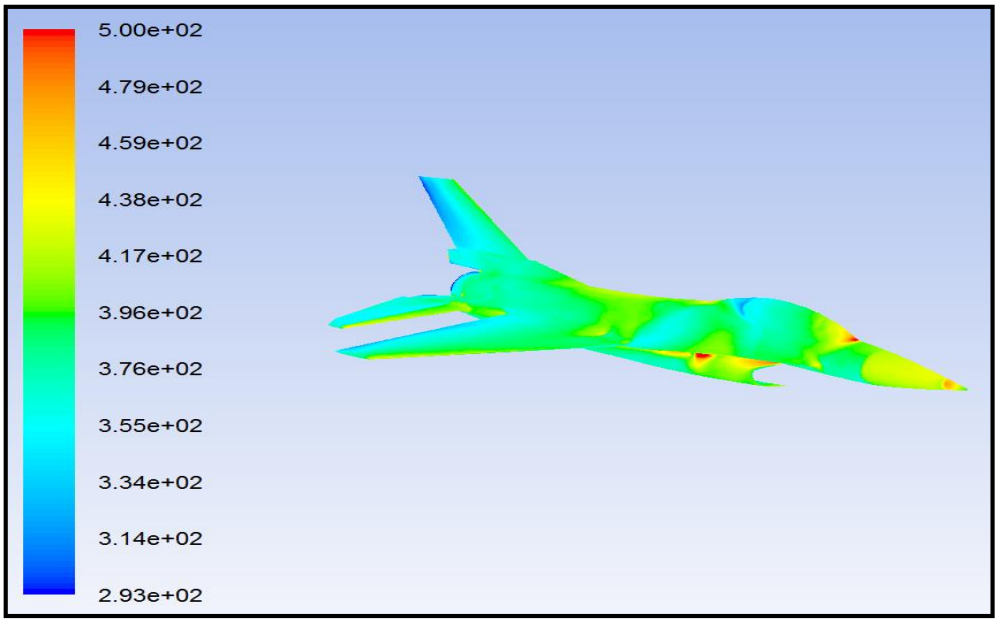

Figure 22–Contours of Temperature [K]

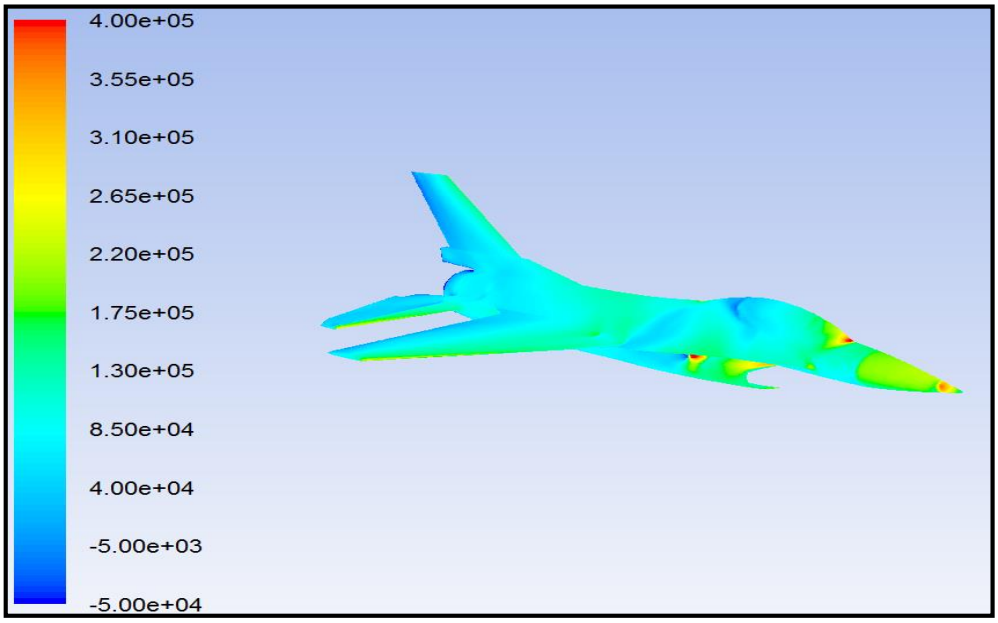

Figure 23–Contours of Static Pressure [Pa]

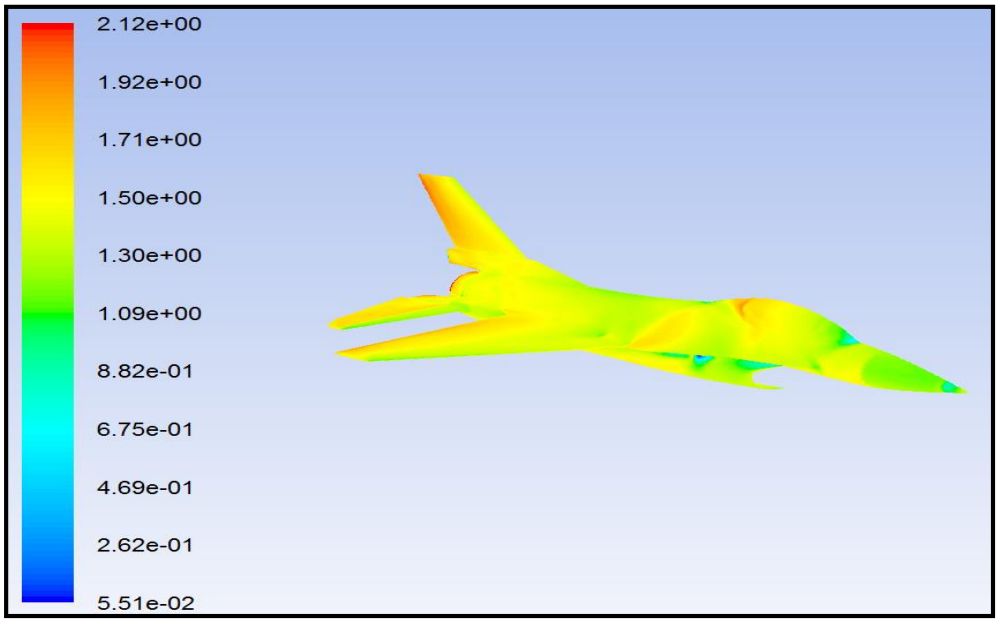

Figure 24–Contours of Mach Number

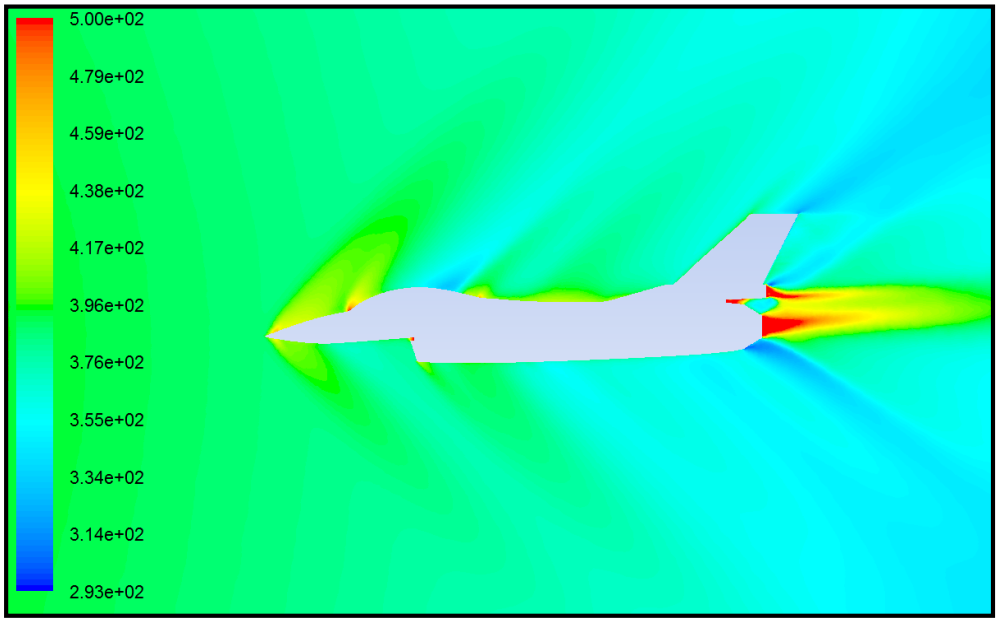

Figure 25–Contours of Static Temperature on the Symmetry Plane [K]

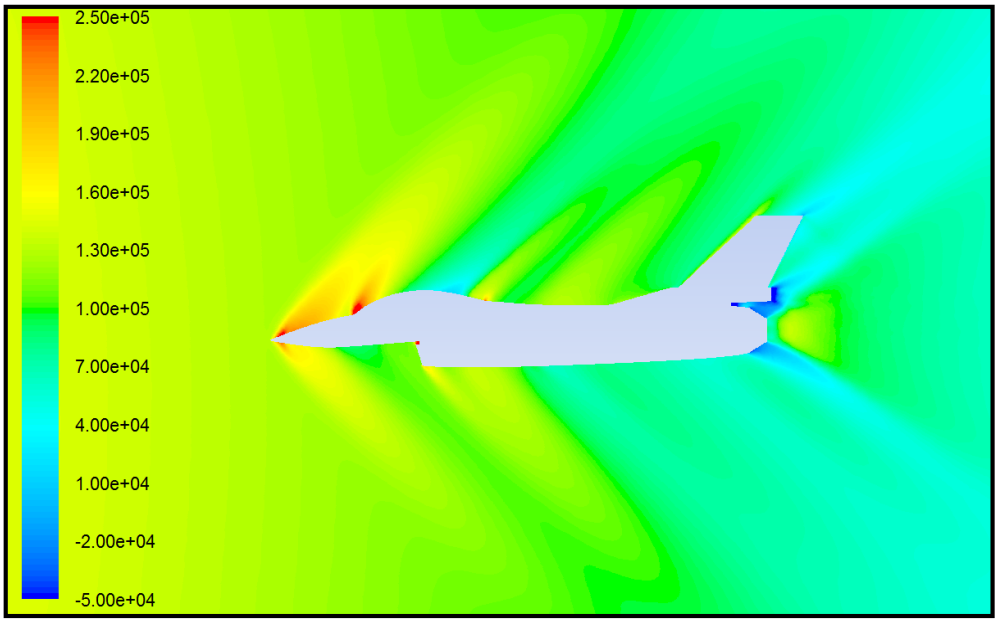

Figure 26–Contours of Static Pressure on the Symmetry Plane [Pa]

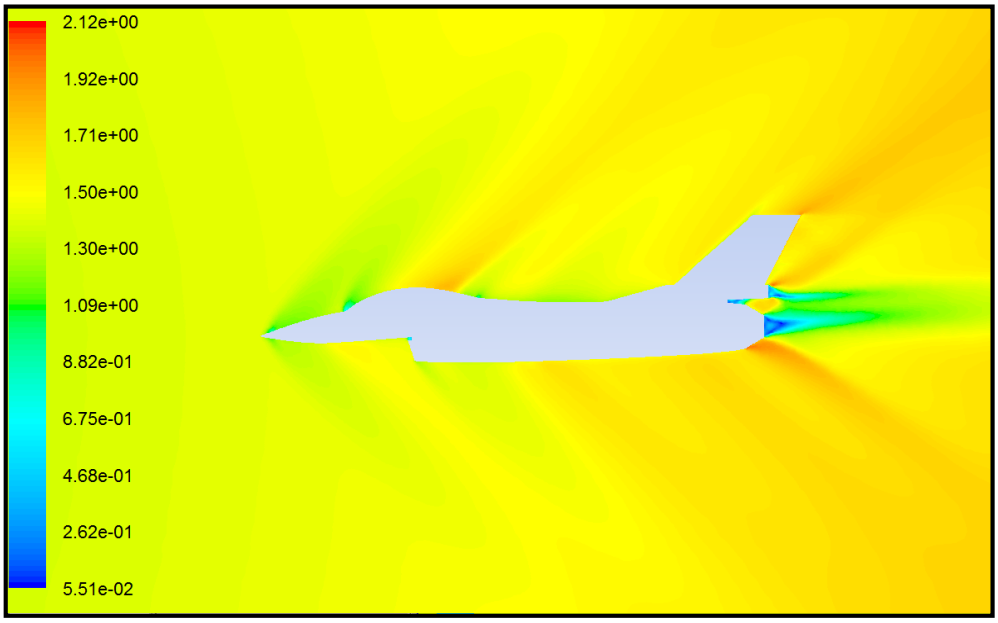

Figure 27–Contours of Mach number on the Symmetry Plane

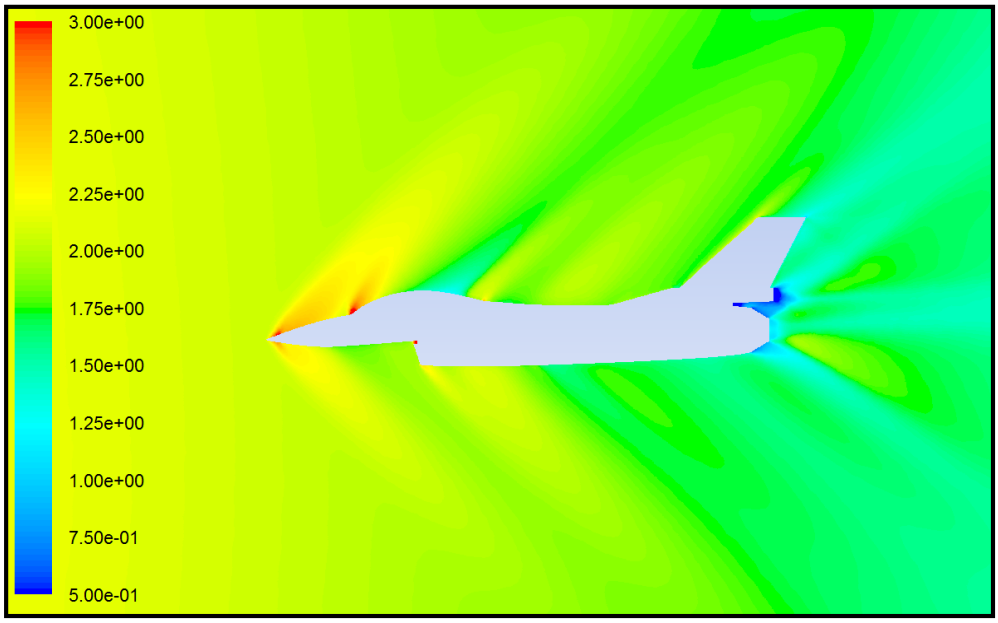

Figure 28–Contours of Density on the Symmetry Plane [kg/m^3]

The validation of the wave drag coefficient results of the F-16 is more challenging. Mesh dependency of the simulation, accurate computational fluid dynamics simulation modelling, and the second derivative of cross sectional area distribution are the parameters that could alter the results. Unlike conceptual designs, F-16 has discontinuities in area distribution; thus, the stability of number of cross sections becomes vital when compared to Sears–Haack slender body. (S–H slender body has continuous first derivative of cross sectional area distribution; thereby, sufficient number of sections could yield accurate results)

4.2 Validation of the Solver

The stability of the method was investigated by Çıtak and Özgen in [21]. Three analytical geometries, representative fighter aircraft geometry and the F-16 geometry were examined in order to bring out stability and accuracy of the program. Figures 29, 30 and 31 present the analytical geometries, Figure 32 presents the representative fighter aircraft geometry and Figure 33 presents the intercepted area distribution of F–16 for Mach 2.

4.2.1 Sears-Haack Slender Body

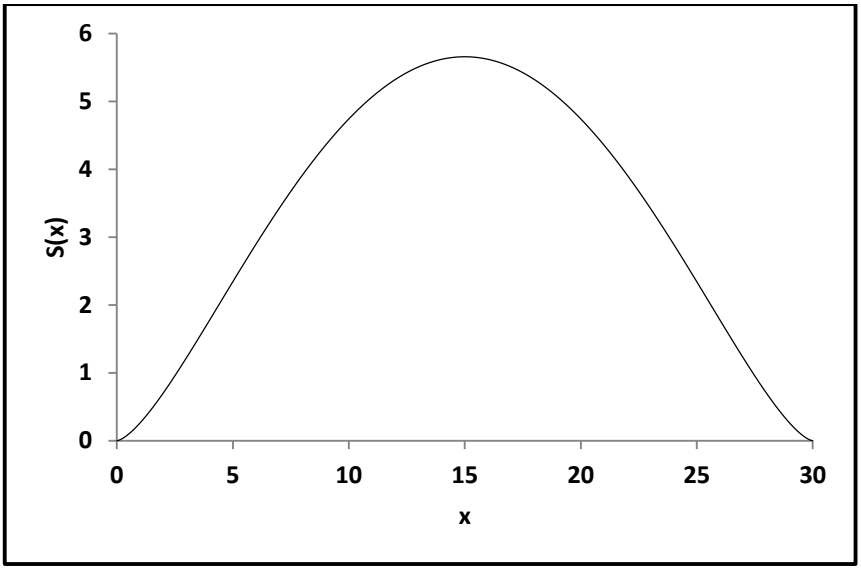

Figure 29-Area Distribution of Sears-Haack Slender Body [21]

Figure 29 presents the Sears-Haack slender body with a volume of 100, and length of 30. Area distribution of the S-H body is given by:

$$S(\theta) = \frac{4V}{\pi l}\left(\sin(\theta) - \frac{1}{3}\sin(3\theta)\right). \tag{3.73}$$

Wave drag force and coefficient of the Sears-Haack slender body can be calculated analytically. Equations (3.75) and (3.76) define these as:

$$D_w = \frac{64V^2}{\pi l^4}\rho U^2, \tag{3.74}$$

$$C_{D_w} = \frac{24V}{l^3}, \tag{3.75}$$

where V is the volume, l is the length, ρ is the freestream density, and U is the freestream velocity. Wave drag coefficient results of S-H slender body are shown in Table 5. As can be seen,the present method agress with the analytical value with an error of less than 10%. (99 points are used to create the geometry.)

Table 5 - Wave Drag Coefficient Results of Sears-Haack Slender Body

Present Study	**Analytic Result**	**Difference (%)**
0.0813	0.0888	-8.4

4.2.2 Von-Karman Ogive

Figure 30 shows the area distribution of Von-Karman Ogive with an area of 30, and length of 10. Area distribution of the body is defined as:

$$S = \frac{S(l)}{\pi}\left(\pi - \theta - \frac{1}{2}\sin(2\theta)\right), \tag{3.76}$$

where *S(l)* is the maximum cross-sectional area (corresponds to $x=l$). Analytical formulas of the wave drag coefficient and force are written in as:

$$D_w = \frac{2\rho U^2}{\pi}\frac{\mathrm{S}(l)^2}{l^2}, \tag{3.77}$$

$$C_{D_w} = \frac{4}{\pi}\frac{S(l)}{l^2}. \tag{3.78}$$

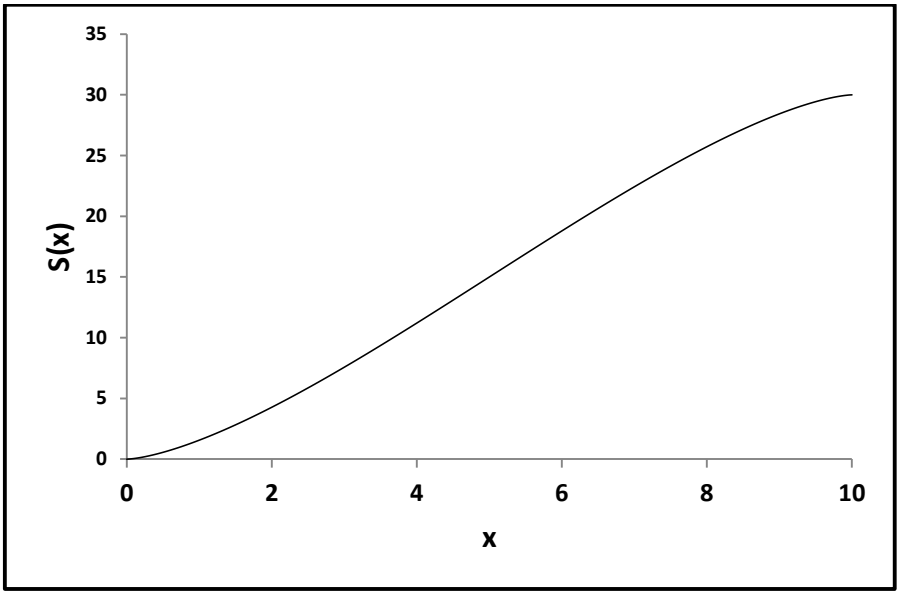

Figure 30-Area Distribution of Von-Karman Ogive [21]

Wave drag coefficients results of Von-Karman Ogive are presented in Table 6 (99 points are used to create the geometry.)

Table 6-Wave Drag Coefficient Results of Von-Karman Ogive

Present Study	Analytic Result	Difference (%)
0.3528	0.3820	-7.6

4.2.3 Cahn and Olstad Geometries

Figure 31 displays the Cahn and Olstad geometries with four different configurations. Results of these configurations are obtained both analytically and numerically.

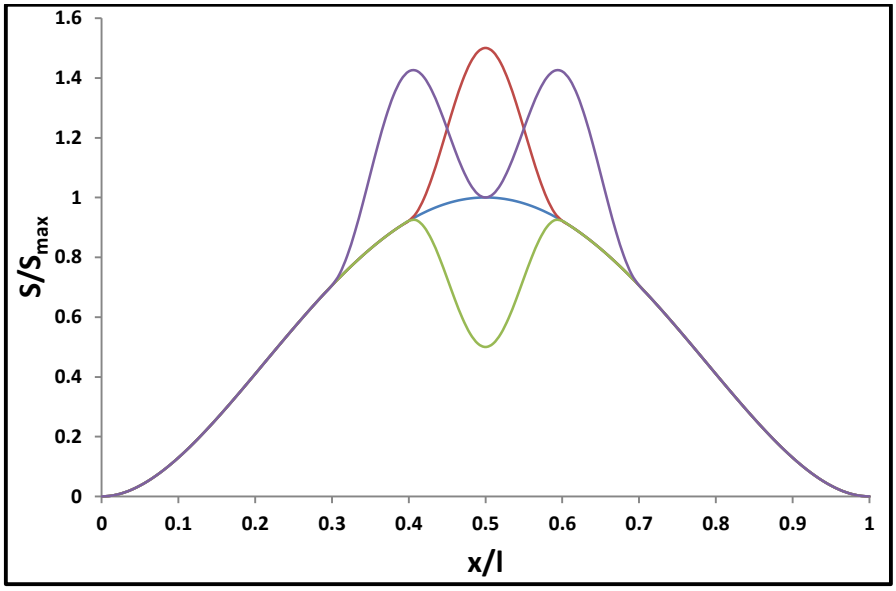

Figure 31-Area Distribution of Cahn-Olstad Geometries [22]

The area distribution of Cahn-Olstad Geometries are created by using 1000 cross-sections. Thus, sensitivity of the number of cross-sections is not considered since the analytical function is used. Table 7 presents the wave drag coefficient results of Cahn-Olstad geometries. As can be seen, the agreement of the results are very good, less than 3% for all cases considered.

Table 7-Wave Drag Coefficient Results of Cahn-Olstad Geometries

Geometry	**Present Study $(R/l)^2$**	**Analytic Result $(R/l)^2$**	**Error (%)**	**Numeric Result $(R/l)^2$**	**Error (%)**
Config. 1	42.66	42.52	+0.32	42.65	+0.02
Config. 2	329.67	329.23	+0.13	325.81	+1.19
Config. 3	304.34	303.25	+0.36	296.84	+2.53
Config. 4	643.43	642.43	+0.16	645.94	-0.39

4.2.4 Representative Fighter Aircraft Geometry

Figure 32 shows the area distribution of representative aircraft geometry. This geometry is typical of 1970s design. Area distribution of the geometry is given by

$$S(x) = 400x^6 - 1176x^5 + 1257x^4 - 588x^3 + 108x^2. \quad (3.79)$$

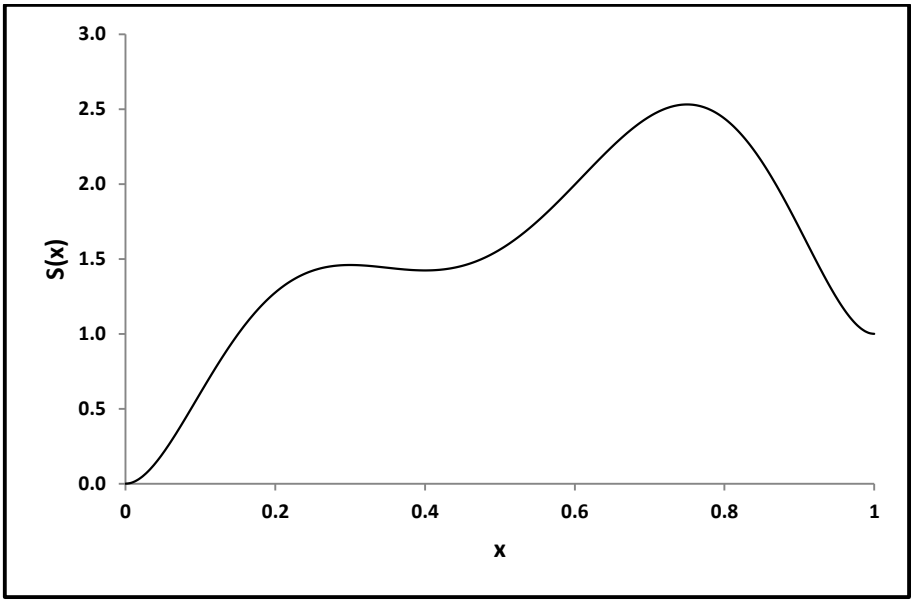

Figure 32-Area Distribution of Representative Fighter Aircraft [22]

Table 8 presents the wave drag results of representative fighter aircraft geometry. As can be seen, the agreement of current results with numerical and analytical results in the literature are very good, with an error of less than 1%.

Table 8-Wave Drag Results of Representative Fighter Aircraft Geometry

Present Study	Analytic Result	Difference (%)	Numeric Result	Difference (%)
126.9871	127.9606	-0.76	127.6451	-0.51

4.2.5 F-16 Geometry

Figure 33 shows the intercepted area distribution of F-16 for Mach=2.

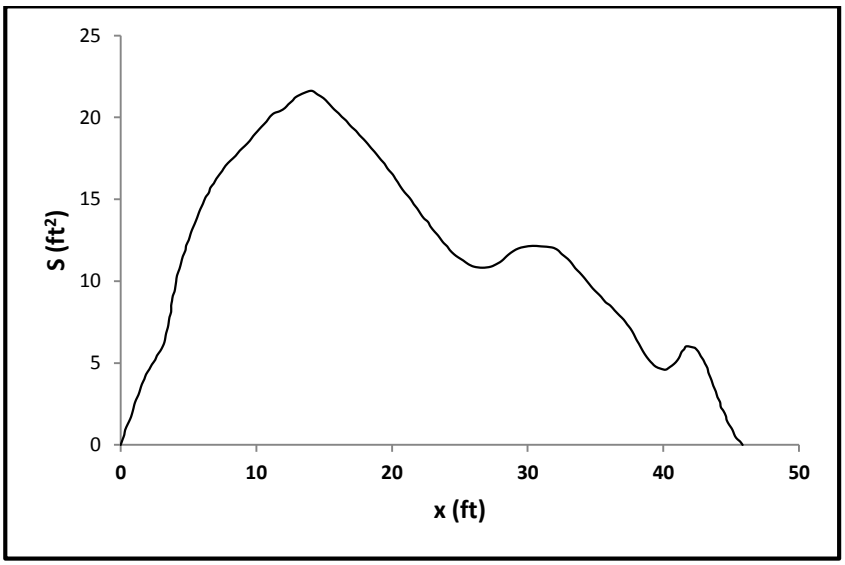

Figure 33-Intercepted Area Distribution of F-16 for Mach 2 [8]

Wave drag coefficient results of F-16 for Mach 2 are presented in Table 9. Here, the error is higher due to the reasons explained below.

Table 9-Wave Drag Coefficient Results of F-16 for Mach=2

Present Study	**Numeric Result**	**Difference (%)**
0.0373	0.0357	+4.5

Increase in number of points for analytical geometries improves the accuracy of the method continuously. On the other hand, this approach for non–analytical geometries does not yield the same result due to the fact that non–analytical geometries could not be represented by functions having continuous first derivative. The effect of peaks and bases between measurement points could not be taken into account during wave drag coefficient calculation which yields incorrect values. Figure 34 shows the sensitivity analysis for the number of cross sections of non-analytical geometry (F-16). It can be

seen that change of wave drag coefficient with respect to number of cross section is unpredictable. Therefore, limit for change of the wave drag coefficient must be placed properly in order to decide the optimal number of cross sections if non-analytical approach is employed.

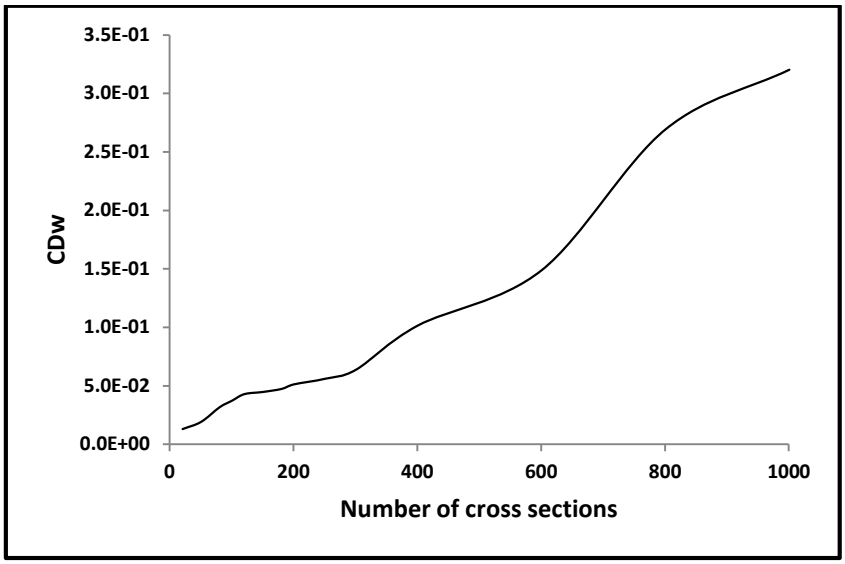

Figure 34-Sensitivity Analysis for Number of Cross Sections

Furthermore, linearized theory requires that the first derivatives of cross sectional area distributions at nose and end are equal to zero as mentioned before. Thus, it is recommended for aircraft being designed for supersonic speeds to be in accordance with this requirement to minimize the wave drag coefficient.

4.3 Test Case Descriptions and Optimization Results

Five different test cases are introduced in order to prove that the solver has the ability to converge to the optimal shape. The methodology of the case matrix is to obtain the success of the numerical method for each aerodynamic configuration. Airfoil shape, chord length, span, sweep and dihedral angle of the aircraft are shown for each configuration [19]. Lifting and control surfaces are not modified during optimization in order not to alter aerodynamic characteristics of the aircraft. In addition, theoretical validation is the most important argument. Despite the fact that optimal shape of the conceptual aircraft design is not the best choice for manufacturability, theoretical

aspect of these cases brings out the optimal shape with respect to the objective function. (*Feet and degrees are used for lengths and angles units for all test cases.*)

4.3.1 Configuration 1

Table 10 and 11 show the specifications of configuration 1, which is wing-body combination. Figure 35 presents the initial form of configuration 1.

Table 10-Specification of Configuration 1-Wing

	Wing
airfoil	NACA 63A304
chord	2-24
span	18.55
sweep	35.7
dihedral	0

Table 11-Specification of Configuration 1-Fuselage

	Fuselage
length	72.75
volume	713.7
maximum diameter	4.00

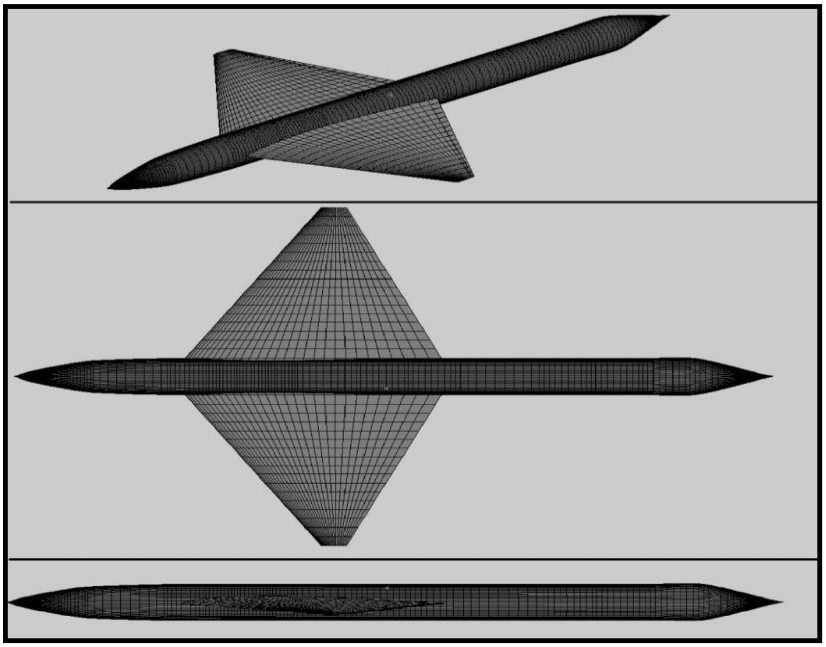

Figure 35–Initial Form of Configuration 1

Figure 36 presents the optimal form of the configuration 1.

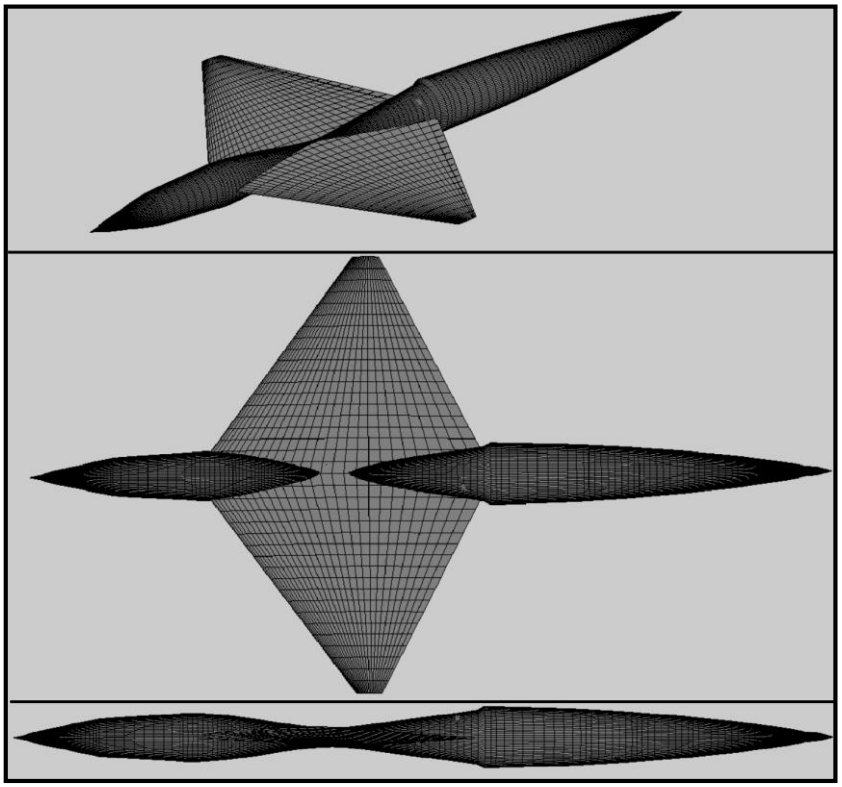

Figure 36-Optimal Form of Configuration 1

Figure 37 presents the optimal and the initial fuselage area distribution.

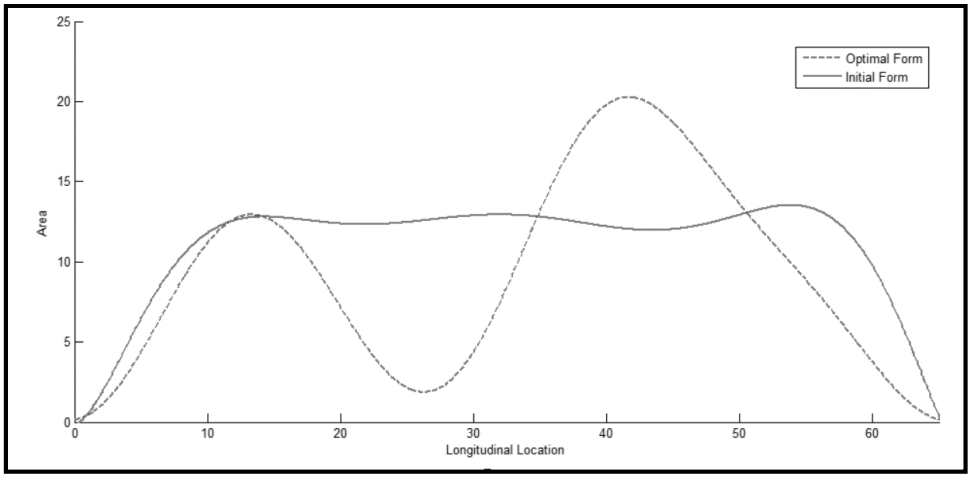

Figure 37-Comparison of Initial and Optimal Fuselage Area Distribution (Configuration 1)

As can be seen, in order to smoothen the area distribution, thereby reducing the wave drag, the locations the fuselage thinned down where the wing cross-section increases the cross-sectional area distribution. As a result of this, the wave drag of the configuration decreases from 0.1053 to 0.0787. However, such a geometry may not the practical as it will prevent engine and system installment very difficult if not impossible.

4.3.2 Configuration 2

Table 12, and 13 show the specifications of configuration 2. Figure 38 presents the initial form of configuration 2.

Table 12-Specification of Configuration 2-Tail

	Tail
airfoil	4% BICONVEX
sweep angle	50
dihedral angle	12.3
span	31.7

Table 13-Specification of Configuration 2-Fuselage

	Fuselage
length	72.75
volume	713.7
maximum diameter	4.00

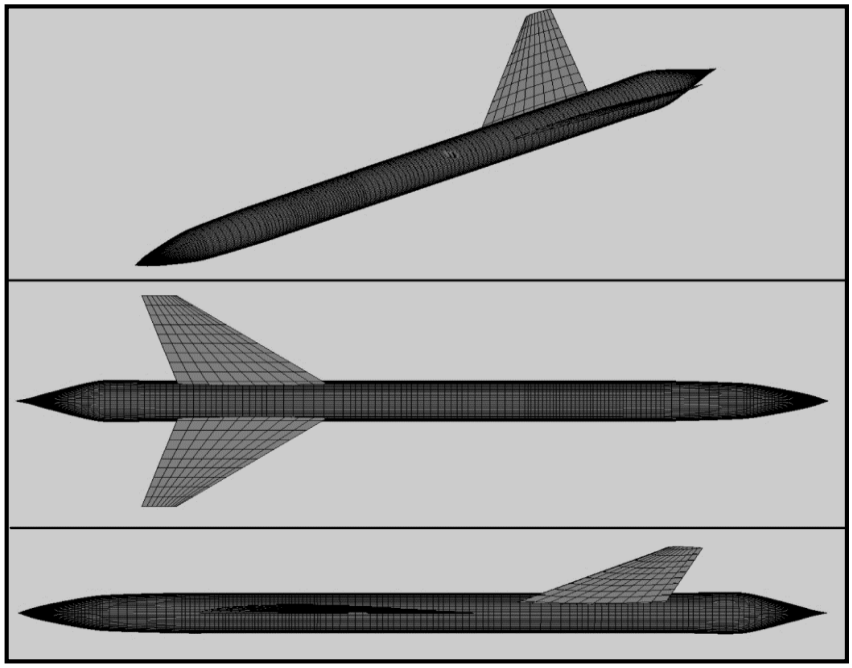

Figure 38–Initial Form of Configuration 2

Figure 39 shows the optimal form of configuration 2.

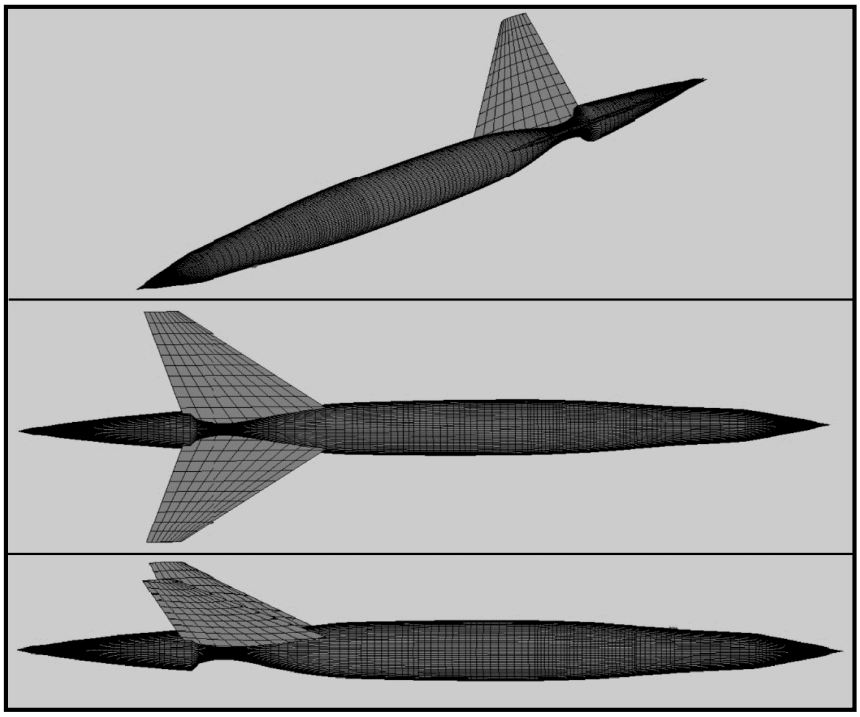

Figure 39–Optimal Form of Configuration 2

Figure 40 shows the optimal and the initial fuselage area distribution.

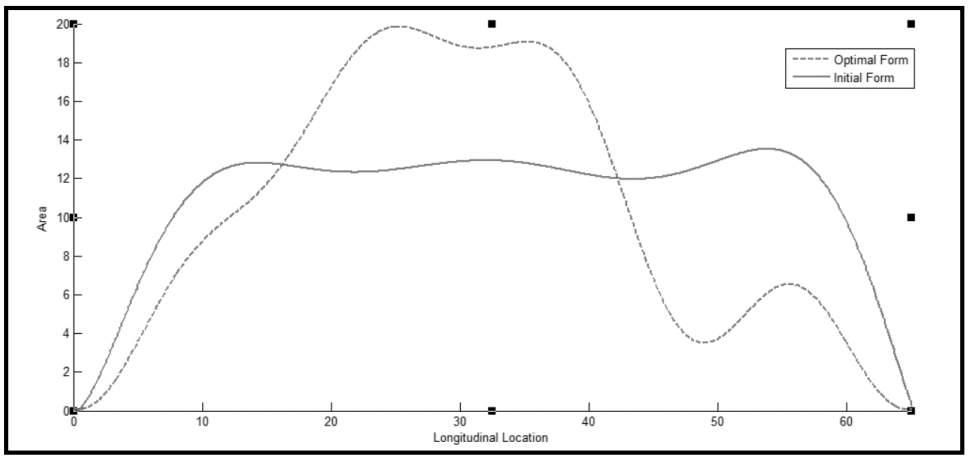

Figure 40-Comparison of Initial and Optimal Fuselage Area Distribution (Configuration 2)

Again, the fuselage has been narrowed down to accommodate the extra area brought in by tail surfaces. Wave drag of the configuration is decreased from 0.0937 to 0.0634.

4.3.3 Configuration 3

Table 14, 15, and 16 show the specifications of configuration 3. This is a combined wing-body-tail configuration and is presented to demonstrate the capabilities of the computational tool for optimizing more than one location on the geometry. Figure 41 presents the initial form of configuration 3.

Table 14-Specification of Configuration 3-Wing

	Wing
airfoil	NACA 63A304
chord	2-24
span	18.55
sweep	35.7
dihedral	0

Table 15-Specification of Configuration 3-Tail

	Tail
area	103.2
sweep	45
dihedral	12.3
airfoil	4% BICONVEX
span	31.7

Table 16-Specification of Configuration 3-Fuselage

	Fuselage
length	72.75
volume	713.7
maximum diameter	4.00

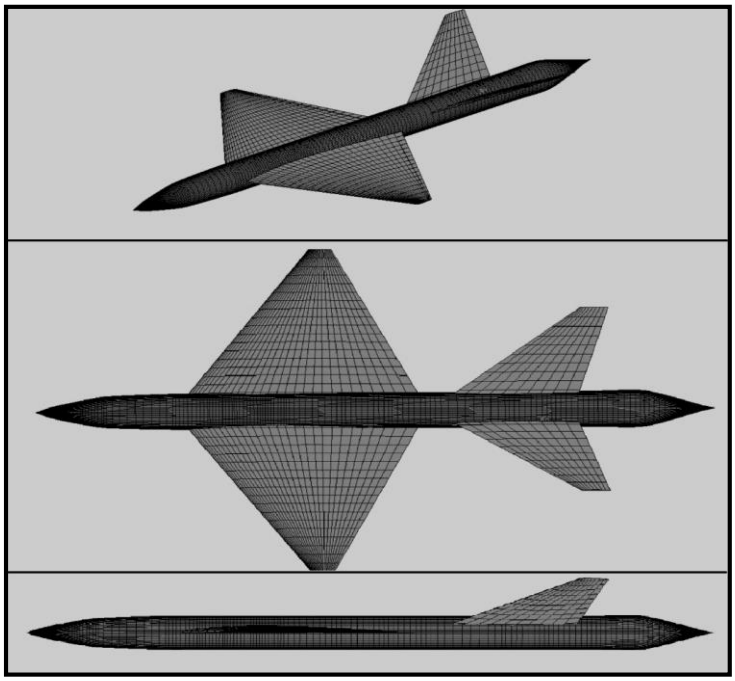

Figure 41–Initial Form of Configuration 3

Figure 42 presents the optimal form of the configuration 3. As expected, the fuselage is narrowed down in order to negate the extra areas brought in by the wing and the tail in order to obtain a smooth area distribution. Wave drag of the configuration is reduced from 0.1349 to 0.0831.

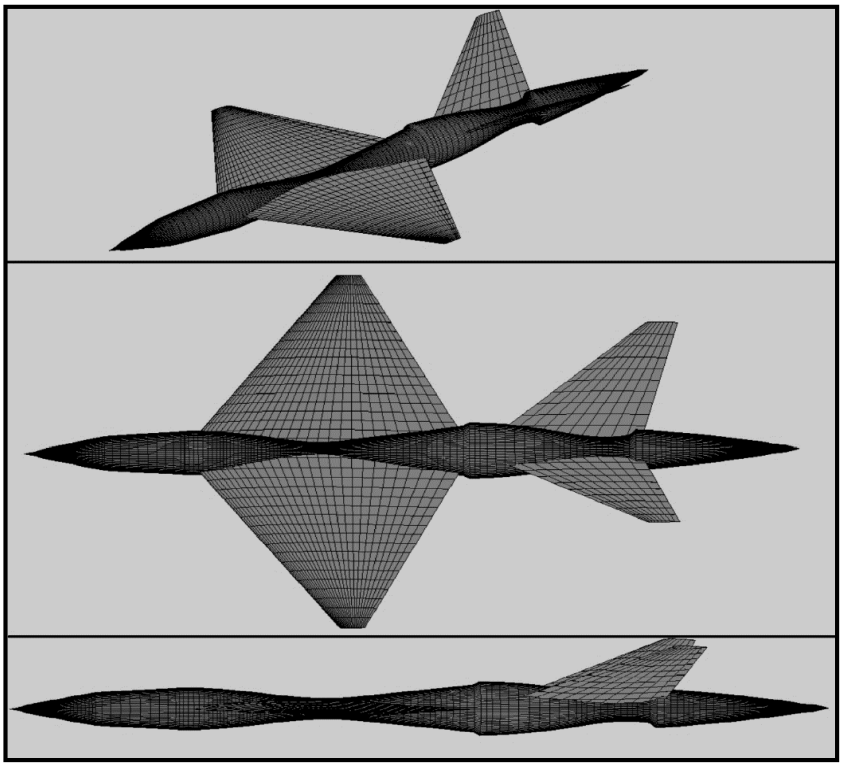

Figure 42–Optimal Form of Configuration 3

Figure 43 presents the optimal and the initial fuselage area distribution.

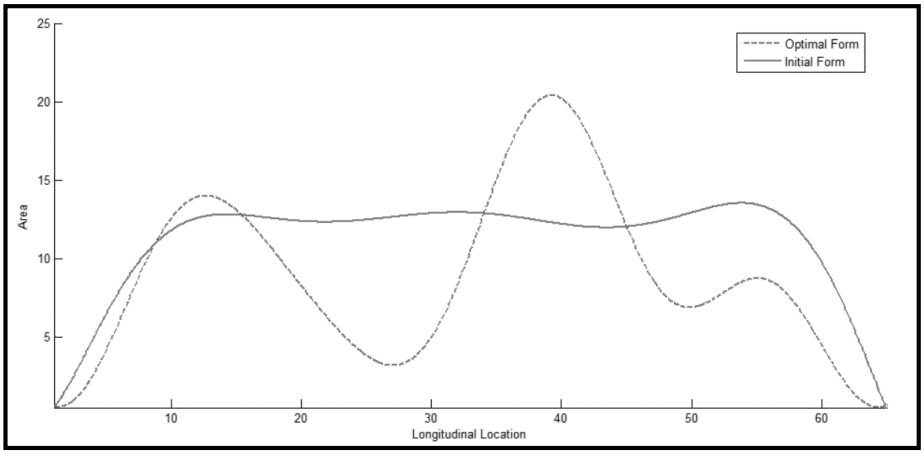

Figure 43-Comparison of Initial and Optimal Fuselage Area Distribution (Configuration 3)

4.3.4 Configuration 4

Table 17, 18, and 19 show the specifications of configuration 4. This is a swept wing configuration where the contribution of the wing tip sections is beyond the wing attachment portion on the fuselage. Figure 44 presents the initial form of configuration 4.

Table 17-Specification of Configuration 4-Wing

	Wing
airfoil	NACA 63A304
chord	2-24
span	18.55
sweep	45
dihedral	0

Table 18-Specification of Configuration 4-Tail

	Tail
area	103.2
sweep	45
dihedral	0
airfoil	4% BICONVEX
span	31.7

Table 19-Specification of Configuration 4-Fuselage

	Fuselage
length	72.75
volume	713.7
maximum diameter	4.00

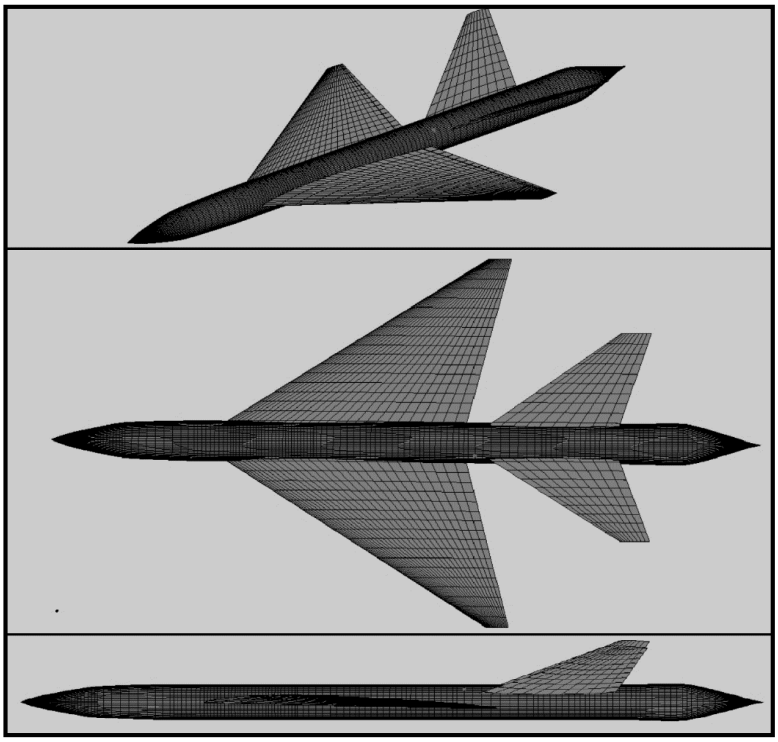

Figure 44–Initial Form of Configuration 4

Figure 45 shows the optimal form of the configuration 4.

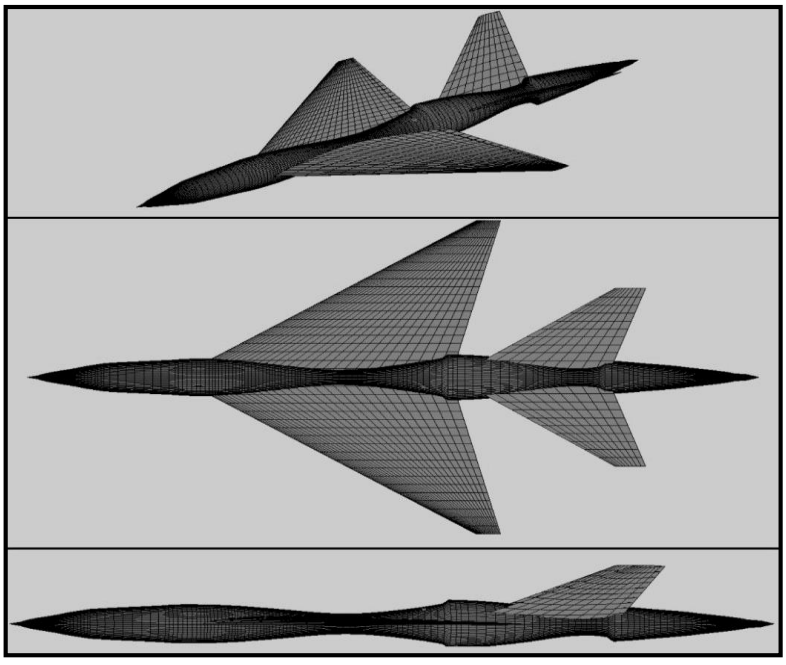

Figure 45–Optimal Form of Configuration 4

Figure 46 shows the optimal and the initial fuselage area distribution.

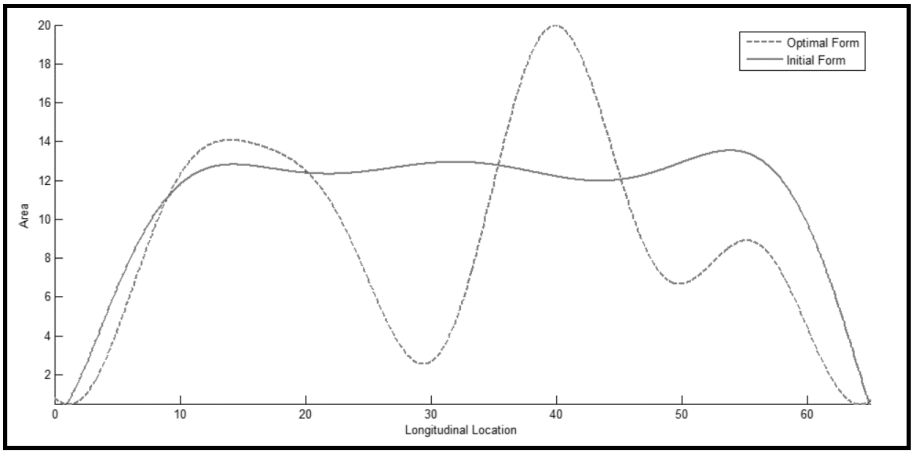

Figure 46-Comparison of Initial and Optimal Fuselage Area Distribution (Configuration 4)

As can be seen, the computational tool can optimize geometries where the area distribution do not necessarily come from the parts of the wing or tail where they are directly attached to the fuselage. Wave drag of the configuration is reduced from 0.1142 to 0.0819.

4.3.5 Configuration 5

Table 20, 21, and 22 show the specifications of configuration 5. Figure 47 presents the initial form of configuration 5. This is a roughly similar configuration to the previous cases, except that wing has negative dihedral.

Table 20-Specification of Configuration 5-Wing

	Wing
airfoil	NACA 63A304
chord	2-24
span	18.55
sweep	45
dihedral	0

Table 21-Specification of Configuration 5-Tail

	Tail
area	103.2
sweep	45
dihedral	12.3
airfoil	4% BICONVEX
span	31.7

Table 22-Specification of Configuration 5-Fuselage

	Fuselage
length	72.75
volume	713.7
maximum diameter	4.00

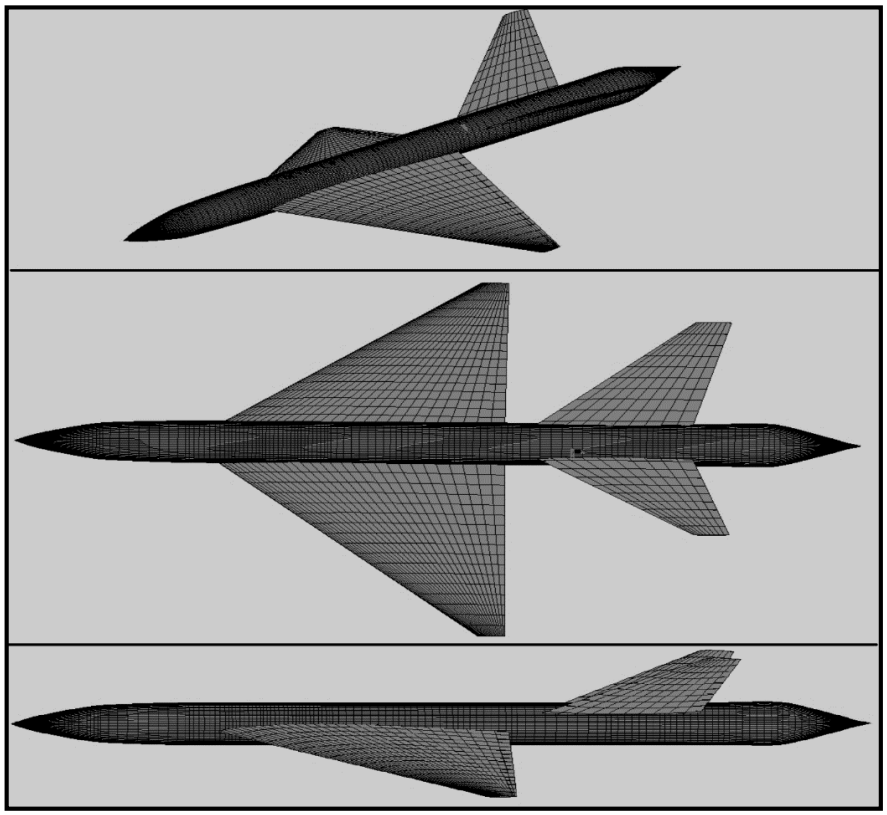

Figure 47–Initial Form of Configuration 5

Figure 48 presents the optimal form of the configuration 5.

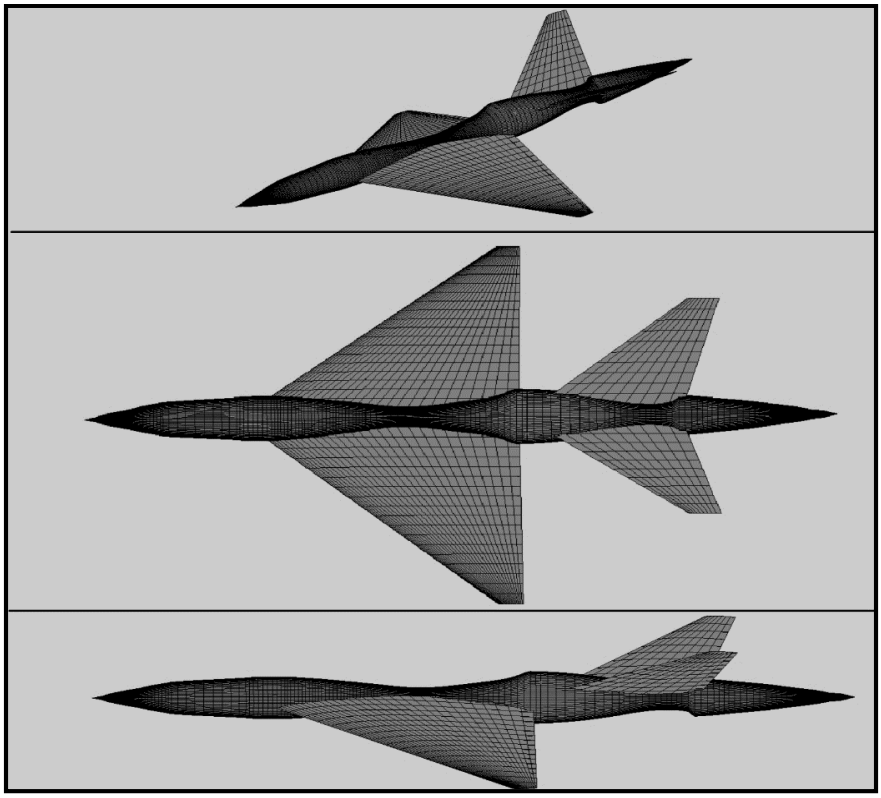

Figure 48–Optimal Form of Configuration 5

Figure 49 presents the optimal and the initial fuselage area distribution.

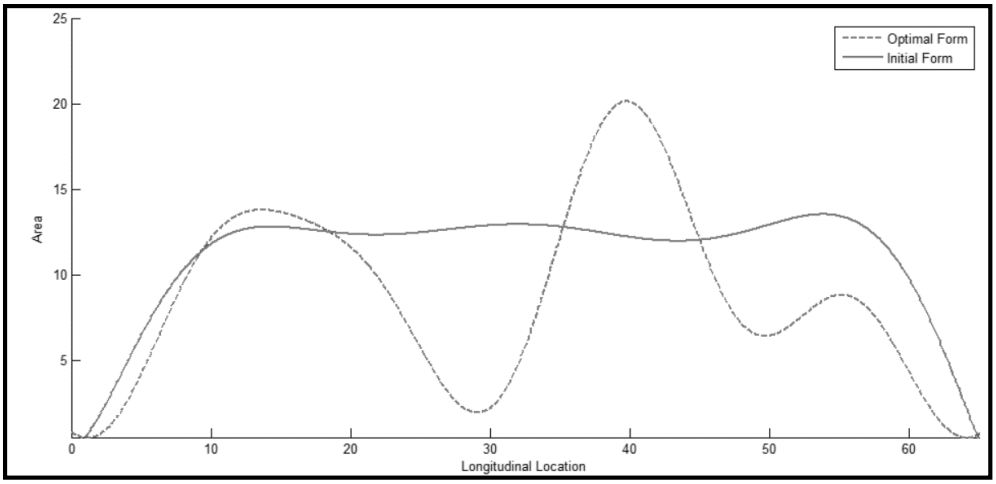

Figure 49-Comparison of Initial and Optimal Fuselage Area Distribution

Table 23 displays the wave drag coefficient results of the original and optimum configurations.

Table 23–Wave Drag Coefficient Results of Configurations

	Initial C_{dw}	**Optimal C_{dw}**	**Reduction (%)**	**Equivalent S-H C_{dw}**
Configuration 1	0.1053	0.0787	25.3	0.0787
Configuration 2	0.0937	0.0634	32.3	0.0633
Configuration 3	0.1349	0.0831	38.4	0.0830
Configuration 4	0.1142	0.0819	28.3	0.0810
Configuration 5	0.1388	0.0831	40.1	0.0830

Table 23 shows the initial and optimal wave drag coefficients. In addition, comparison of optimal results with equivalent S-H values can be obtained table shown above. Figure 50 presents the residual history of the configurations.

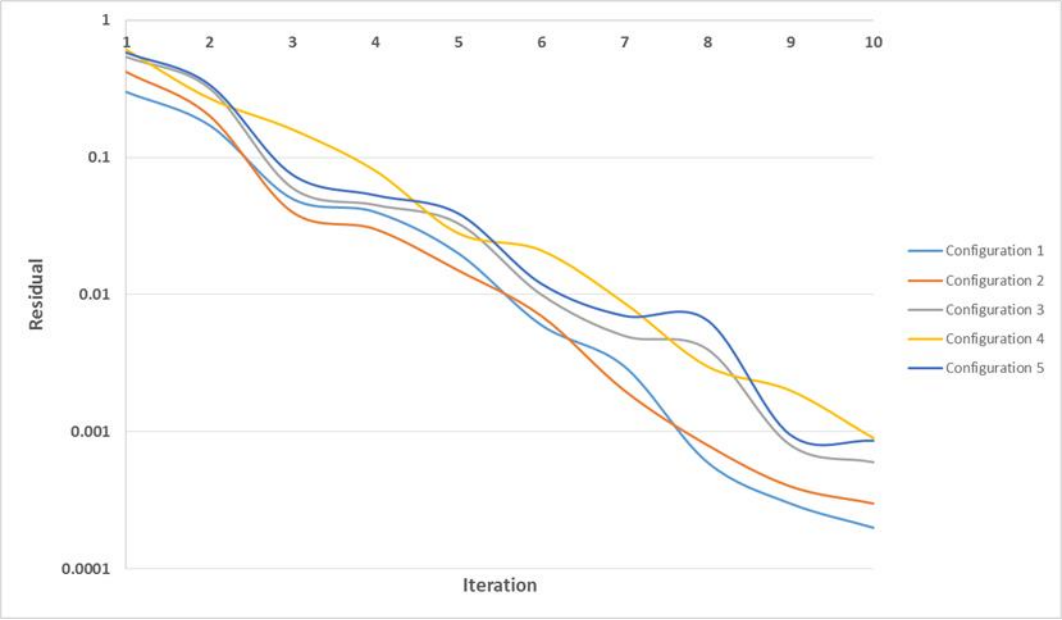

Figure 50–The Residual History of the Configurations

4.4 Discussion about the Optimization Results

The optimal forms of the configurations are presented in this section. Non–lifting components (fuselage) are modified during the optimization loop in order not to change the aerodynamic characteristics of the configurations. In other words, fuselage is reshaped to minimize the wave drag coefficient.

Mach cuts plays an important role on calculating wave drag force and coefficient for an arbitrary shaped aircraft. Equation (3.81) presents the Mach angle which is used for calculating intercepted area distribution without using the Mach cone approach.

$$\mu = \sin^{-1}\left(\frac{1}{Mach}\right). \tag{3.80}$$

The aerodynamic characteristics of an aircraft must remain unchanged during optimization. Therefore, lifting and control surfaces and related cross–sections are excluded from the optimization algorithm. Furthermore, the total volume of the aircraft is calculated by summing all parts including the lifting and control surfaces. In other words, non-lifting surfaces are modified with respect to the objective function. Second, the intercepted cross–sectional area distribution for various Mach number is obtained by neglecting the small changes due to Mach cone method. It can be stated that non-lifting surfaces of high speed aircraft must be as smooth as possible due to avoiding the flow separation and shock formation. For this reason, non–lifting surfaces such as fuselages do not have sharp geometry changes which brings out the intercepted area distribution for various Mach number could be obtained with Mach angle methodology only.

Despite the fact that Mach number seems influential on the optimization process, the optimal cross sectional area distribution is independent from Mach number. Mach number only affects the intercepted area distribution only. Thus, Sears–Haack slender body has the minimum wave drag coefficient for a given volume and length. However, the intercepted area distribution and wave drag coefficient of it change with respect to Mach number. To have the minimum value of wave drag coefficient for an aircraft,

the change of first derivative of cross sectional area distribution of the entire aircraft has to be minimum for a given volume and length. The methodology explained above is commonly used for high subsonic and supersonic aircraft design development. Hepperle [23] utilizes the same method to optimize the supersonic transport aircraft. The configuration of his aircraft design is presented in Figure 51.

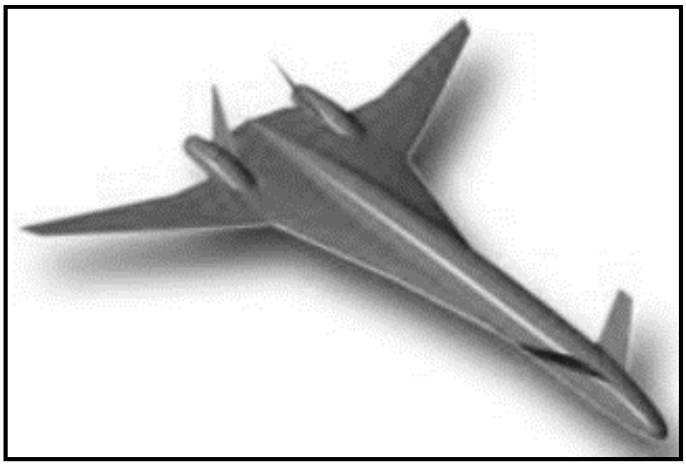

Figure 51–Hepperle's conceptual aircraft [23]

The cross sectional area distribution of Hepperle's conceptual aircraft is presented in Figure 52.

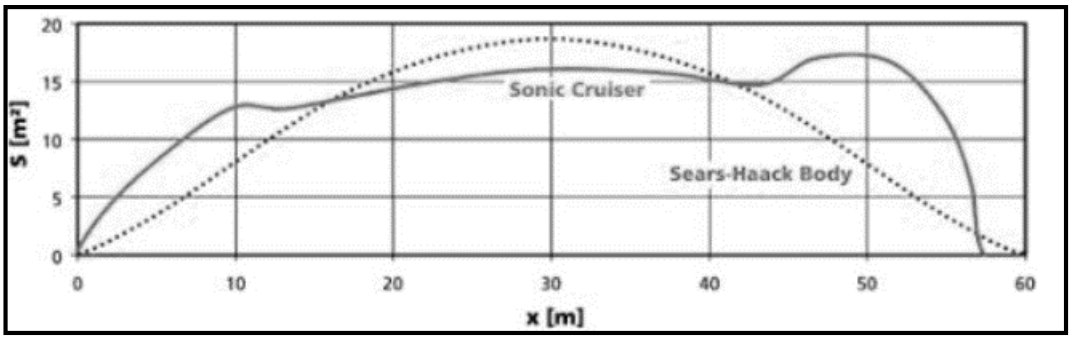

Figure 52–Area Distribution of Hepperle's conceptual aircraft [23]

It is clearly seen that the aircraft does not have the optimum area distribution. Many reasons could explain this. First of all, the aerodynamic efficiency is not the only consideration for aircraft designers. In other words, structural capabilities and stability enhancement are other important applications to be take care of as well as

aerodynamics [23]. Also systems integration like the engine, radar etc. have a strong influence on the geometry, which may often contradict with aerodynamic requirements.

4.5 Fighter Aircraft Geometry with Different Engines

Test cases presented above are analyzed to validate the optimization algorithm. A fighter aircraft geometry is used in order to test the developed computational tool against a more realistic aspect. As can be seen, the optimized geometry reduces the wave drag by 32.9% in average. Also worth mentioning is that the final geometries yield a wave drag coefficient very close to the (Sears-Haack body), underlining the success of the optimization process. The cross-sectional area of air intakes are subtracted from the aircraft geometry in this analysis. Specifications of non–symmetric fuselage, wings and tails for different sections fighter aircraft geometry are presented in Table 24, 25, and 26. Reference area of the wing is 384.07 ft^2.

Table 24-Wing Specifications of Fighter Aircraft

	Section 1	**Section 2**
span	5.13	12.59
tip chord	12.73	4.26
root chord	20.43	12.73
sweep	52	28
dihedral	0	0

Table 25-Vertical Tail Specifications of Fighter Aircraft

	Section 1	**Section 2**
span	1.77	7.36
tip chord	8.05	2.30
root chord	8.05	8.05
sweep	0	50
dihedral	0	60

Table 26-Horizontal Tail Specifications of Fighter Aircraft

	Section 1	**Section 2**
span	2.84	7.53
tip chord	6.99	2.37
root chord	3.76	6.99
sweep	29.52	29.52
dihedral	0	0

Fighter aircraft geometry is investigated with the two different engine configurations; namely, *GE F414* [33] and *GE F110* [34]. Thus, the constraints related to cross–sectional area dimensions are decided with respect to the dimensions of the engines.

4.5.1 Fighter Aircraft Configuration with *GE F110*

Figure 53-55 present the comparison between the optimal and initial form of the three dimensional fighter aircraft configuration with *GE F110* engine.

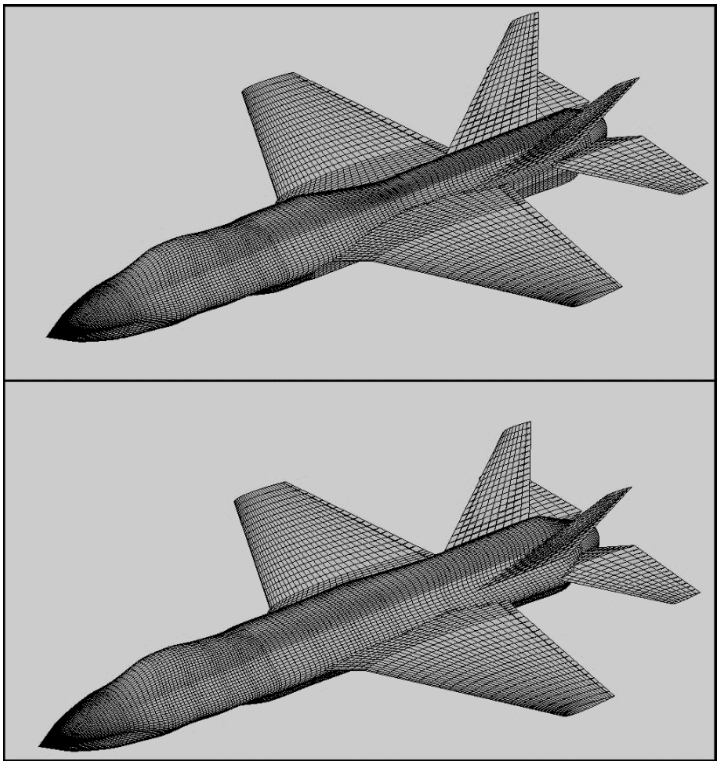

Figure 53-Initial (bottom) and Final (top) Configuration of Fighter Aircraft with GE F110 Engine–Isometric

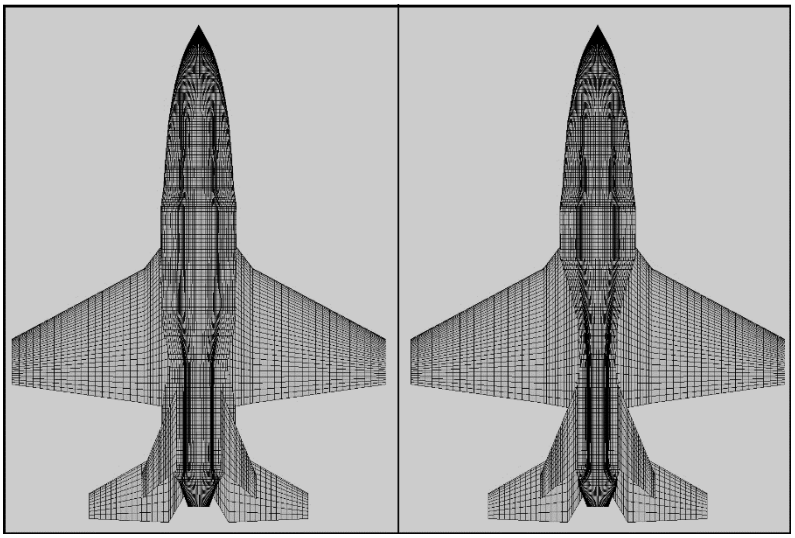

Figure 54-Initial (left) and Final (right) Configuration of Fighter Aircraft with GE F110 Engine–Top

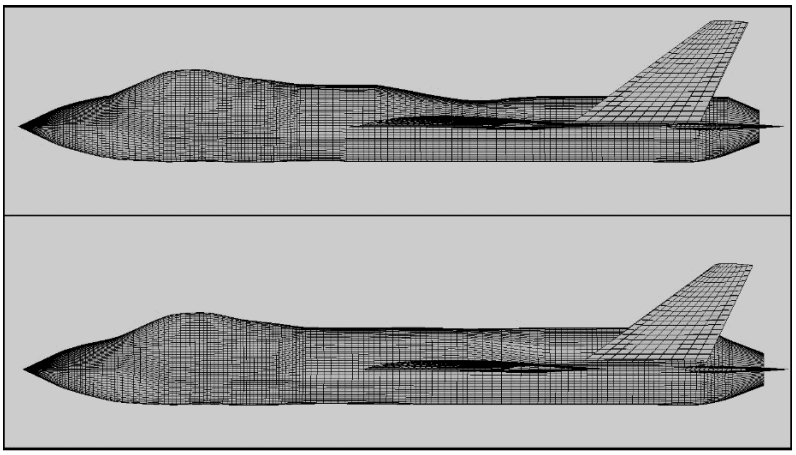

Figure 55-Initial (bottom) and Final (top) Configuration of Fighter Aircraft with GE F110 Engine–Side

The diameter and length of *GE F110* are 3.96 ft and 15.18 ft [33]. According to these dimensions, minimum cross–sectional area for the engine region is 15.4 ft^2 (minimum cross–sectional area is calculated by multiplying the area of the engine with 1.20 to account for cooling space and installation, accessories, etc.). Thus, the locations presenting engine location are fixed to this value and provides a geometric

constraint. Figure 56 presents the initial and the optimal fuselage area distribution of the fighter aircraft geometry with *GE F110* engine.

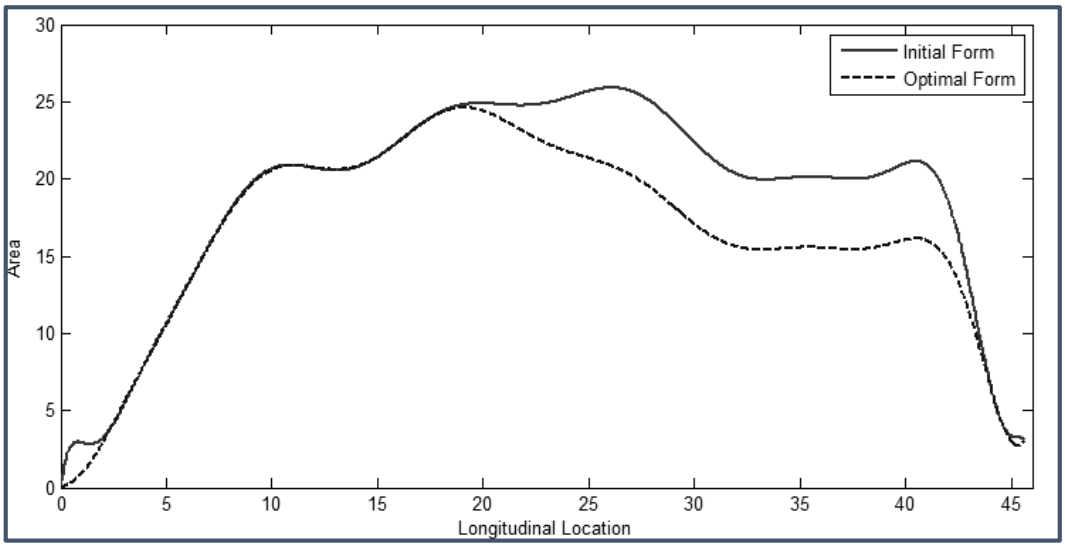

Figure 56-Comparison of Initial and Optimal Fuselage Area Distribution (Fighter Aircraft configuration with GE F110)

The wave drag coefficient of the fighter aircraft is reduced from 0.185 to 0.171 with the constraints explained above.

4.5.2 Fighter Aircraft Configuration with 2x *GE F414*

Figure 57-59 present the comparison between optimal and final form of three dimensional fighter aircraft configuration with 2x*GE F414* engine.

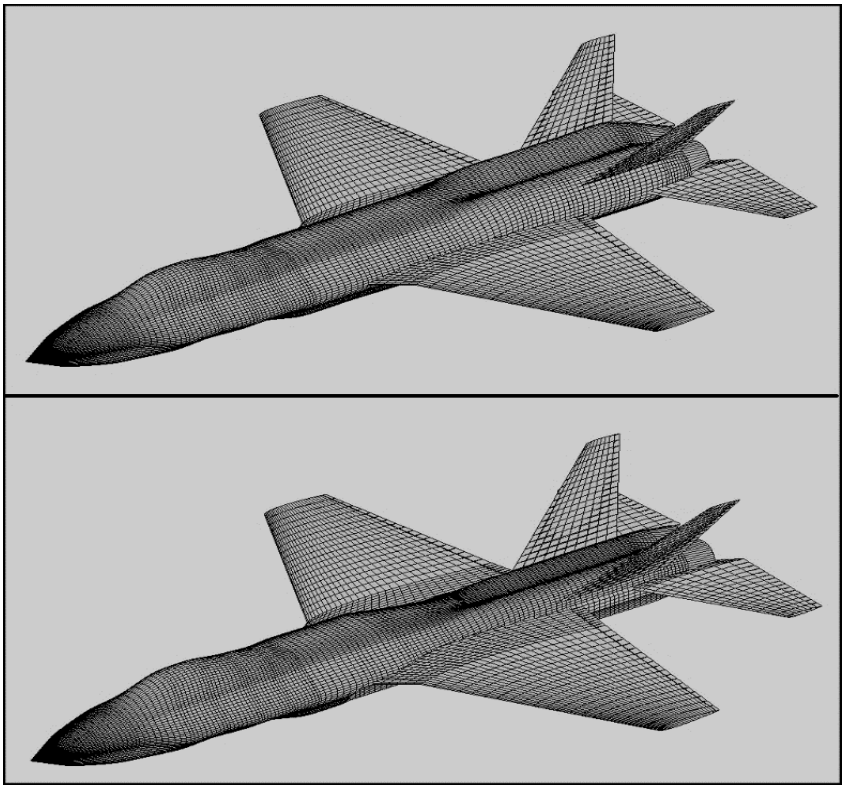

Figure 57-Initial (top) and Final (bottom) Configuration of Fighter Aircraft with 2x GE F414 engines–Isometric

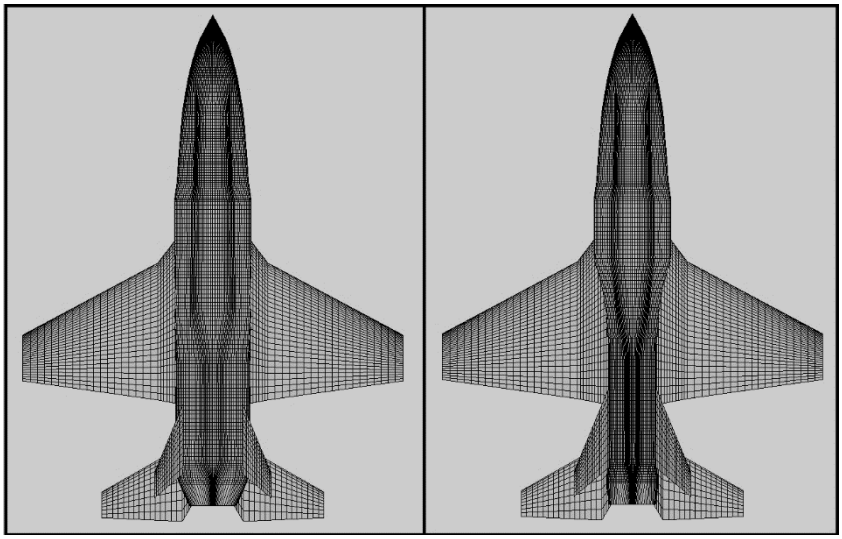

Figure 58-Initial (left) and Final (right) Configuration of Fighter Aircraft with 2x GE F414 Engines–Top

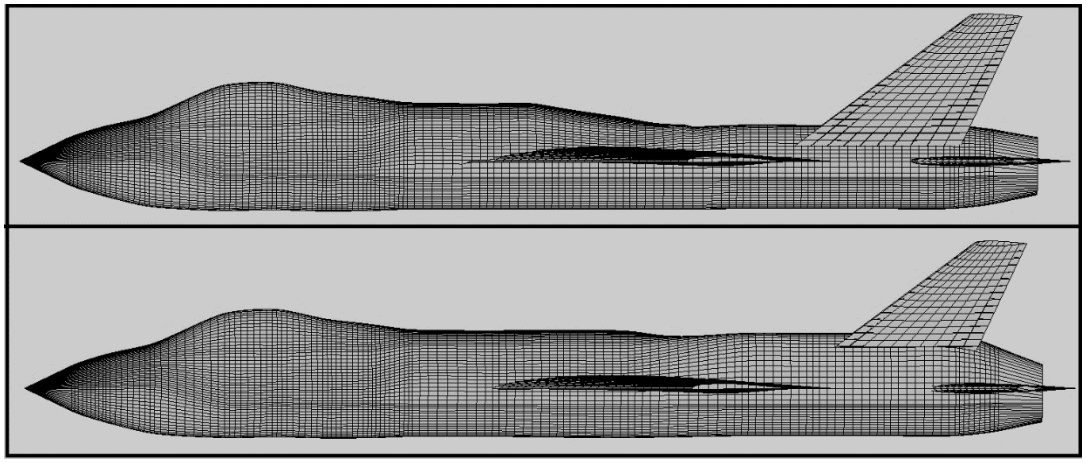

Figure 59-Initial (bottom) and Final (top) Configuration of Fighter Aircraft with GE F414 Engine–Side

The diameter and length of *GE F414* are 2.90 ft and 12.89 ft [33]. According to these dimensions, minimum cross–sectional area for the engine region is 19.12 ft^2 (minimum cross–sectional area is calculated by multiplying the area of the engine with 1.20). Thus, the locations representing engine location are fixed to this value. Figure 60 presents the initial and the optimal fuselage area distribution of the fighter aircraft geometry with *GE F414.*

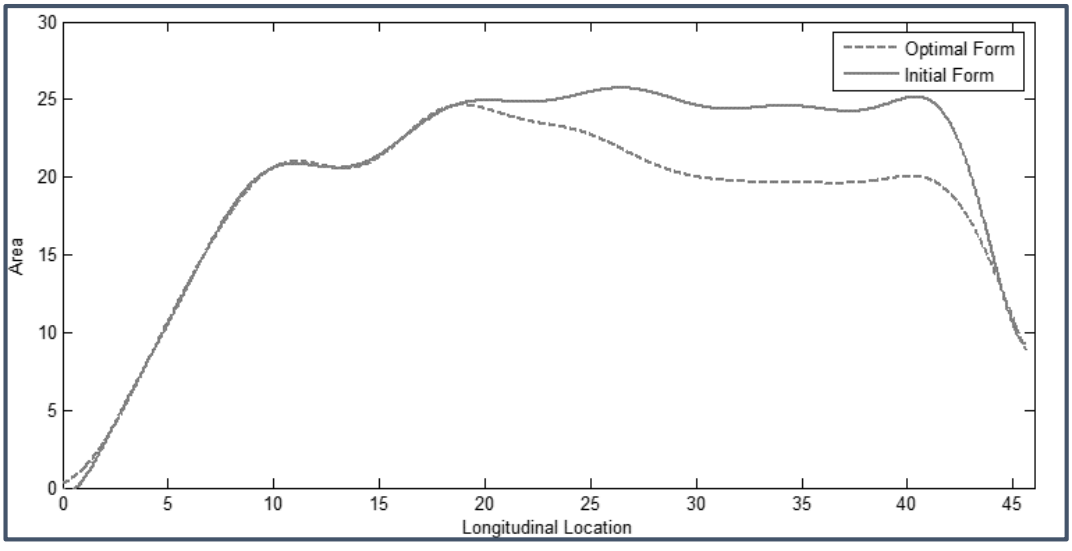

Figure 60-Comparison of Initial and Optimal Fuselage Area Distribution (Fighter Aircraft configuration with GE F414 x 2)

The wave drag coefficient of the fighter aircraft is reduced from 0.204 to 0.192 with the constraints explained above. Total volume of the aircraft is not kept constant in this optimization run. Keeping total volume constant often yields unrealistic geometries. Further work is required to tackle this issue, as total volume of an aircraft may be important design requirement especially for such aircraft. The magnitude of the areas related to engine section are fixed by employing simple area calculation which is less than the initial cross-sectional area magnitudes. Thus, volume participants at the front region of the aircraft increases to keep volume constant which results in unrealistic geometries. To avoid this, constraints of engine is used for optimization only. Lower part of the fuselage must have a place for landing gear, weapons bay and other components. Thus, area reduction is applied for upper part of the fuselage only.

CHAPTER 5

CONCLUSION & FUTURE WORK

5.1 Conclusion

In this thesis, the numerical optimization of the wave drag coefficient for supersonic geometries is performed. In the early stages of research a literature survey is completed on methods about wave drag calculation, and optimization. The wave drag for high speed aircraft has major role on supersonic flight regime. Despite the fact that many other drag components play important roles in the calculation of the overall drag, wave drag coefficient governs the performance of aircraft high speeds. Secondly, the solver is verified by using two different geometries, the wave drag coefficients of which are obtained from literature. It is seen that the difference between the results of the actual study and the literature results are sufficiently in close agreement so as to implement the optimization algorithm. Results are obtained from computational fluid dynamics simulations with a variety of supersonic flow speeds. In detail, two different shapes; namely, Sears–Haack slender body and F-16 are analyzed and the obtained results yield an error that is smaller than 8%.

Next, test cases are introduced with respect to the aerodynamic parameters. Case matrix is generated to analyze the effect of each aerodynamic parameter such as dihedral angle and area of the control surfaces. It is verified that various types of aircraft could be optimized by using the algorithm. Although the optimal shape of each configuration has the smallest wave drag coefficient for the given volume and length, the manufacturability of these aircraft geometries is questionable.

Finally, it is seen that the program has the ability to optimize the entire configuration. However, parts having no effect on the aerodynamic characteristics are enforced to

body shape change. Main reason behind this is preventing an additional aerodynamic trade-off analysis while generating the final configuration of the designed aircraft. Shape optimization is completed with respect to wave drag coefficient, thus, viscous effects are not included in calculations in this study.

For the test cases considered, it can be said that the developed computational tool is capable of optimizing aircraft geometries to yield significant reductions in the wave drag coefficient. Such a tool can be used as is or be developed further to be used in the conceptual design phase, where a high number of configurations need to be analyzed in a short time.

5.2 Future Work

Although the discretization and geometry transfer abilities between *OpenVSP* and the program are appropriate in the conceptual level for this level of design, various aircraft components like pods, weapons, etc. may not be drawn and analyzed by the program. As a future aim, the output of the program is aimed to input to the *OpenVSP* to prepare computational fluid dynamics simulations which enable to prove the reduction in wave drag coefficient. Furthermore, this will also empower the direct connection among the design program "*OpenVSP*", the optimization program and computational fluid dynamics simulation. More complex geometries and constraints for the cross sectional shape of the fuselage will also be added to approach real aircraft geometry [11, 26] For example, an internal weapon bay and a radar dimensions can be related to constraints.

Next, additional objective functions can be combined with the program. Maximization of lift will be complementary for the optimization problem of the complete aircraft post-design. There may be proposed two ways to achieve this aim: (i) using simple inviscid methods in the optimization loop like panel method or (ii) response surface (indirect) optimization combined with computational fluid dynamics simulation. Another objective function may be the minimization of the radar cross section, which is a strong function of the geometry.

Investigating multidisciplinary design optimization for aircraft geometry, embedding additional solvers into the main program to analyze the flow dynamics over the aircraft in more detail may be part of the future steps of the work. Moreover, complete conceptual design of a high speed aircraft including sizing, trade–off studies, and optimization for different design goals can be planned for oncoming research subjects.

REFERENCES

[1] A. W. Wilhite, An Overview of NASA's High - Speed Research Program, ICAS, 2000.

[2] T. Raffin, "http://www.3dcadbrowser.com/," 3D CAD Browser, 14 December 2007. [Online]. [Accessed August 2014].

[3] R. Aboulafia, Jane's Civil Aircraft, Glasgow: Harper Collins Publishers, 1996.

[4] M. Sadraey, "Drag Force and Drag Coefficient," in *Aircraft Performance Analysis*, 2009.

[5] D. P. Raymer, Aircraft Design: A Conceptual Approach, Reston: AIAA Education Series, 2012.

[6] W. J. Strang and R. McKinlay, "Concorde in Service," *Aeronautical Journal*, vol. February, 1979.

[7] B. M. Kulfan, "Fundamentals of Supersonic Wave Drag," in *Fourth International Conference on Flow Dynamics*, Sendai, 2007.

[8] S. K. Rallabhandi and D. N. Mavris, "An Unstructured Wave Drag Code for Preliminary Design of Future Supersonic Aircraft," in *AIAA*, Orlando, 2003.

[9] "http://triaero.sourceforge.net/," TRIAERO, October 2005. [Online]. [Accessed May 2014].

[10] M. G. Hutchison, Multidisciplinary Optimization of High - Speed Civil Transport Configurations Using Variable - Complexity Modeling, Blacksburg: Virginia Polytechnic Institute and State University, 1993.

[11] O. VSP, "www.openvsp.org," 14 February 2014. [Online]. [Accessed March 2014].

[12] MATLAB User's Guide, Natick: The MathWorks Inc., 2014.

[13] ANSYS Fluent 12.0 User's Guide, ANSYS Inc., 2009.

[14] Tecplot.360 User's Manual, Tecplot Inc., 2013.

[15] I. Griva, S. G. Nash and A. Sofer, Linear and Nonlinear Optimization, Philadelphia: Society for Industrial and Applied Mathematics, 2008.

[16] E. Eminton, "On the Numerical Evaluation of the Drag Integral," Ministry of Aviation, London, 1961.

[17] G. N. Ward, Linearized Theory of Steady High - Speed Flow, Cambridge University Press, 1955.

[18] G. -. W. Weber, Lecture Notes - Numerical Optimization, Ankara, 2013.

[19] H. Glauert, The Elements of Aerofoil and Airscrew Theory, Cambridge University Press, 1948.

[20] O. Knill, "Multivariable Calculus - Lecture 21: Greens theorem," Harvard University, 2011.

[21] C. Çıtak and S. Özgen, "Sesüstü Hava Araçlarının Dalga Sürükleme Katsayılarının Sayısal Yöntemlerle Hesaplanması," in *SAVTEK 2014*, Ankara, 2014.

[22] M. S. Cahn and W. B. Olstad, "A Numerical Method For Evaluating Wave Drag," National Advisory Committee for Aeronautics, Langley Field, va., 1958.

[23] M. Hepperle, "The Sonic Cruiser - A Concept Analysis," in *International Symposium "Aviation Technologies of the XXI Century: New Aircraft Concepts and Flight Simulation"*, Berlin, 2002.

[24] T. v. Mourik, Fortran Programming Manual, London: University College London, 2005.

[25] M. Fujino and Y. Kawamura, "Wave - Drag Characteristics of an Over the Wing Nacelle Business Jet Configuration," *Journal of Aircraft*, vol. 40, p. 6, 2003.

[26] R. V. and H. Jr., "An Analysis and Correlation of Aircraft Wave Drag," NASA Technical Memorandum, Langley Station, Hampton, Va., 1964.

[27] T. Kribler, "A Conceptual Design Methodology to Predict the Wave Drag of a Transonic Wing," in *Aerodynamic Design and Optimization of Flight Vehicles in a Concurrent Multi-Disciplinary Environment*, Ottawa, 1999.

[28] K. A. Geiselhart, "Integration of Multifidelity Multidisciplinary Computer Codes for Design and Analysis of Supersonic Aircraft," in *AIAA*.

[29] A. Entsminger, G. David and G. Will, "General Dynamics F-16 Fighting Falcon," AOE 4124.

[30] H. Sobieczky, "New Design Concepts for High Speed Air Transport," in *International Centre for Mechanical Sciences*, N.Y, SpringerWienNewYork, pp. 159-235.

[31] B. Probert, "Aspects [1] of Wing Design for Transonic and Supersonic Combat Aircraft," in *RTO AVT Fluid Dynamics Research on Supersonic Aircraft*, Belgium, 1998.

[32] H. Ashley and M. Landahl, Aerodynamics of Wings and Bodies, New York: Dover Publications, 1965.

[33] GE F414, "http://www.geaviation.com/military/engines/f414/,". [Online]. [Accessed November 2014].

[34] GE F110, "http://www.geaviation.com/military/engines/f110/,". [Online]. [Accessed November 2014].

[35] The Area Rule and F-102 Story, Chapter 5 - The Era of High-Speed Flight, "http://www.hq.nasa.gov/pao/History/SP-440/ch5-10.htm". [Online]. [Accessed January 2015].

[36] Convair F-102 Delta Dagger, "http://en.wikipedia.org/wiki/Convair_F-102_Delta_Dagger". [Online]. [Accessed January 2015].

FIGURES

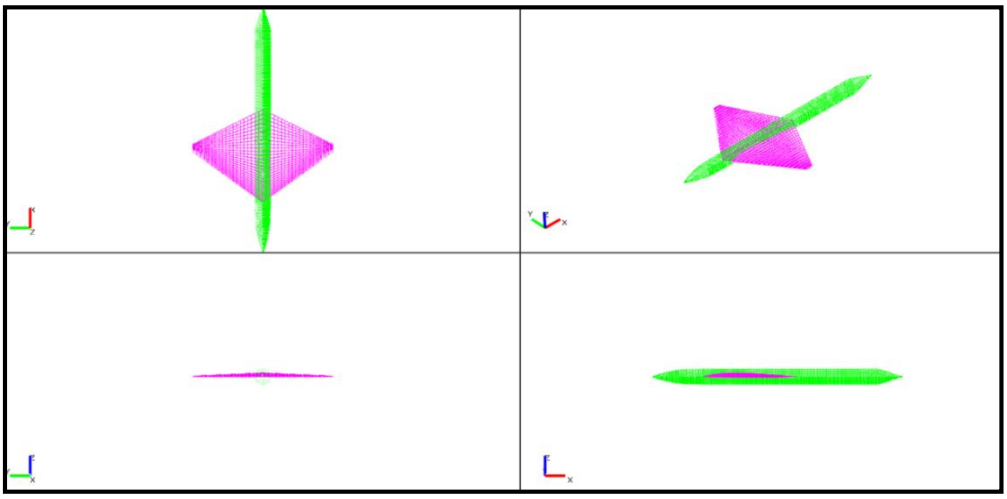

Figure 61–Configuration 1 (*OpenVSP* view)

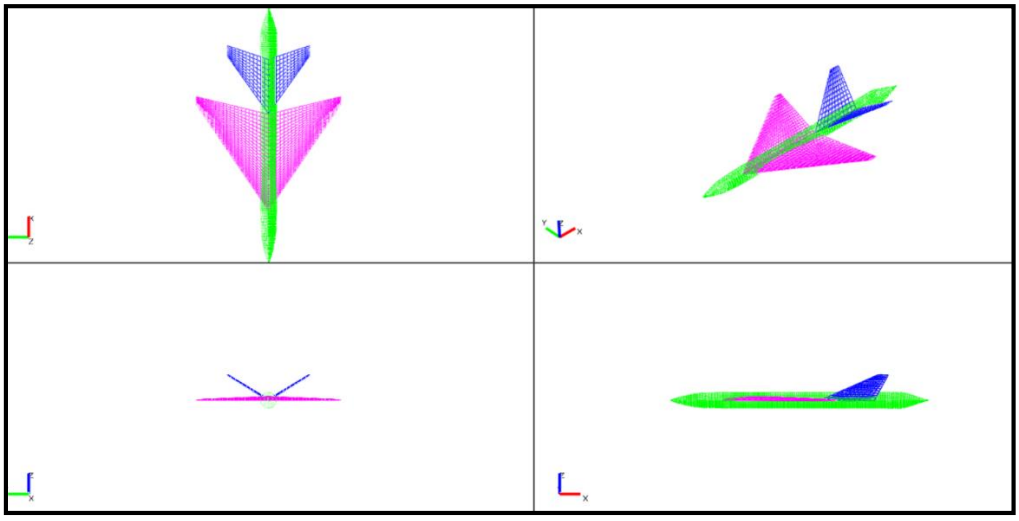

Figure 62–Configuration 2 (*OpenVSP* view)

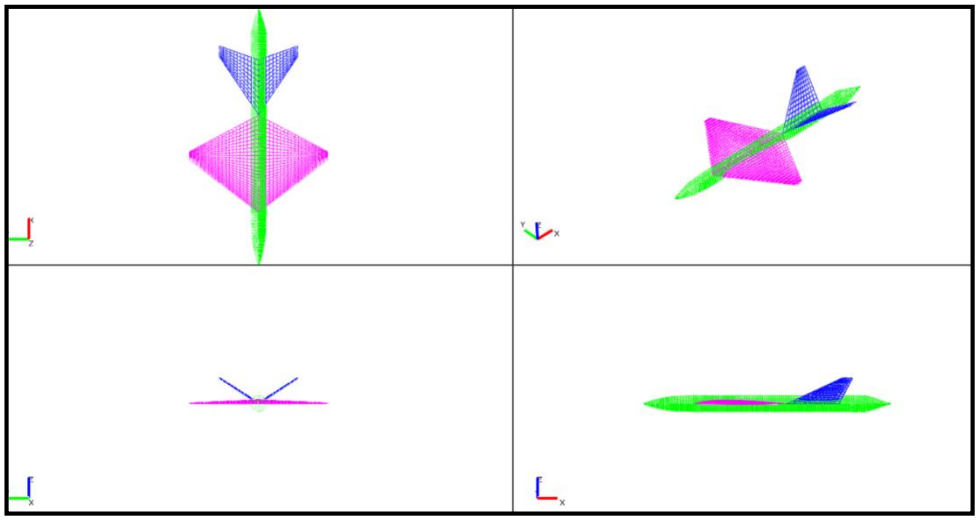

Figure 63–Configuration 3 (*OpenVSP* view)

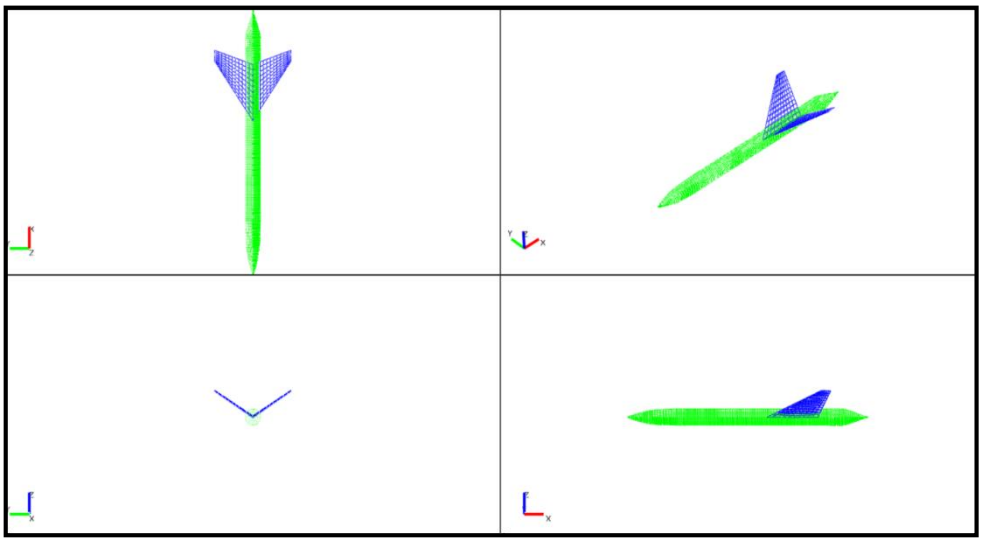

Figure 64–Configuration 4 (*OpenVSP* view)

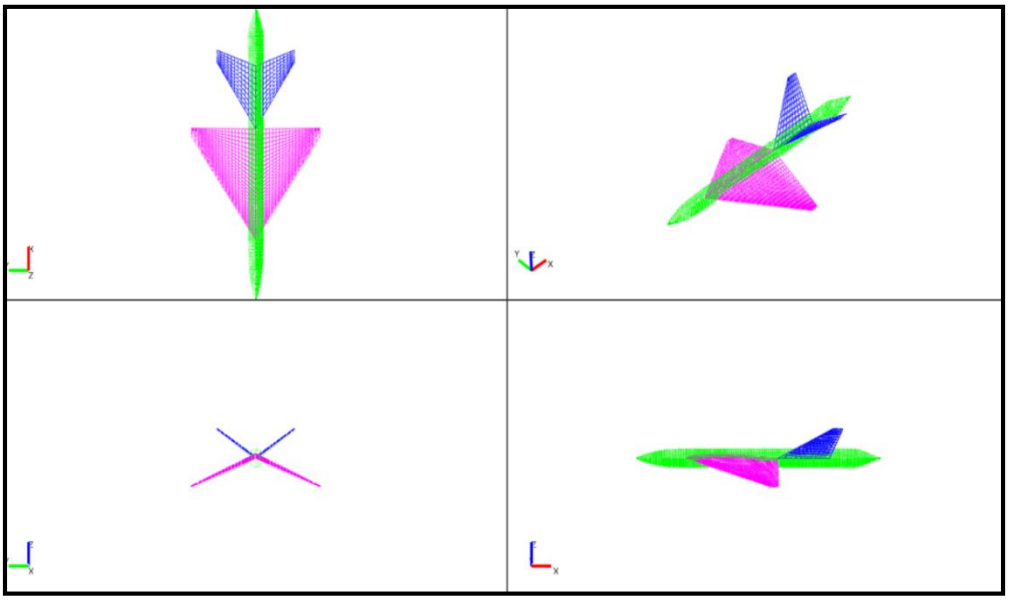

Figure 65–Configuration 5 (*OpenVSP* view)